University of Alberta
Department of Civil &
Environmental Engineering

Structural Engineering Report No. 265

Fatigue Crack Behaviour in Mine Excavator

by

Yue Yin

Gilbert Y. Grondin

and

Alaa E. Elwi

May, 2006

Fatigue Crack Behaviour in Mine Excavator

by

Yue Yin
Gilbert Grondin
Alaa Elwi

Structural Engineering Report No. 265

Department of Civil and Environmental Engineering
University of Alberta
Edmonton, Alberta

May 2006

Executive Summary

Maintenance costs at Syncrude represent a significant portion of yearly operating budget. Minimizing these costs and optimizing the shutdown outages can therefore lead to significant reductions in unit cost. One of the recurring problems with most mining equipment is cracking and this issue is therefore one that needs to be addressed as part of the maintenance and repair program. The frequent and almost certain occurrence of fatigue cracking is largely due to high impact loads, the high frequency of load cycles and large component sizes. The potential for catastrophic brittle fracture is enhanced by high impact loads (resulting in high loading rates), low service temperatures (resulting in a drop of fracture toughness), and large component (causes localized stress triaxiality). To ensure safe and reliable operation, a significant portion of the maintenance budget is allocated to monitor and repair cracks. This monitoring and repair strategy is based on vendor specifications and maintenance personnel experience. However, the oil sand environment causes cracks to appear much earlier than for typical mining applications. Also, newer and larger equipment do not necessarily conform to the experience gained from old equipment. These concerns, coupled with fast retirement rate of personnel, present a challenge to the efforts of mine operators in reducing maintenance cost and increasing equipment reliability.

The purpose of this research is to examine the crack management program at Syncrude and to optimize it using state-of-the-art technology. The research is conducted through collaboration with a research team from the Department of Civil & Environmental Engineering from the University of Alberta and is applied to the BE 395B shovel boom as an example, but the same technique is applicable to any equipment component subjected to fatigue loading. The main product of this research is a tool that can optimize crack repair and improve equipment reliability.

The proposed crack management tool takes the form of a chart that predicts the remaining life of a corner crack in the shovel boom. The predictions presented in these charts are based on limited field measurements of operating load, fatigue testing of boom material, and extensive finite element analysis of the shovel boom. The field and lab data are utilized in the context of fracture mechanics analysis and finite element modeling to predict crack life at any location in the boom. The remaining life predictions are presented in easy-to-use charts and require only minimal engineering experience.

The *Crack Clock* chart is an optimization tool for Shovel maintenance. It enables inspectors and planners to make quick and reliable decisions for managing boom crack repair. It allows maintenance outages to be scheduled based on safe service life rather than operation demands. It supports the prioritization of crack repair of several locations based on their relative remaining life. It helps Maintenance react faster to changing Operation demands without risking catastrophic failures.

Acknowledgements

This work was conducted while the senior author was a post-doctoral fellow in the Department of Civil & Environmental Engineering of the University of Alberta.

Funding for this research was provided by Syncrude Canada Ltd and the Natural Sciences and Engineering Research Council of Canada through a Collaborative Research and Development Grant.

The research was conducted in collaboration with Dr. Khlaed Obaia of Syncrude Research. His assistance with the field work logistic and encouragement throughout this work is gratefully appreciated. The invaluable assistance of Ms. Silvia Gonzalez and Mr. Victor Del Valle with the field instrumentation and data collection for the shovel boom is acknowledged with thanks. The assistance of Mr. Jeremy Wong with the coordination of access and shop implementation is also much appreciated.

Table of Contents

1. Introduction

Syncrude Mine has been employing a significant fleet of the largest mobile equipment in the world. The cost of mining this large volume of ore is a significant portion of ore's unit cost and, therefore, any improvement in mining equipment operation and maintenance can lead to significant reductions in yearly operating budget. One of the limiting problems for Syncrude fleet is cracking. Almost all of mobile equipment has experienced different levels of cracking since operation started in 1978. This frequent and almost sure occurrence of cracking is largely due to high impact loads, high fatigue cycles, low operating temperature and large component size.

To ensure reliable and safe operation, Syncrude allocates a good portion of its maintenance budget to monitor and repair cracks in mobile equipment. The main purpose of this project is to examine the crack management program at Syncrude for the mobile equipment and to optimize it using state-of-the-art technology. Optimizing crack management requires good knowledge of the governing material properties, the state of stress at crack locations, the load spectrum under operating conditions, fracture and fatigue analysis, and inspection techniques for welds and imperfections. In addition, significant time is required to conduct necessary stress and fracture analysis. Therefore, maintenance personnel frequently takes conservative approaches to repair these cracks, which may result in frequent shut down and loss of production. Experience with equipment helps to reduce down time but as the company upgrades its equipment for newer and larger shovels and trucks, benefits from this experience diminishes. These two main issues emphasize the need for an economic and reliable method for predicting crack life.

The research presented in the following was conducted on a Bucyrus Erie (BE) 395B shovel, depicted graphically in Figure 2, as a case study of fatigue load assessment of heavy mining equipment. The main components of the shovel that are of interest in this study are indicated in Figure 2. The main components of the BE 395B shovel consist of the motor and A-frame housing, which sits on a pair of crawlers, the boom, the bucket, the stick and three sets of cables (support cable, crowd cable, and hoist cable) shown in Figure 2. The boom is pinned to the housing at the bottom of the boom and is held at the top by support cables, in a fixed position at 45 degrees. The pin area of the boom consists of a large steel casting welded to the upper portion of the boom, which consists of two built up box girders joined together at two locations along the boom as shown in Figure 3. The bucket, which is a heavy plate structure that is partly cast steel and fitted with teeth, is attached to the end of the stick in a fixed orientation to it. The stick is made of a round hollow structural steel section. The bucket end of the stick is raised up and down with the hoist cable, which wraps around sheaves at the top end of the boom. The stick sits loosely in a saddle that is pinned to the boom, allowing rotation of the stick around the axis of the saddle. The stick is advanced

forward and retracted with the crowd cable. Thus, the stick and the bucket can rotate around the saddle block and translate along its axis. The rotation is controlled by hoist cables and hoist motor while the translation is controlled by the crowd cables and crowd motor.

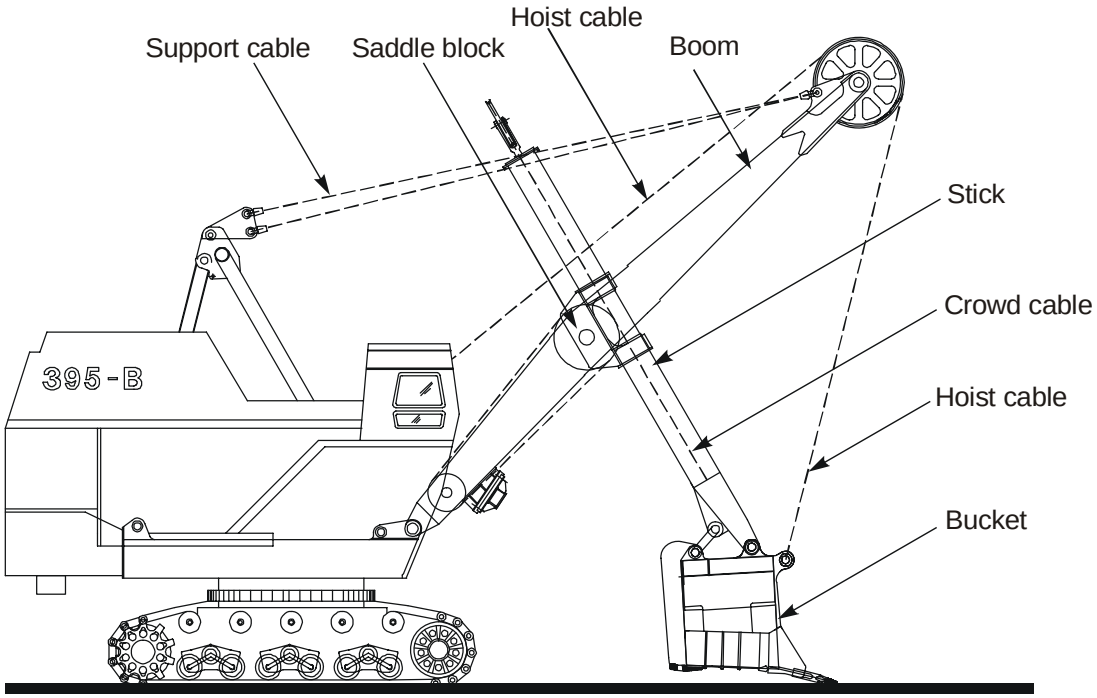

Figure 1 – BE 395B Shovel

During the mining operation, the boom, stick and bucket are restricted to move in the plane of the hoist and support cables. This plane may rotate around the vertical axis of the housing. This rotation around the vertical axis corresponds to an out-of-plane movement of the boom, stick and bucket assembly. The cycle of advancing the bucket into the oilsand face, lifting it up to extract the oil sand from the face, retracting the stick, rotating the vertical plane to the location of the haul truck, unloading, and bringing the bucket back to the oil sand face takes about 50 seconds. The object of the work presented here is the boom. As mentioned above, the boom is a heavy steel box girder structure. The boom is susceptible to the formation of fatigue cracks primarily in the bottom flange and advancing up into the web plates. These cracks develop typically within three months of operation and can reach lengths of up to 450 mm before the boom is repaired.

Although the following work was applied to the BE 395B shovel boom, the same technique used for the shovel boom can be applied to any equipment component subjected to fatigue loading. The procedure includes field monitoring of the equipment to establish a representative fatigue load spectrum for the component under operating conditions, material testing to characterize the fatigue properties and finite element analysis of the structure to determine the stress and strain parameters for fatigue life calculations.

A collaborative research program between a group of researchers from the Department of Civil & Environmental Engineering of the University of Alberta and Syncrude Canada Ltd was initiated in June 2001. The main objective of the research program is to develop a model to predict the behaviour of fatigue cracks in the BE 395 electric shovel boom. In order to develop this predictive model, information in a number of key areas is essential, such as, the load spectrum, the cyclic and monotonic material properties, stresses and strains in areas of stress concentration, and a predictive model that correlates the load spectrum and material properties to the remaining life. Activities have been carried out in each one of these areas.

The current project consists of four phases: definition of the load spectrum, numerical modeling, material properties characterization, and crack behaviour simulation. The load spectrum definition focuses on developing tools to measure actual dynamic loads acting on the equipment under operating conditions, and compare it to design loads. The numerical modeling involves building finite element model of boom with cracks meshed in. The material properties experiments focus on laboratory testing of coupons sampled out of material surrounding field cracks. Fatigue testing of smooth specimen and cracked specimen will be performed to determine the parameters affecting crack initiation life and crack growth rate. Crack behaviour simulation involves incorporating lab and field data into a finite element model of the boom structure and run different crack propagation scenarios to predict failure.

2. Field Test For Load Spectrum Determination

One of the largest sources of error in fatigue life prediction of equipment or structures is related to the lack of knowledge of the stress history. In order to minimize the error attributable to this source, field monitoring of BE 395B shovel 11-77 was conducted for approximately one week starting August 22, 2002. The field test consisted of controlled operation of the shovel under simulated operating conditions and normal operating conditions. Strains were measured at two cross-sections along the boom, hoist and crowd motors voltage, current and rpm were recorded, and the position of the stick was monitored throughout the test period. The following gives a summary of some of the findings from the field tests.

2.1 Field Test Preparation

Two cable displacement transducers were mounted on the boom of the shovel to monitor the position of the stick during excavation as shown in Figure 1. The position of stick was therefore known accurately from initial measurements of the position of the transducers and transducer readings recorded during the field test. Knowledge of the position of the stick is

important in the process of correlating the field data with finite element analysis results, as explained below.

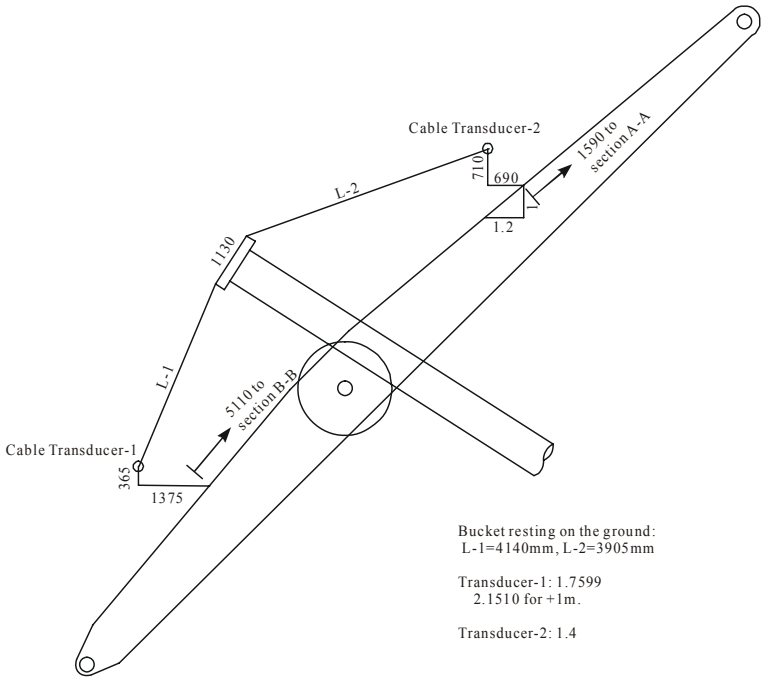

Figure 1 – Position of Cable Transducers

A total of 32 strain gauges were mounted on the boom at sections A-A and B-B, as shown in Figure 2, Figure 3 and Figure 4. Because the loading condition in the boom consist of bending and axial force only, single grid strain gauges, aligned with the axis of the boom, were used for project. The strain gauges were used to validate a finite element model of the boom, which was developed to determine the stresses existing in the different hot spots on the boom. Because the strain gauges were going to be used to validate the finite element model, it was important that the strain gauges be located in regions of little to no stress concentration. The monitored sections were therefore taken at intermediate points between stiffeners in the boom. Both legs of the boom were instrumented as shown in Figure 3.

The strain gauges and cable transducers were monitored using a high-speed data acquisition system and computer at a sampling rate of 100 cycles per second. The crowd and hoist motor voltage, current and rpm were recorded using a data recorder.

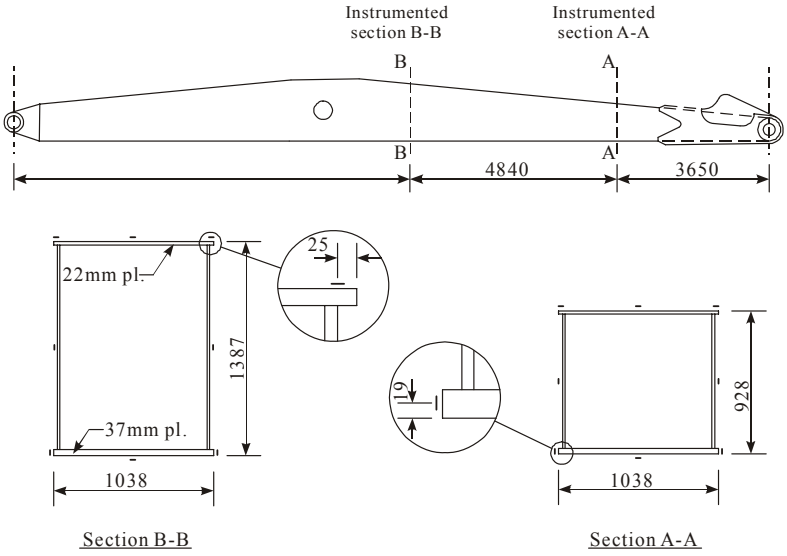

Figure 2 – Position of Strain Gauges

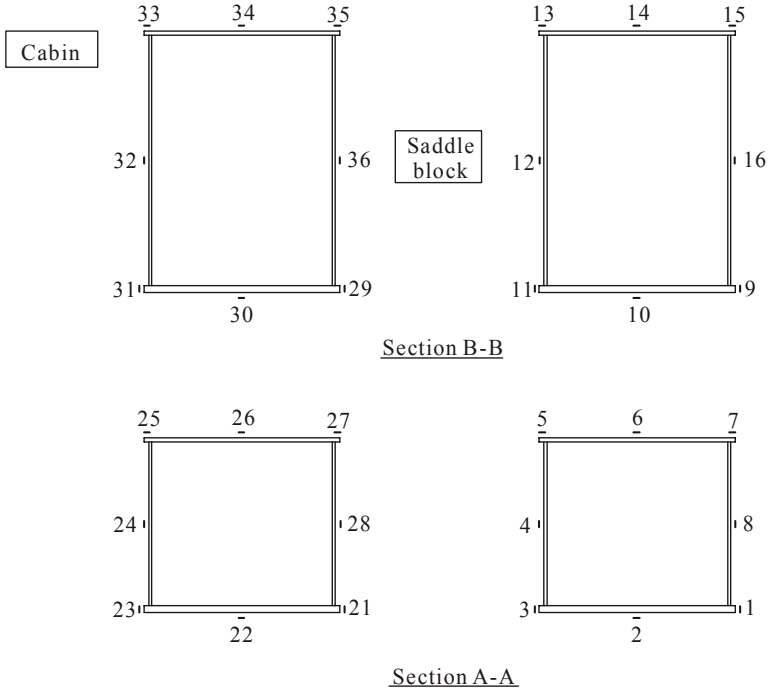

Figure 3 – Location of Strain Gauges

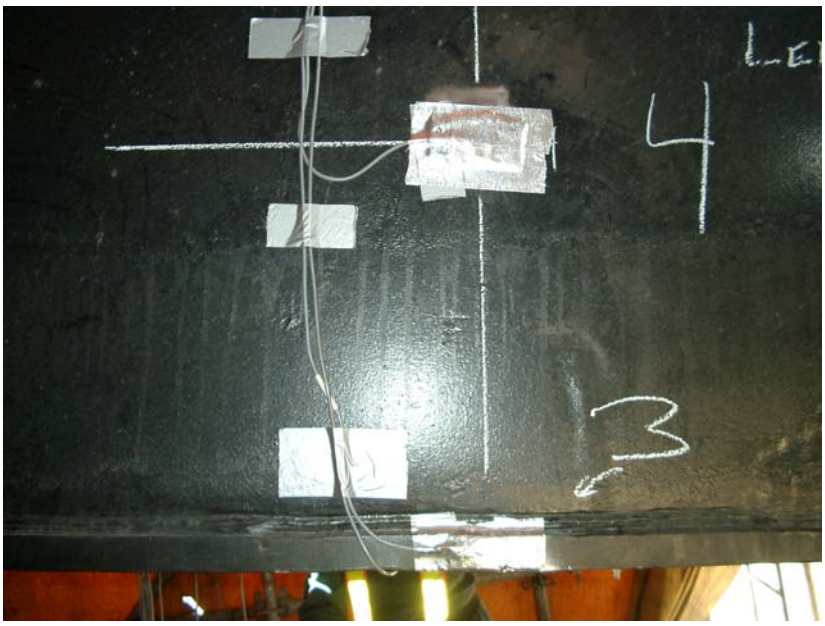

Figure 4 – Strain Gauge Installation on Web and Bottom Flange of Boom at Section A-A

2.2 Field Test Procedure

During the simulated operation and the first hour of normal operation, a video record of the excavator movements was collected. The computer, data recorder and video camera were synchronized. The difference in time between the various data collection instruments is as follows:

Computer Time	+00:00:00	Watch Time	+00:02:06
Record Time	+00:03:03	Camcorder Time	+00:03:09

A controlled field test was conducted on August 22, 2002. During this test the shovel was used through its full range of motion with the dipper empty and the dipper full. In addition, the shovel was fully engaged in digging operation. The data collection started at 3:20:48 (data acquisition system time) when the shovel was in the rest position with the bucket resting on the ground. The angle of the boom was measured to be 39.5º to the horizontal at that time. Controlled operation of the shovel started with an empty bucket. Table 1 summarizes the shovel activity during this part of the test. The tests were repeated twice and are identified as tests 1 and 2 in the table. The time at the start of the activity was recorded and reported in the table. The start of the activity is also identified by a letter and a number. The letters are sequential and the number refers to the test number. For each activity described in the first column of the table, the start time is recorded in the second column for test 1 and in the third column for test 2.

Table 1 – Field Test with Empty Bucket

Activity (reference to figure 11)	Computer Time	
	Test 1	Test 2
Bucket on ground (just before start moving) (Figure 11(a))	**A_1** 3:33:17	**A_2** 3:37:40
<Start moving>		
Stick fully retracted (up) (Figure 11(b))	**B_1** 3:33:50	**B_2** 3:38:04
Stick fully retracted in near horizontal position (Figure 11(c))	**C_1** 3:34:32	**C_2** 3:38:45
Stick fully extended in near horizontal position (Figure 11(d))	**D_1** 3:35:05	**D_2** 3:39:09
Stick fully retracted in near horizontal position (Figure 11(e))	**E_1** 3:35:32	**E_2** 3:39:41
Stick fully retracted in vertical position (Figure 11(f))	**F_1** 3:36:27	**F_2** 3:40:20*
Stick in vertical position on ground (Figure 11(g))	**G_1** 3:37:02	**G_2** 3:40:36
Return to stick fully extended on ground (Figure 11(h))	**H_1** 3:37:31	**H_2** 3:41:01*
Swing (half speed)	**I** 3:41:32	**J** 3:42:31
Swing back (full speed)	**K** 3:42:31	**L** 3:42:56

*The shovel did not pause.

The controlled test was continued with the bucket full of tar sand. Table 2 summarizes the shovel activity during this part of the test. Once again, the test was repeated twice. The controlled test was completed at 3:56:14.

Table 2 – Field Test with Bucket Full

Activity	Time	
	Test 1	Test 2
Bucket on ground (just before start moving)	**A_3** 3:45:20	**A_4** 3:48:11
<Start moving>		
Stick fully retracted (up)	**B_3** 3:46:10	**B_4** 3:48:45
Stick fully retracted in horizontal position	**C_3** 3:46:48	**C_4** 3:49:18
Stick fully extended in horizontal position	**D_3** 3:47:16	**D_4** 3:49:52
Stick fully retracted in horizontal position	-	-
Stick fully retracted in vertical position	-	-
Stick in vertical position on ground	-	-
Return to stick fully extended on ground	**H_3** 3:48:03	**H_4** 3:50:30*
Swing (half speed)	**I'** 3:50:31	**J'** 3:51:20
Swing back (full speed)	**K'** 3:51:25	**L'** 3:51:47

The field test under normal operating conditions was conducted from August 23,2002 to August 30,2002. However, because of shut down of the shovel for repairs during that period, only the data collected on August 23 and August 30 could be used for the project. This, couple with the fact that no other data could be collected during the project period, severely impede the ability of the procedure developed in the following to predict the remaining life of the boom.

2.3 Strain Data Analysis

Filtering of Data

In order to eliminate parasitic voltages (electronic noise) from the recorded data, the measured strain data were filtered using a low-pass filter. Figure 5 and Figure 6 show typical data obtained from strain gauges 1 and 3, respectively. The data before filtering shows significant high frequency noise, which was eliminated by the procedure outlined below.

Filtering of a signal is possible if the frequencies of the parasitic and gauge signals are different as shown in Figure 6. Some of the different filters that are employed in signal conditioning include: low-pass filter, high-pass filter, band-pass filter and band-stop filter. A low-pass filter passes low-frequency components of the output while attenuating high-frequency components. This type of filter is therefore suitable for data as shown in Figure 6.

The input-output relationship can be simply described by

$$y_k = \sum_{n=0}^{L} b_n x_{k-n} \qquad [1]$$

where y is the output, or filtered data, and x is the input data. The objective of the filter design is to generate the b_n coefficients, which are the elements of the impulse response of the filter. Different time-domain window functions are used to obtain these coefficients and the one with minimum width of transition band and minimum oscillatory response is adopted. The filtered data shown in Figure 5 and Figure 6 indicate that the filter used for this data provides adequate filtering. Although a very small time shift seems to be indicated, the range of output value does not suffer from this time shift.

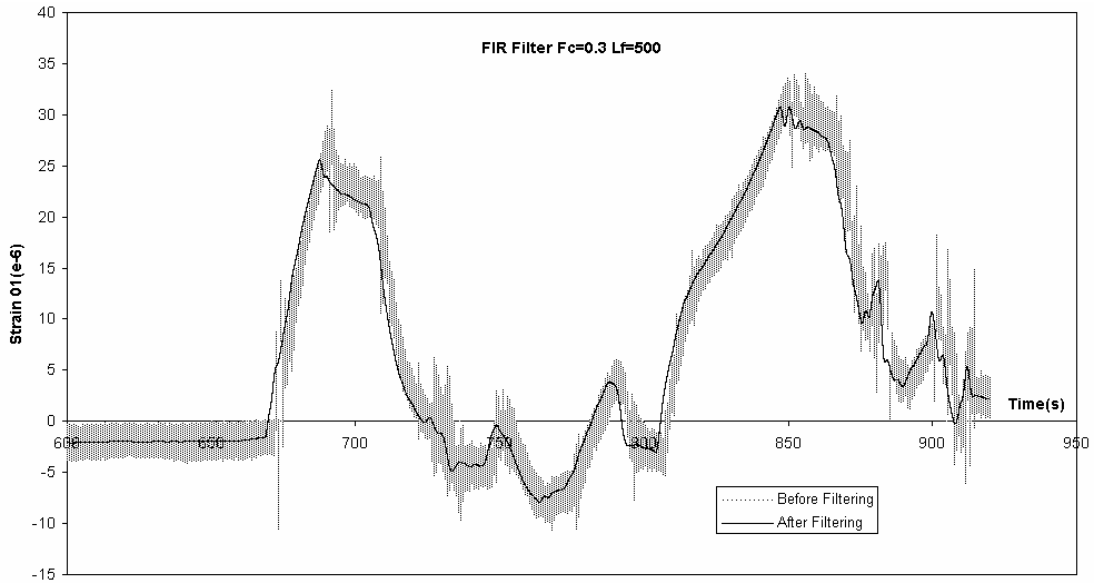

Figure 5 – Data from Strain Gauge 1 Before and After Filtering

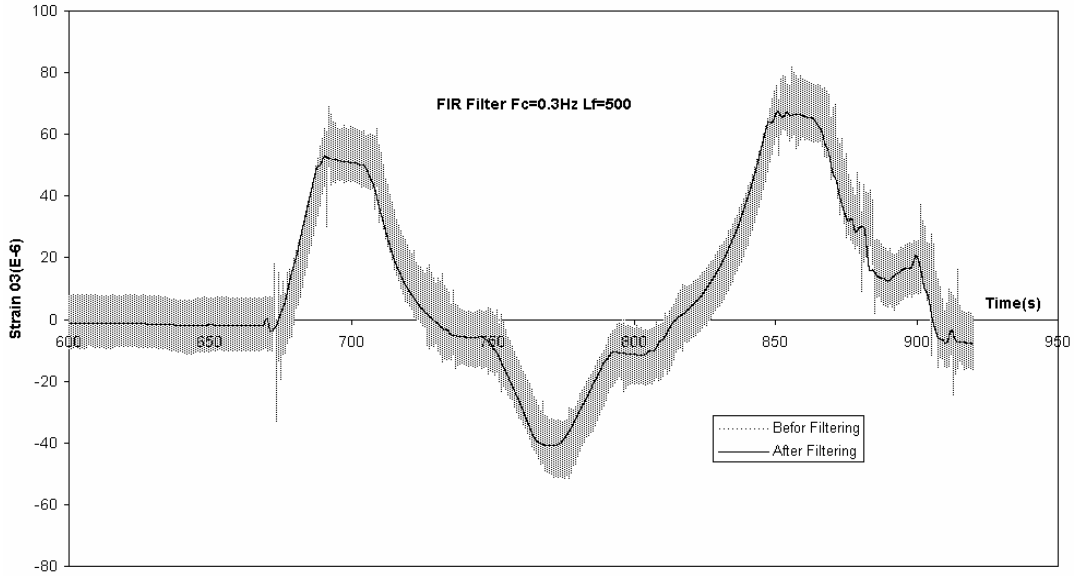

Figure 6 – Data from Strain Gauge 3 Before and After Filtering

2.4 Preliminary Study on Field Test Data

Raw data from cable transducers collected during the controlled test are shown in Figure 7 and Figure 8 for transducers 1 and 2, respectively. A comparison of the data with the events summarized in Tables 1 and 2 indicate that the cable transducers were responding well.

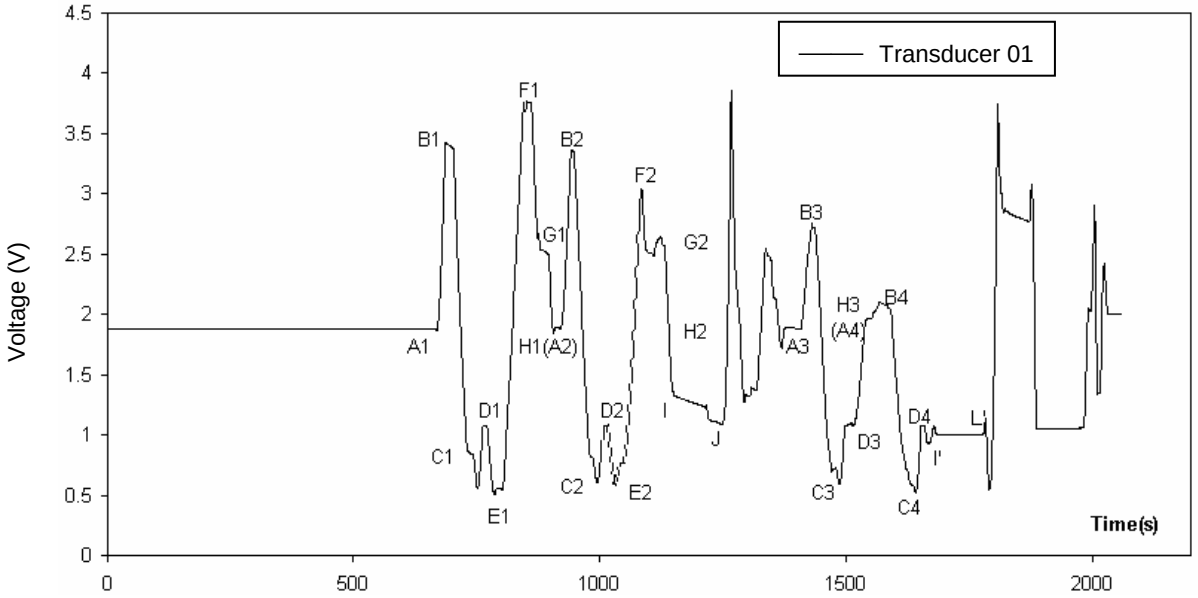

Figure 7 – Voltage Data from Cable Transducer 1

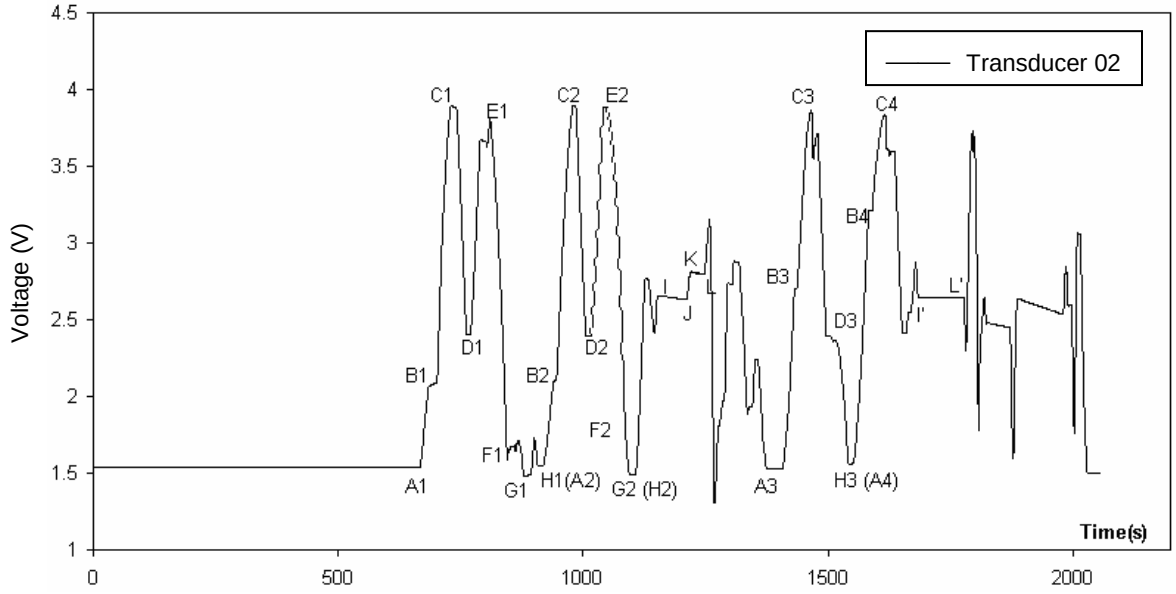

Figure 8 – Voltage Data from Cable Transducer 2

Five strain gauges (11, 12, 13, 14 and 35 shown in Figure 3) were damaged before the test began on August 22. In addition, examination of the strain gauge data indicated that gauges 1, 9, 16 and 25 were not functioning properly during the test. These strain gauges are therefore ignored in the analysis of the test data.

2.5 Stress Cycle Counting

The strain and stress history in most equipment consists of variable amplitude stress or strains. When dealing with variable amplitude loading, it is common practice to reduce the data to a stress or strain spectrum in order to facilitate the calculations of fatigue damage so that the effect of variable amplitude load histories can be compared to fatigue data obtained with simple constant amplitude load cycles. The procedure of reducing a variable stress history into a stress spectrum is based on the assumption that stress interaction is not significant in fatigue calculations and is achieved by "cycle counting". The most commonly used cycle counting method is the rainflow counting method (Stephens *et al.*, 2001).

The rainflow method counts a history of peaks and valleys in sequence according to the following procedure:

Step 1 - Read the next stress value, S.
Step 2 - Form ranges X and Y. If the vector contains less than 2 points past the reference point, go to step 1.
Step 3 - Compare ranges X and Y
  a. If X<Y, go to step 1.
  b. If X=Y and Y contains S, go to step 1.
  c. If X>Y and Y contain S, go to step 4.
  d. If X≥Y and Y does not contain S, go to step 5.
Step 4 - Move S to the next point in the vector. Go to step 1.
Step 5 - Count range Y. Discard the peak and valley of Y. Go to step 2.
Step 6 - Read the next peak or valley from the beginning of the vector E(n). If the starting point, S, has been reread, stop.
Step 7 - Form ranges X and Y. If the vector contains less than 2 points past the reference point, go to step 6.
Step 8 - Compare ranges X and Y.
  a. If X<Y, go to step 6.
  b. If X≥Y, go to step 9.
Step 9 - Count range Y. Discard the peak and valley of Y. Go to step 7.

The above procedure was used to reduce the variable amplitude strains in the shovel boom into strain spectra. The results of the strain cycle counting are presented following

2.6 Strain Spectrum Analysis

The filtered strain data indicated that the strain magnitude and distribution in both legs of the boom were almost identical, indicating negligible out-of-plane effects and torsion effects in the boom. The strain data was used to derive a strain spectrum, which characterizes the strain history during the two days of operation for which field data was obtained, at the cross-sections of the boom that were monitored in the field test program. Furthermore, the strain data was used to validate the finite element model developed to obtain localized strains in the boom at fatigue prone areas. This validation process will be described later in this report.

The strain spectrum at each location was counted using the above algorithm. Sample results of cycle counting (average strains in the bottom and top flanges at cross-section B-B (see Figure 2)) are illustrated in Figure 9. Strain ranges less than 1/10 of the maximum strain range were neglected in these calculations. These strain ranges are small and would lead to negligible fatigue damage.

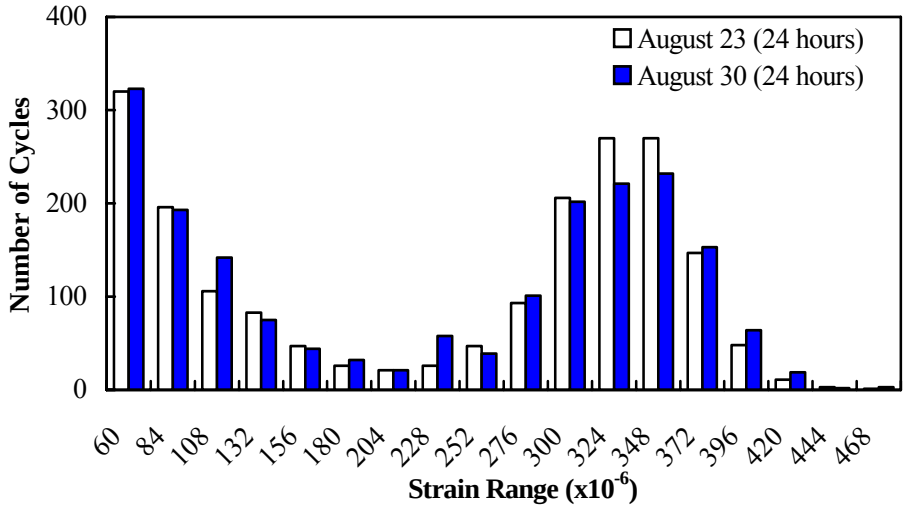

(a) On Bottom Flange

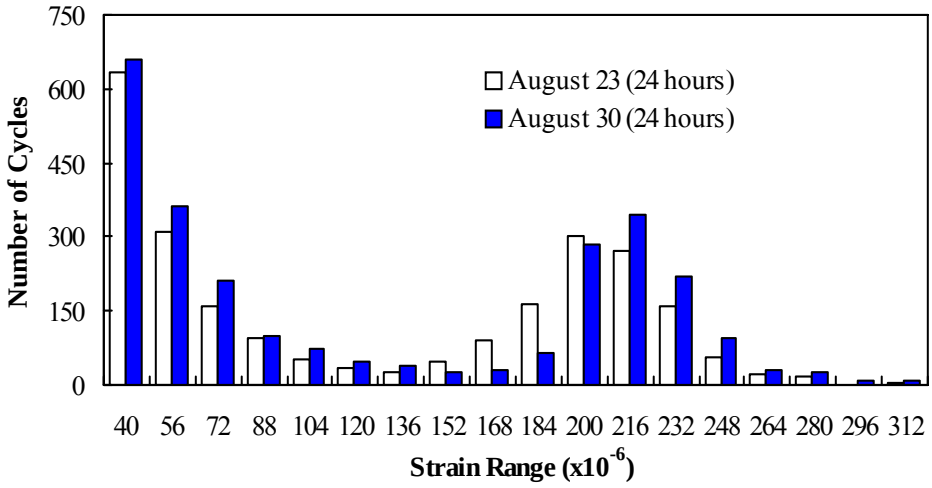

(b) On Top Flange

Figure 9 – Strain Spectrum from Measurements at Section B-B

The strain data presented over a one week interval in Figure 9 indicate that the strain data were very similar throughout the test period. The magnitude and number of cycles of the strain spectra on August 23 and August 30 at the higher strain ranges agree well. This, obviously, provides the reassurance that the conditions over time are not highly variable. It should be noted, however, that although the measurement period spanned over one week, the position of the shovel in the mine did not change significantly over that period since the

shovel was shut down because of electrical problems. Therefore, the collected field data do not reflect variation of conditions at different places in the mine. Seasonal variations of conditions, due to changes in temperature, are therefore not reflected in the collected data.

The strain spectra presented in Figure 9 indicate that the strain ranges on the bottom flange are much larger than those on the top flange. This is consistent with the observation that most of the fatigue cracks in the shovel boom are observed on the bottom flange or in the bottom portion of the boom webs.

2.7 Determination of Stick Position

The orientation of the stick can be determined from the position of three points: P1, P2 and PP as shown in Figure 10. The following six equations can be derived for the six unknown coordinates, x1, y1, x2, y2, xx and yy of the three reference points.

$$(x1-a)^2+(y1-b)^2=l1^2 \quad [2]$$

$$(x2-c)^2+(y2-d)^2=l2^2 \quad [3]$$

$$(x2-x1)^2+(y2-y1)^2=D^2 \quad [4]$$

$$(x3-e)^2+(y3-f)^2=R^2 \quad [5]$$

$$\frac{y2-y1}{x2-x1}=\frac{yy-f}{xx-e} \quad [6]$$

$$\frac{xx-(x1+x2)/2}{yy-(y1+y2)/2}=-\frac{yy-f}{xx-e} \quad [7]$$

Although the equations are simple, a closed formed solution of these equations is difficult. The solution of Equations [2] to [7] is more easily obtained iteratively. The iterative procedure takes the following form:

- Obtain an initial position of Point P(x,y) from Equations [8] and [9].

$$(x-a)^2+(y-b)^2=(l1+D/2)^2 \quad [8]$$

$$(x-d)^2+(y-d)^2=(l2+D/2)^2 \quad [9]$$

- Determine Point PP(xx,yy) from Equations [5], [7] and [10].

$$x=(x1+x2)/2, \qquad y=(y1+y2)/2 \quad [10]$$

- Determine the position of points P1(x1,y1) and P2(x2,y2) from Equations [2], [3], [4] and [5].
- Obtain a more accurate position of Point P(x,y) from Equation [10].
- Repeat steps 2, 3, and 4 until convergence is reached.

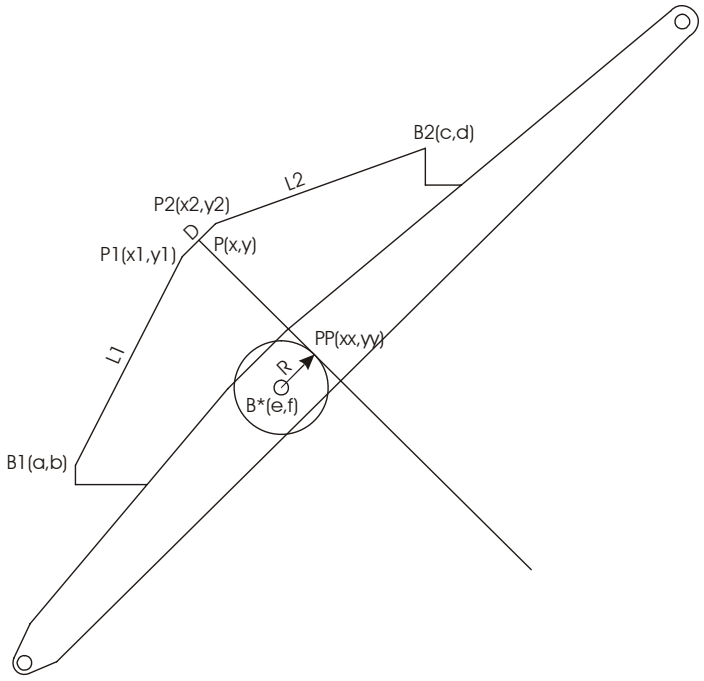

Figure 10 – Determination of Stick Position

As illustrated in Figure 11, some reference positions of the stick, identified in Table 1, during the first stage of the controlled field tests were determined successfully using the iterative procedure. The stick positions determined in this fashion are in good agreement with the position observed during the test and reported in Table 1.

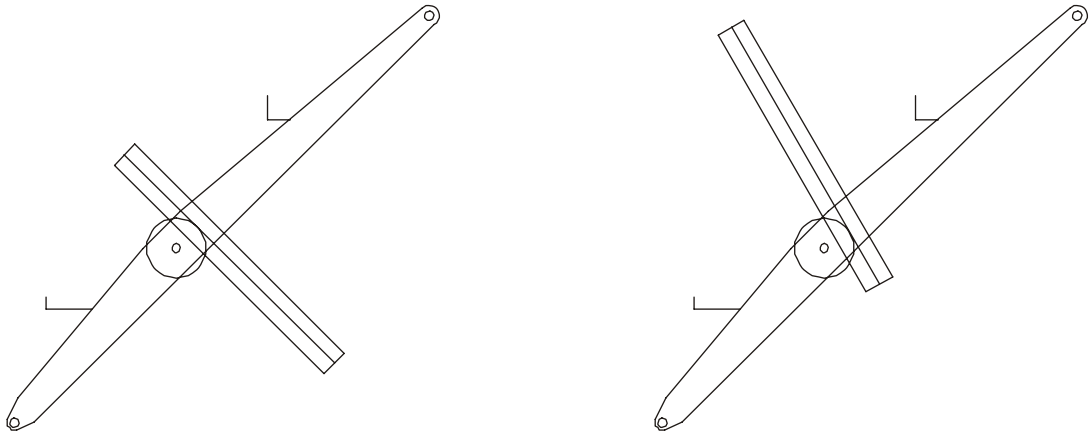

(a) Bucket on the Ground (b) Stick Fully Retracted

Figure 11 – Reference Positions of the Stick

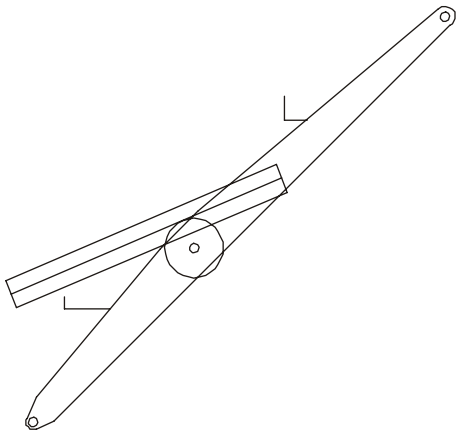

(c) Stick Fully Retracted in Near Horizontal Position

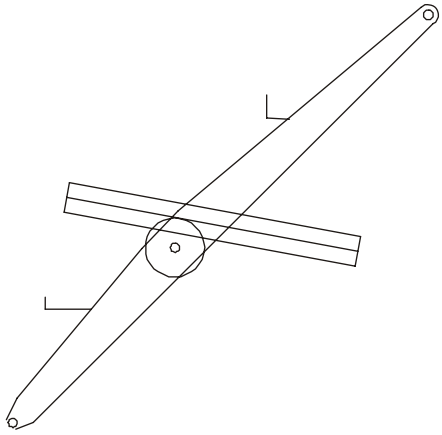

(d) Stick Fully Extended in Near Horizontal Position

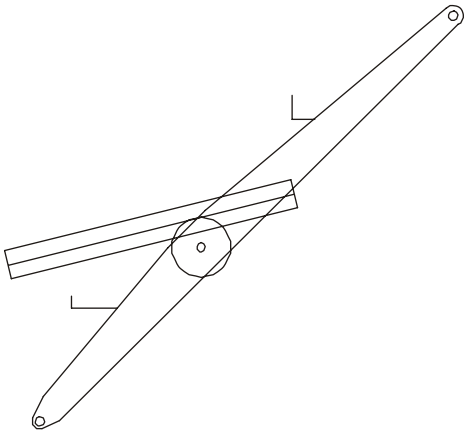

(e) Stick Fully Retracted in Near Horizontal Position

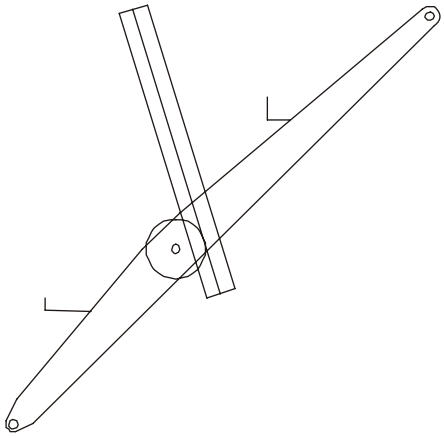

(f) Stick Fully Retracted in Near Vertical Position

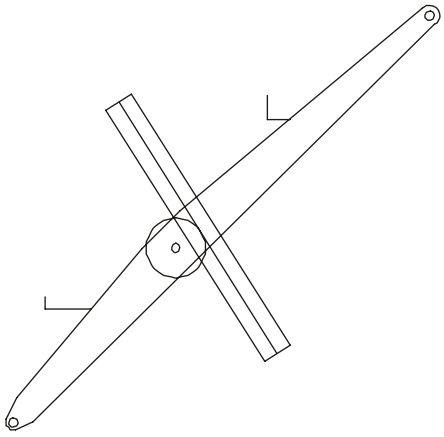

(g) Stick on the Ground in a Near Vertical Position

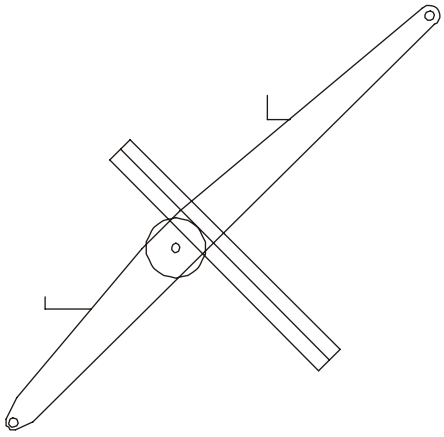

(h) Stick Returned to its Original Position

Figure 11– Reference Positions of the Stick (Cont'd)

3. Modelling of Instrumented Boom

3.1 In-plane Forces on the Boom

The internal in-plane forces at instrumented cross-sections A and B (axial forces N_A and N_B and bending moments M_A and M_B) were determined from the strain data and assuming the strain distribution shown in Figure 12. The linear strain distribution was confirmed by plotting the measured strains over the depth of the boom in both legs of the two instrumented sections. The strain distributions shown in Figure 12 (a) and Figure 12 (b) illustrate two conditions, one where all the section is in tension and one where part of the section is in tension and part is compression. The following procedure, applicable to both web strain distributions illustrated in Figure 12, was developed to obtain the internal forces from the measured strains.

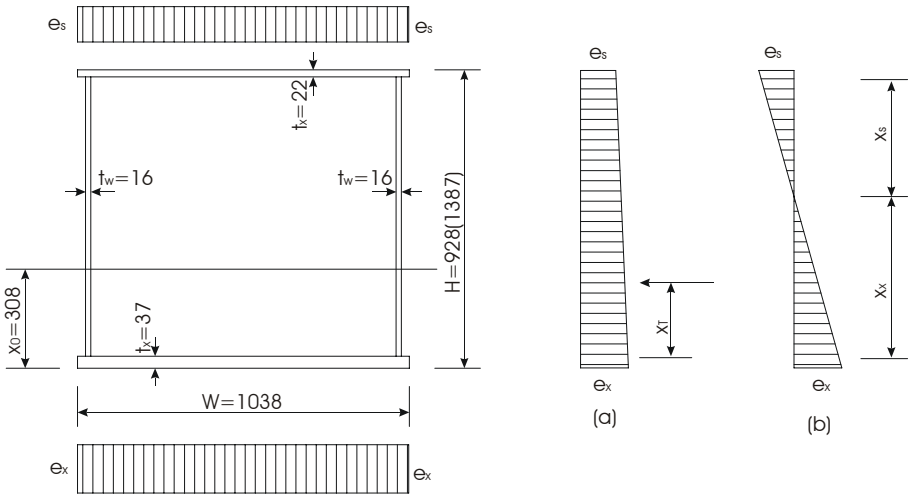

Figure 12 – Sectional Property and Simplified Strain Distribution

1. When $e_x \cdot e_s \geq 0$, as shown in Figure 12(a)

$$N = [W \cdot t_x \cdot e_x + W \cdot t_s \cdot e_s + (H - t_x - t_s) \cdot t_w (e_x + e_s)] \cdot E \quad [11]$$

$$M = M_x + M_s + M_w \quad [12]$$

where,

$$M_x = W \cdot t_x \cdot e_x \cdot (x_0 - \frac{t_x}{2}) \cdot E \quad [13]$$

$$M_s = -W \cdot t_s \cdot e_s \cdot (h - x_0 - \frac{t_s}{2}) \cdot E \quad [14]$$

$$M_w = H \cdot t_w \cdot (e_x + e_s) \cdot (x_0 - x_T - t_x) \cdot E \quad [15]$$

where,

$$x_T = \frac{e_x \cdot H + 2 \cdot e_s \cdot H}{3 \cdot (e_x + e_s)} \quad [16]$$

2. When $e_x \cdot e_s < 0$, as shown in Figure 12(b)

$$N = [W \cdot t_x \cdot e_x + W \cdot t_s \cdot e_s + x_x \cdot t_w \cdot e_x + x_s \cdot t_w \cdot e_s] \cdot E \quad [17]$$

$$M = M_x + M_s + M_{wx} + M_{ws} \quad [18]$$

where,

$$M_x = W \cdot t_x \cdot e_x \cdot \left(x_0 - \frac{t_x}{2} \right) \cdot E \quad [19]$$

$$M_s = -W \cdot t_s \cdot e_s \cdot \left(h - x_0 - \frac{t_s}{2} \right) \cdot E \quad [20]$$

$$M_{wx} = x_x \cdot t_w \cdot e_x \cdot \left(x_0 - \frac{x_x}{3} - t_x \right) \cdot E \quad [21]$$

$$M_{ws} = -x_s \cdot t_w \cdot e_s \cdot \left(x_x + t_x + \frac{2 \cdot x_s}{3} - x_0 \right) \cdot E \quad [22]$$

$$x_x = \frac{|e_x| \cdot (H - t_s - t_x)}{|e_x| + |e_s|}; \qquad x_s = \frac{|e_s| \cdot (H - t_s - t_x)}{|e_x| + |e_s|} \quad [23]$$

A positive force N causes tension in the cross-section and a positive moment M causes tension in the bottom flange.

3.2 Forces on the Boom

In order to load the finite element model the cable forces must be determined. These are calculated from equilibrium considerations and the force effects determined at Sections A and B of the boom. Cable forces T_1 and T_3 shown in Figure 13 can be determined from equilibrium consideration of the end part of the boom.

The three equilibrium equations can be written as follows:

From $\sum F_x = 0$,

$$N \cos\varphi_0 - V \sin\varphi_0 + T_1 \cos\varphi_{1-1} + T_1 \sin\varphi_{1-2} + T_3 \cos\varphi_3 = 0 \quad [24]$$

From $\sum F_y = 0$,

$$N \sin\varphi_0 + V \cos\varphi_0 + T_1 \sin\varphi_{1-1} + T_1 \cos\varphi_{1-2} + T_3 \sin\varphi_3 = 0 \quad [25]$$

From $\sum M_E = 0$

$$M - V \cdot L = 0 \qquad [26]$$

where L is the distance from the instrumented section to the sheave axis (L_A or L_B) and V and M are the shear force and the bending at the instrumented sections.

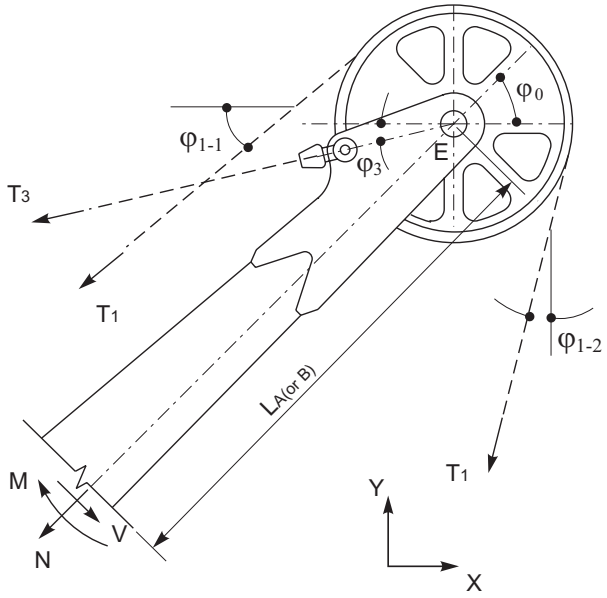

Figure 13– Free-body Diagram of the End Part of the Boom

It follows that

$$V = M / L \qquad [27]$$

$$T_1 = \frac{\sin\varphi_3 \cdot (V \sin\varphi_0 - N \cos\varphi_0) + \cos\varphi_3 \cdot (N \sin\varphi_0 + V \cos\varphi_0)}{\sin\varphi_3 \cdot (\cos\varphi_{1-1} + \sin\varphi_{1-2}) - \cos\varphi_3 \cdot (\sin\varphi_{1-1} + \cos\varphi_{1-2})} \qquad [28]$$

$$T_3 = \frac{N \cos\varphi_0 - V \sin\varphi_0 + T_1 \cdot (\cos\varphi_{1-1} + \sin\varphi_{1-2})}{-\cos\varphi_3} \qquad [29]$$

Since T_1 is the force in the hoist cable, it should always be positive (tension force). When the above equations indicate that T_1 is negative, the cable force is assumed to be zero, indicating that the cable is loose. According to the above calculations, a force F_d corresponding to the dynamic effect of the system, which is perpendicular to the boom as shown in Figure 13, must be introduced to maintain equilibrium of this part of the boom. In fact, this dynamic force F_d should be present at all time, but it is impossible and unnecessary to distinguish it from the force in the cables when T1 is positive. The following equations can be deduced easily by considering the equilibrium state with F_d instead of T_1.

$$V = M / L \quad [27]$$

$$T_1 = 0 \quad [30]$$

$$T_3 = -\frac{N}{\cos(\varphi_0 - \varphi_3)} \quad [31]$$

$$F_d = V - T_3 \sin(\varphi_0 - \varphi_3) \quad [32]$$

Because there should be some tension force in the support cables before the strain gauges were zeroed, it is possible that the calculated value of T_3 be negative, which indicates a decrease of the tension force in the support cables.

T_2 and R_B can be determined by considering equilibrium of the stick and the boom, as shown in Figure 14 and Figure 15. The three equations of equilibrium for the stick are:

$$\sum F_x = 0 \qquad T_2 \cos\varphi_2 + R_B \sin\varphi_2 + T_1 \sin\varphi_{1-2} - R = 0 \quad [33]$$

$$\sum F_y = 0 \qquad T_2 \sin\varphi_2 - R_B \cos\varphi_2 - T_1 \cos\varphi_{1-2} + W = 0 \quad [34]$$

$$\sum M_B = 0 \qquad W \cdot L_W + R \cdot L_R - T_1 \cdot L_{T1} = 0 \quad [35]$$

Eliminating the unknown forces R and W,

$$\begin{aligned}(L_R \cos\varphi_2 - L_W \sin\varphi_2) \cdot T_2 + (L_R \sin\varphi_2 + L_W \cos\varphi_2) \cdot R_B + \\ (L_W \cos\varphi_{1-2} + L_R \sin\varphi_{1-2} - L_{T1}) \cdot T_1 = 0\end{aligned} \quad [36]$$

From equilibrium of the boom,

$$\sum M_A = 0 \qquad L_{T_2} \cdot T_2 + L_{R_B} \cdot R_B + \left(L_{Boom} - L_{A\,or\,B}\right) \cdot V + M = 0 \quad [37]$$

Therefore,

$$R_B = \frac{(T_1 \cdot L_{T_1} - T_1 \cdot L_w \cos\varphi_{1-2} - T_1 \cdot L_R \sin\varphi_{1-2}) \cdot L_{T_2} + \left[M + (L_{Boom} - L_{A\,or\,B}) \cdot V\right] \cdot (L_R \cos\varphi_2 - L_w \sin\varphi_2)}{(L_R \sin\varphi_2 + L_w \cos\varphi_2) \cdot L_{T_2} - (L_R \cos\varphi_2 - L_w \sin\varphi_2) \cdot L_{R_B}}$$

. . . [38]

$$T_2 = \frac{-L_{R_B} \cdot R_B - (L_{Boom} - L_{A\,or\,B}) \cdot V - M}{L_{T_2}} \quad [38]$$

and,

$$R = T_2 \cos\varphi_2 + R_B \sin\varphi_2 + T_1 \sin\varphi_{1-2} \quad [39]$$

$$W = -T_2 \sin\varphi_2 + R_B \cos\varphi_2 + T_1 \cos\varphi_{1-2} \quad [40]$$

It should be noted that, in the above equations, when L_A is used, the shear force, *V*, and the bending moment , *M*, are those applicable to section *A*-*A* of the boom. Similarly, when the length L_B is used in the equations, the shear force and bending moment are both determined at section *B*-*B*. The axial force in the crowd cable, T_2, calculated from the measured strains, is illustrated in Figure 16 for 10 cycles of normal digging operation.

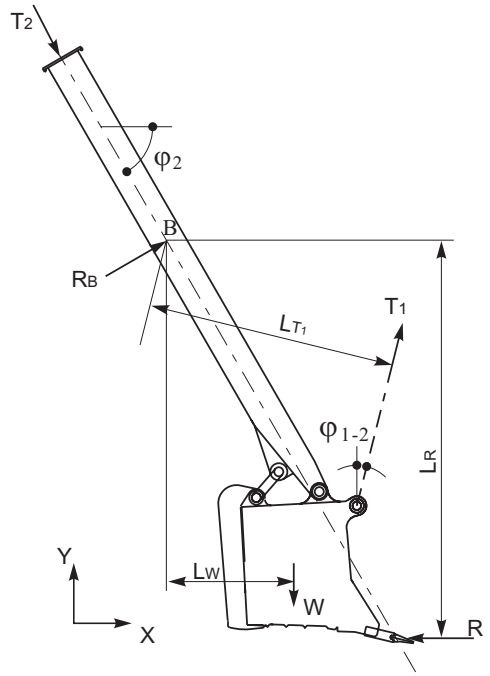

Figure 14 – Free-body Diagram of the Stick

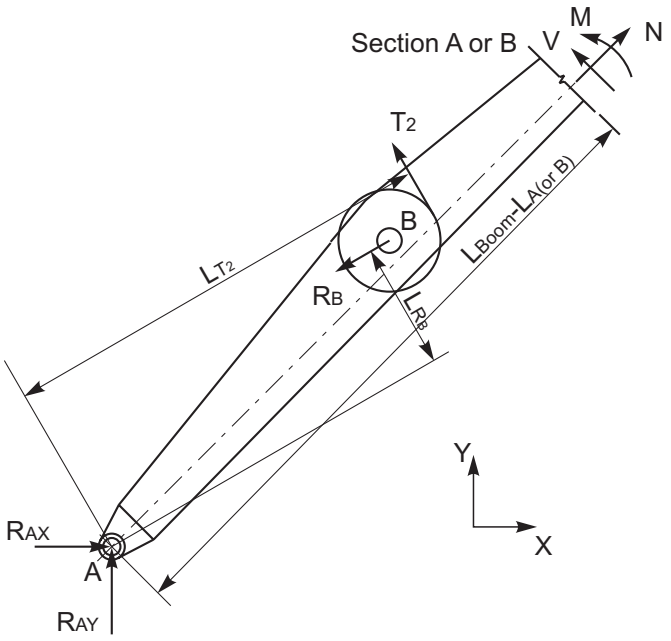

Figure 15 – Free-body Diagram of the Boom

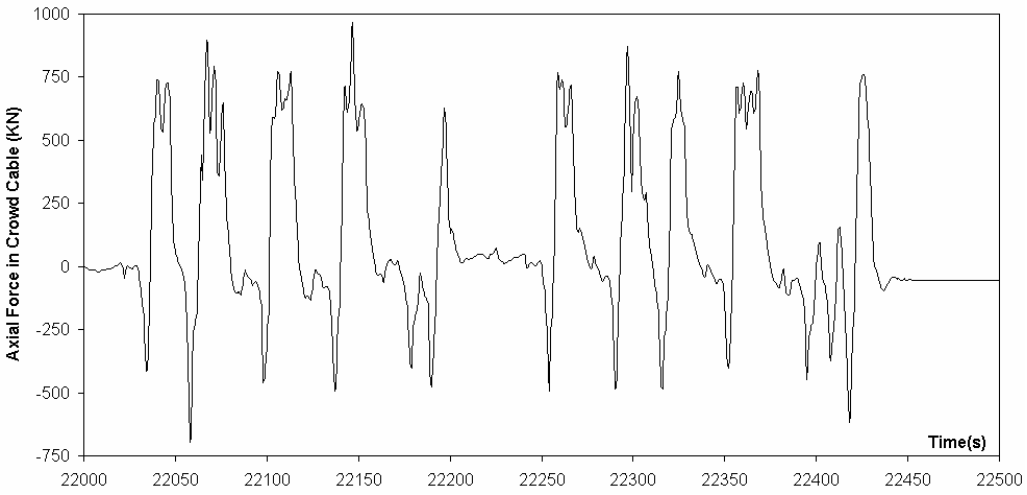

Figure 16 – Axial force in Crowd Cable in 10 Digging Cycles

3.3 Simplified Model of the Boom

The boom can be simplified into a simply supported beam with in-plane forces T_2, R_B and N, as shown in Figure 17. A support in the transverse direction is added at Point E to represent the total cable forces along this direction and the dynamic effect. This simplified model of the boom was used to determine the magnitude of the forces to apply on the FEA model.

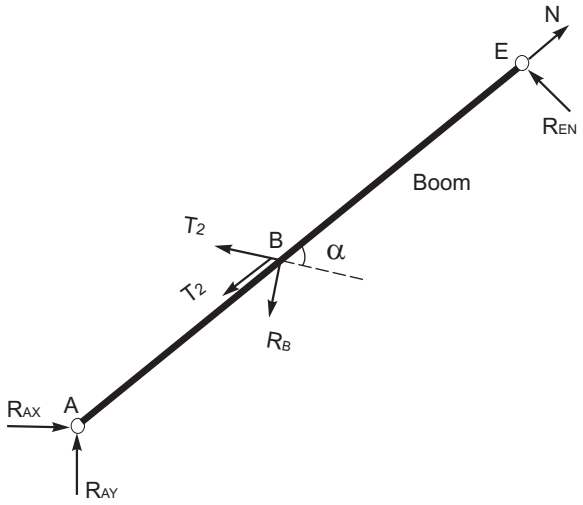

Figure 17 – Simplified Model of the Boom

3.4 Finite Element Analysis of the Boom

A coarse finite element mesh of the boom was developed for a preliminary analysis as shown in Figure 18. Most of the dimensions were obtained from a drawing of the boom provided to the investigators by Syncrude Canada Ltd. Some dimensions were obtained

during a field visit and the top and bottom plates thickness were confirmed by Syncrude field personnel.

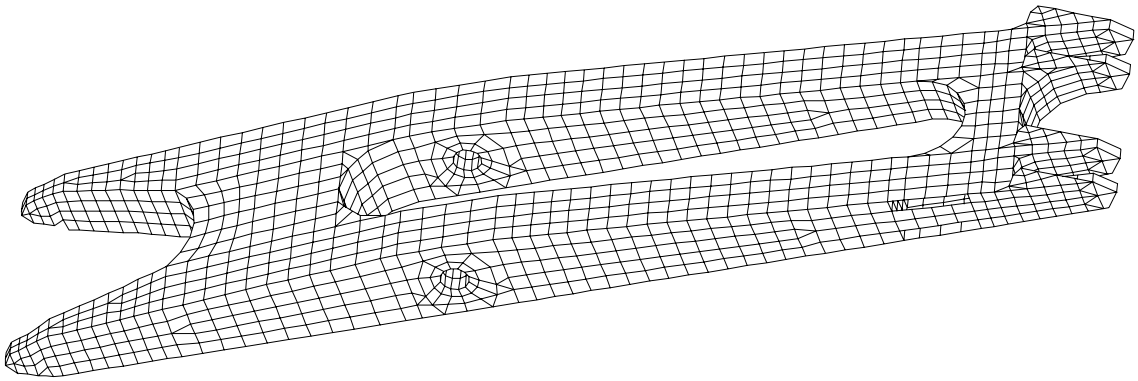

Figure 18 – Finite Element Model of the Boom

Because of symmetry of the boom and loading, the model of Figure 18 was further simplified by breaking it along the line of symmetry. This simplification is justified from the observation that measured strains in both legs of the boom were observed to be similar, thus making the boom symmetrical both in geometry and loading. Only one-half of the boom was modeled as shown in Figure 19. The half boom was discretized using three-node and four-node shell elements implemented in the commercial software ABAQUS. Three pins, one each at points A, B and E (see Figure 19), were modeled using rigid surfaces.

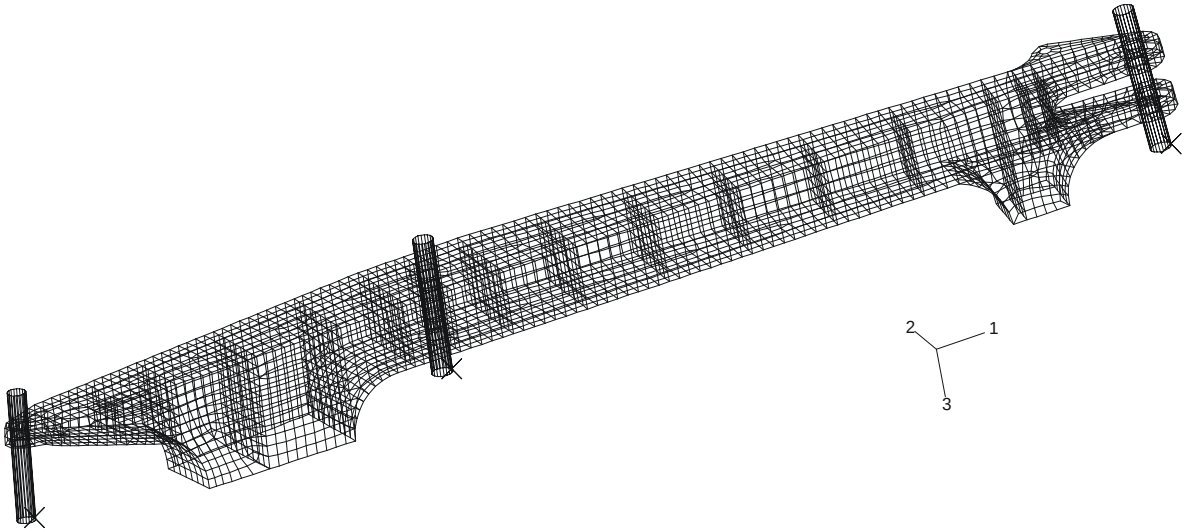

Figure 19 – Refined Mesh Model of the Boom

Validation of the finite element model was performed as follows: from field strain and displacement data and equations of equilibrium, the external forces to the boom were calculated; these forces were used as applied forces on the finite element model; strains at the location of the field strain gauges were then compared with the field measured strains (or section forces derived from the calculated stresses and strains). A significant discrepancy

between the calculated strains and the field measured strains would indicate either that: 1) the finite element model is not the same as the instrumented structure; or 2) the equations of equilibrium used to calculate the external forces from the measured strains are incorrect. Good agreement between the FEA results and the field measurement indicates that the finite element model is representative of the structure monitored in the field and that the equations used to determine the forces applied on the finite element model are correct. The verified finite element model is then used to extrapolate the field measured strains from the locations of measurements to the numerous locations of strain concentration in the boom.

4. Analysis of Field Data

Three unit load cases, as shown in Figure 20, were used to correlate the measured field data and the finite element analysis results. The stress (strain) distributions, $\sigma^1(\varepsilon^1)$, $\sigma^2(\varepsilon^2)$ and $\sigma^3(\varepsilon^3)$, in the boom under the action of these three unit loads were obtained from the finite element analysis.

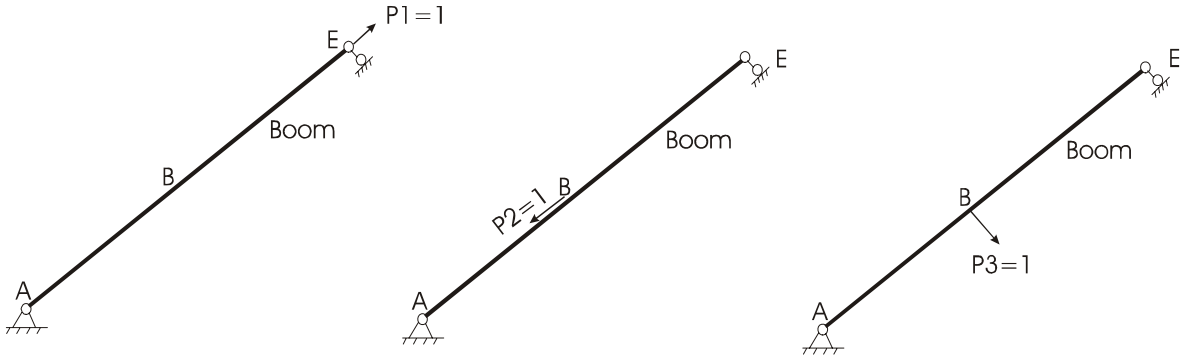

(a) Load case 1 (b) Load case 2 (c) Load case 3

Figure 20 – Basic Load Cases Considered

The stress and strain at any location along the boom and for any combination of forces T_2, R_B and N shown in Figure 17 can be obtained from a linear combination of the unit load analysis results. That is,

$$\sigma = P_1 \cdot \{\sigma\}^1 + P_2 \cdot \{\sigma\}^2 + P_3 \cdot \{\sigma\}^3 \qquad [41]$$

where

$$P_1 = N \qquad [42]$$

$$P_2 = T_2 + T_2 \cos\alpha + R_B \sin\alpha \qquad [43]$$

$$P_3 = R_B \cos\alpha - T_2 \sin\alpha \qquad [44]$$

The variation of longitudinal stress over time in the top and bottom flanges at section B-B was determined using the above equation. Using the stress versus time data, the stress ranges

were counted using the rain-flow counting method. The stress spectrum obtained from this procedure is compared in Figure 21 and Figure 22 to the stress spectrum obtained directly from the strains measured on the boom. Figure 21 presents the stress spectrum for the top flange at section B-B whereas Figure 22 presents the stress spectrum for the bottom flange at the same section. It should be noted that the top and bottom stress ranges were obtained by averaging the strains recorded at the top and the bottom flanges, respectively. Because lateral bending of the boom was negligible, the strain variation in the transverse direction was minimal. Both figures indicate an excellent correlation between the calculated and measured stress ranges. This good agreement indicates that the calculations, which are based on the equations of equilibrium presented above and the finite element model are both correct.

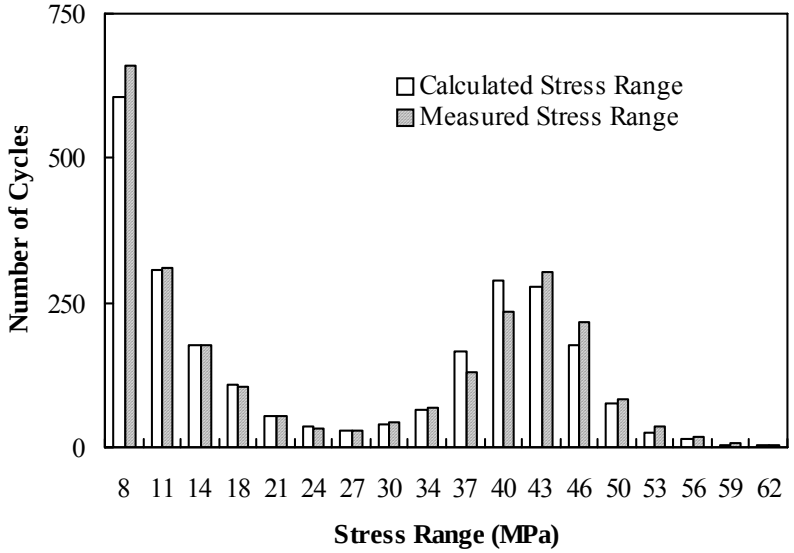

Figure 21 – Longitudinal Stress Range –Top Flange at Section B-B (August 23, 24 hours)

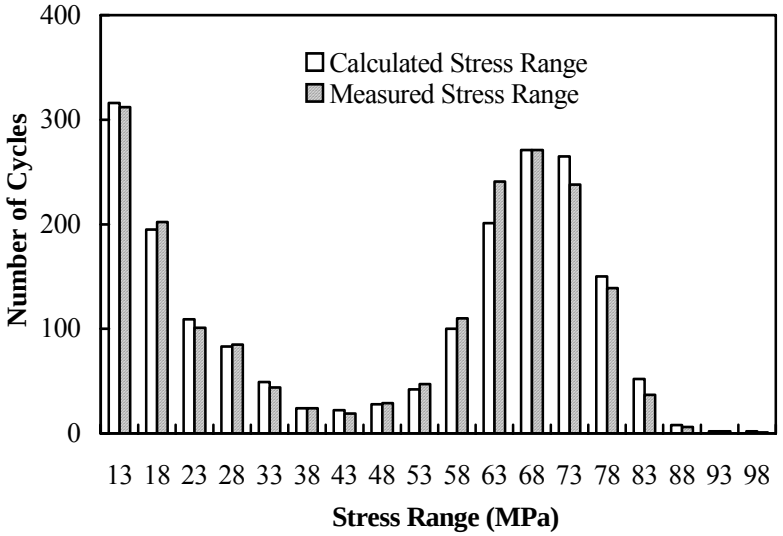

Figure 22 – Longitudinal Stress Range – Bottom Flange at Section B-B (24 hours, August 23)

The stress history at three points on the bottom flange, designated as L_1, L_2 and L_3, as shown in Figure 23, was determined from the finite element analysis. Point L_2 is located along the axis of the saddle block, shown as line 2 in Figure 23, and is at the outer edge of the flange, whereas point L1 is located along the same axis, but on the inner edge of the flange. Point L_3 is located near the inside edge of the flange near the tip of the boom. All three locations represent observed cracking regions. The results of the rainflow cycle counting are presented in Figure 24, where the stress range was normalized by dividing the calculated stress ranges by the maximum stress range at that location. A comparison of these results with the results presented Figure 21 and Figure 22 indicates that the stress spectra have similar distributions. This is expected since the material in the boom did not yield during the loading process and the stresses are directly proportional to the applied load.

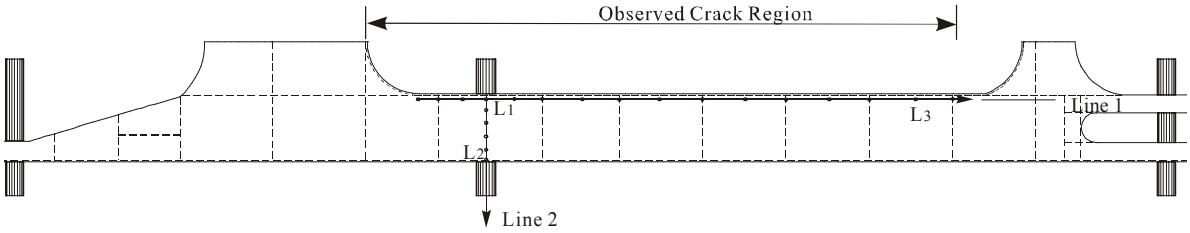

Figure 23 – Locations Studied on the Bottom Flange of the Boom

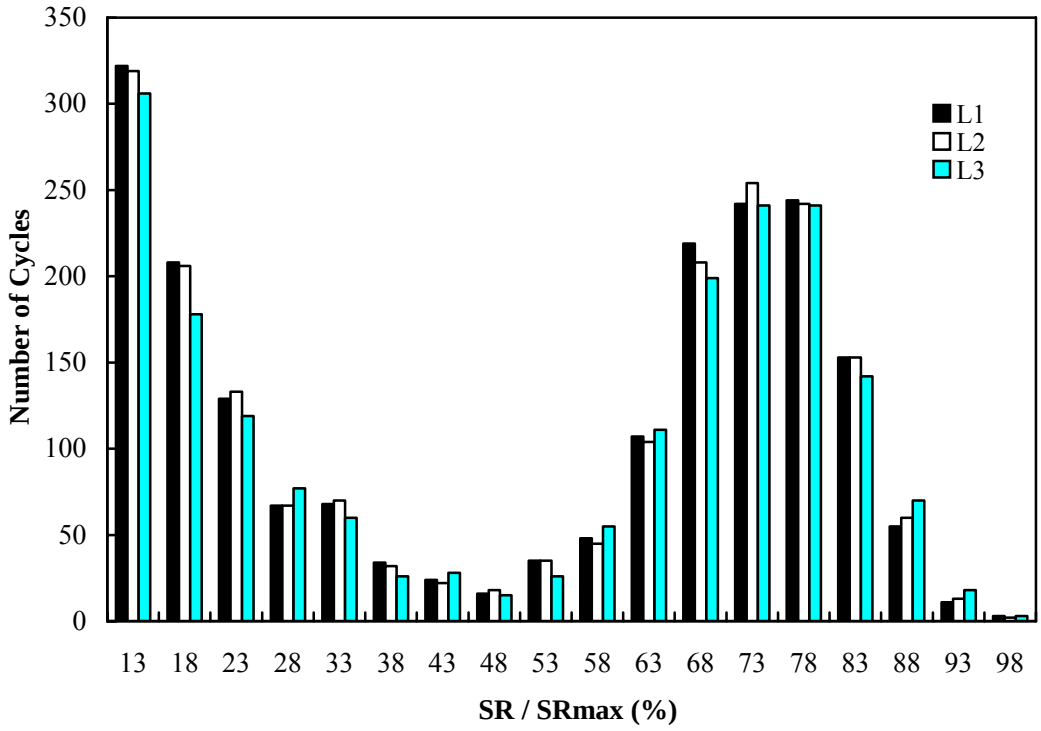

Figure 24 – Longitudinal Stress Ranges at Points L_1, L_2 and L_3 (August 23)

4.1 Equivalent Stress Range and Equivalent Load Range

Calculation of the fatigue life under variable amplitude loading can follow various cumulative damage theories. Although several damage theories have been developed over the years, the one that remains most widely used is the linear damage rule by Palmgren and Miner (Gurney and Maddox, 1990). The Palmgren-Miner model can be used to simplify the variable amplitude fatigue spectrum into a single equivalent stress range. Since the stress spectrum is slightly different for every point on the boom, it is advantageous to simplify the problem by using an equivalent load range on the boom, from which the equivalent stress ranges everywhere in the boom can be obtained from an analysis of the boom under the equivalent load range. This approach needs to be validated for the boom.

An equivalent stress range, which results in the same amount of fatigue damage as the variable stress spectrum, can be obtained using the linear damage rule by Palmgren and Miner. The resulting equivalent stress range takes the following form :

$$\Delta\sigma_e = \sum_{i=1}^{k}\left[\frac{\Delta\sigma_i{}^m n_i}{N}\right]^{1/m} \qquad [45]$$

where $\Delta\sigma_i$ is the i^{th} stress range in the spectrum, which occurs n_i times and N is the total number of stress cycles, namely, $N=\sum n_i$. The derivation of this equation is based on the Palmgren-Miner model and has been demonstrated elsewhere (Fisher *et al*., 1998). The constant *m* is the slope of the S-N curve, which is usually taken as 3. However, a more accurate value of the material constant *m* can be obtained from crack growth rate tests. The boom was made of 350WT steel and eight crack growth rate tests were conducted to determine its crack growth rate characteristics. From the crack growth rate test results presented in section 5, an average value of *m* was found to be approximately 3.3 for this steel. The value of *m* was found to be dependent on the mean stress level and varied from 3.03 to 3.59 as the load ratio increased from 0.1 to 0.5.

The equivalent stress ranges along two lines (lines 1 and 2 shown in Figure 23) along and across the bottom flange of the boom were calculated using equation [46] with $m = 3.3$. A plot of the variation of the equivalent stress range along these two lines is presented in Figure 25.

Figure 25(b) indicates that the equivalent stress range decreases as be move closer to the tip of the boom. Greater fatigue damage is therefore expected to take place near the radius between the boom leg and transverse tie.

Reference to figures 21 to 23 indicates that the fluctuations are due to the presence of the internal diaphragms. Figure 25(b) indicates only a very small variation of the stress range across the width of the bottom flange of the boom.

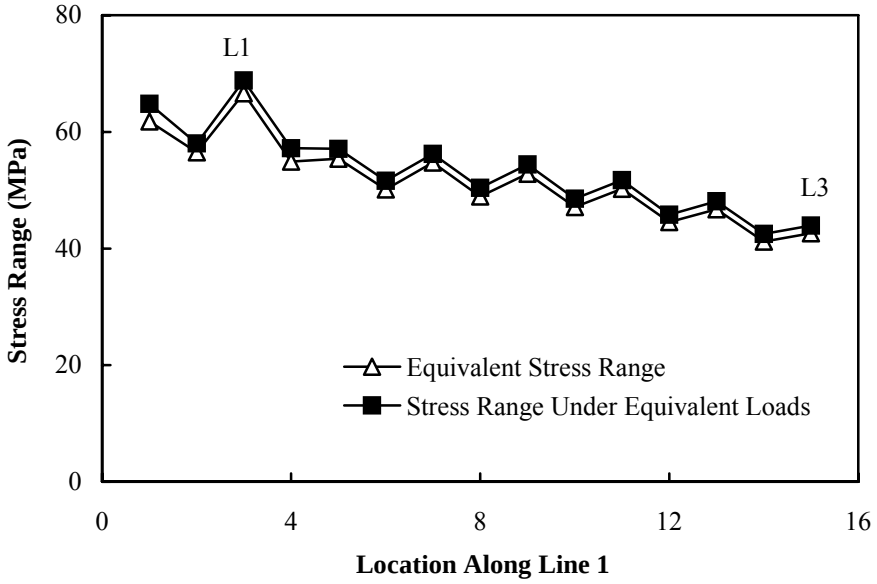

(a) Along the length of the boom (along Line 1 in Figure 23)

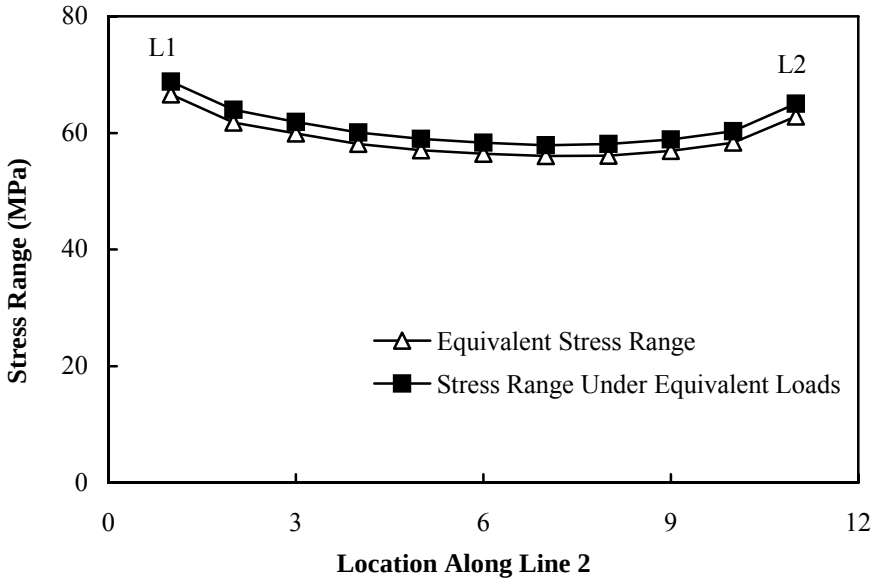

(b) Across the width of the boom (along Line 2 in Figure 23)

Figure 25 – Stress Range Variation on the Bottom Flange of the Boom

In order to simplify the calculation of the equivalent stress range for every stress point on the boom, equivalent load ranges corresponding to the force degrees of freedom P_1, P_2 and P_3

shown in Figure 20 were calculated using the Palmgren-Miner rule approach. This results in an equation similar to the equivalent stress range presented above where the stress range is replaced by a load range. The same constant $m = 3.3$ was used for the calculation of the equivalent load ranges. The stress ranges under these equivalent loads, P_{1E}, P_{2E} and P_{3E}, can be determined simply by loading the finite element model with the equivalent load ranges. A comparison of the equivalent stress ranges obtained using this approach and the previous approach outlined above is presented in Figure 25. The equivalent stress ranges obtained by the simplified approach are in good agreement with the equivalent stress ranges obtained by looking at individual points on the boom. The equivalent stress ranges, obtained using the simplified approach, are slightly conservative compared to the point-by-point approach.

The equivalent principal stress range and axial stress range in the bottom flange, outside web and inside web are presented in Figure 26, Figure 27, and Figure 28, respectively. The stresses shown in the legend are twice the stress range in kPa.

A comparison of figure (a) with figure (b) in each of Figure 26, Figure 27, and Figure 28 indicates only minor differences between the principal stresses and the axial stresses. This indicates that the stresses in the boom are primarily axial. The locations of high stresses, indicated in red, are in areas where fatigue cracks have been detected in the booms. The maximum equivalent stress range, obtained using the mesh shown in Figure 19, is approximately 70 MPa. Because of the relatively coarse mesh used at this stage of the analysis, the stresses obtained from the mesh of Figure 19 do not account for localized stress concentrations expected at the diaphragm welds. Further mesh refinement is required to assess these localized stresses.

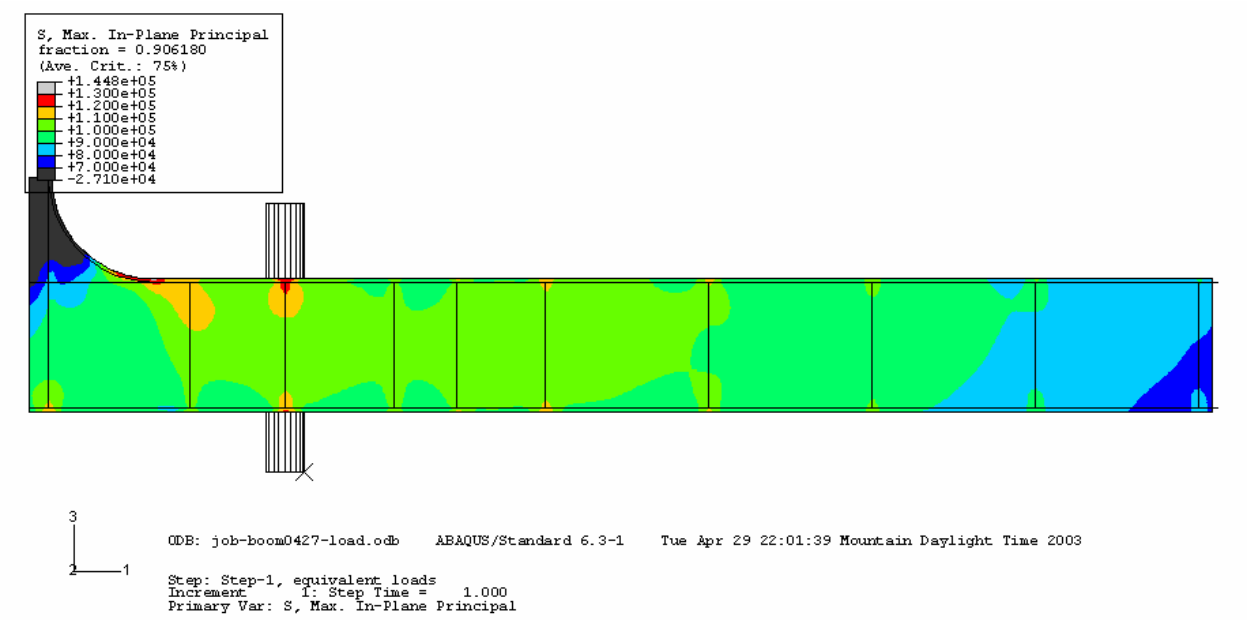

(a) Major principal stresses

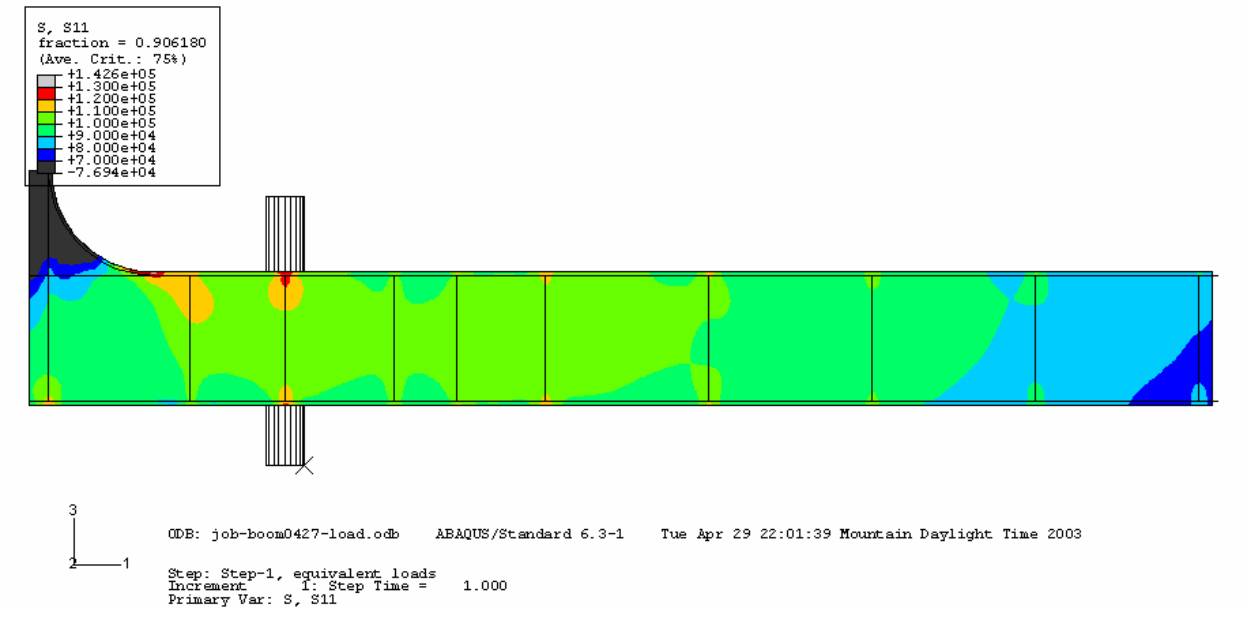

(b) Axial stresses

Figure 26 – Equivalent Stress Ranges in the Bottom Flange of the Shovel Boom

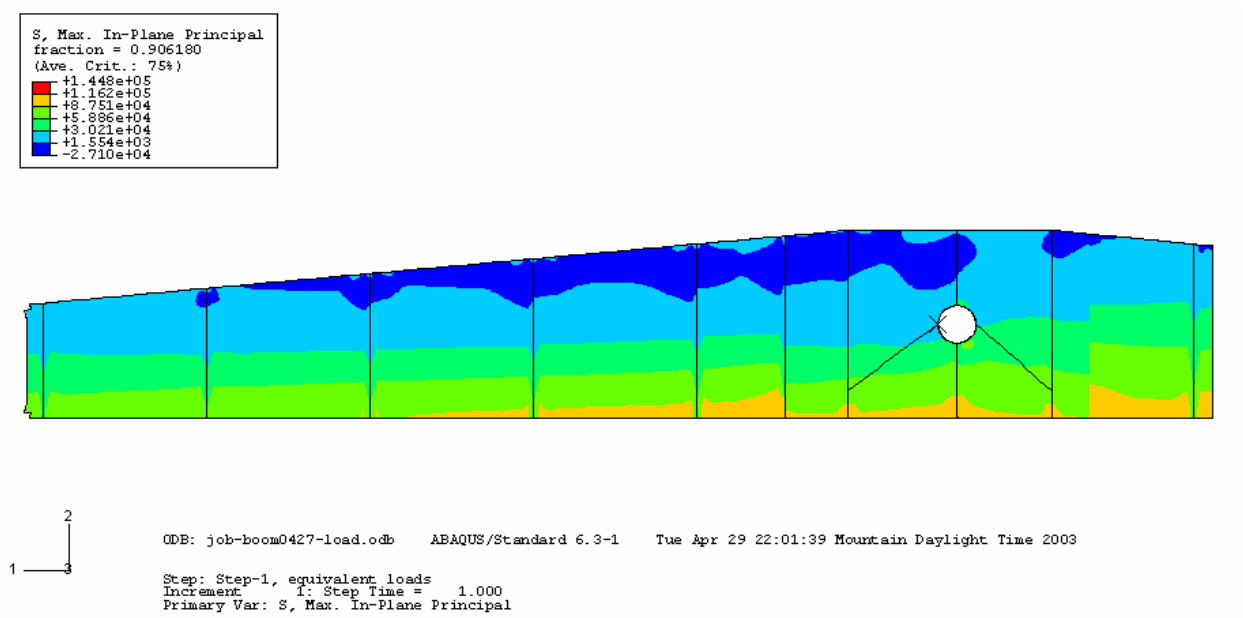

(a) Major principal stresses

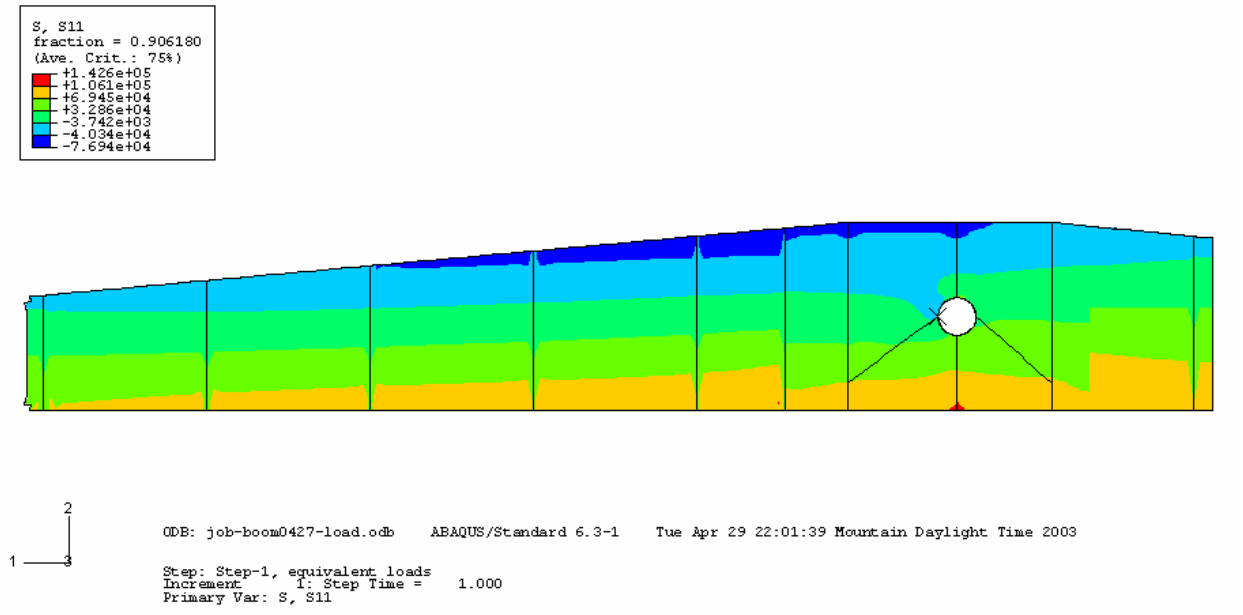

(b) Axial stresses

Figure 27 – Equivalent Stress Ranges in Exterior Web of Shovel Boom

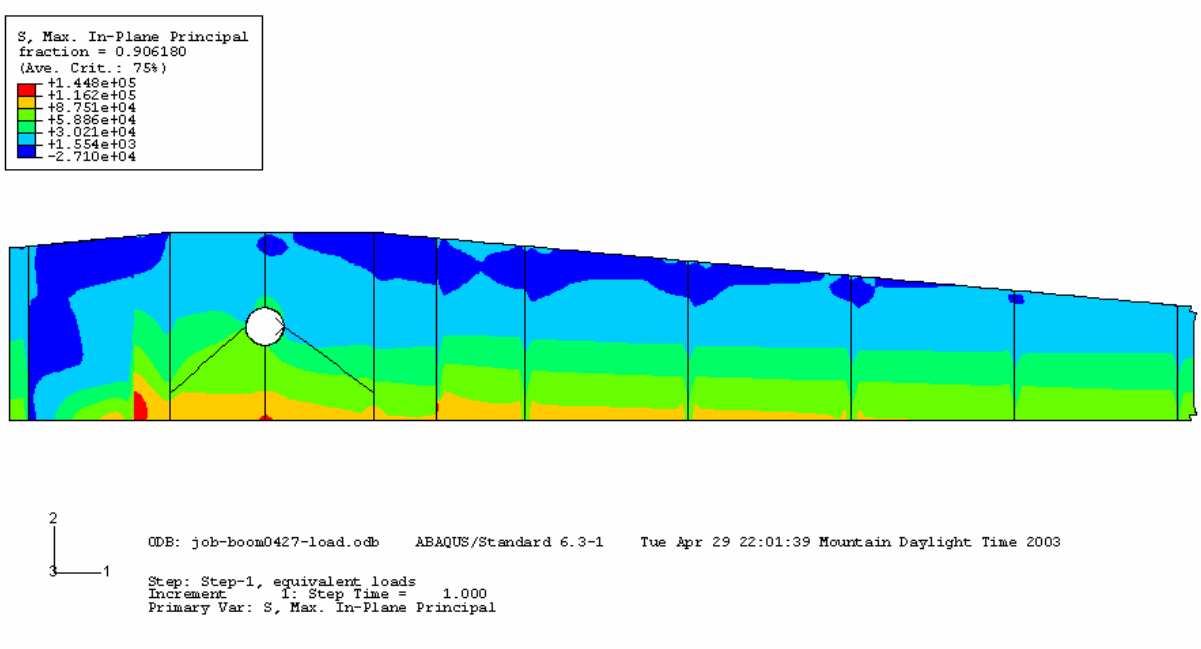

(a) Major principal stresses

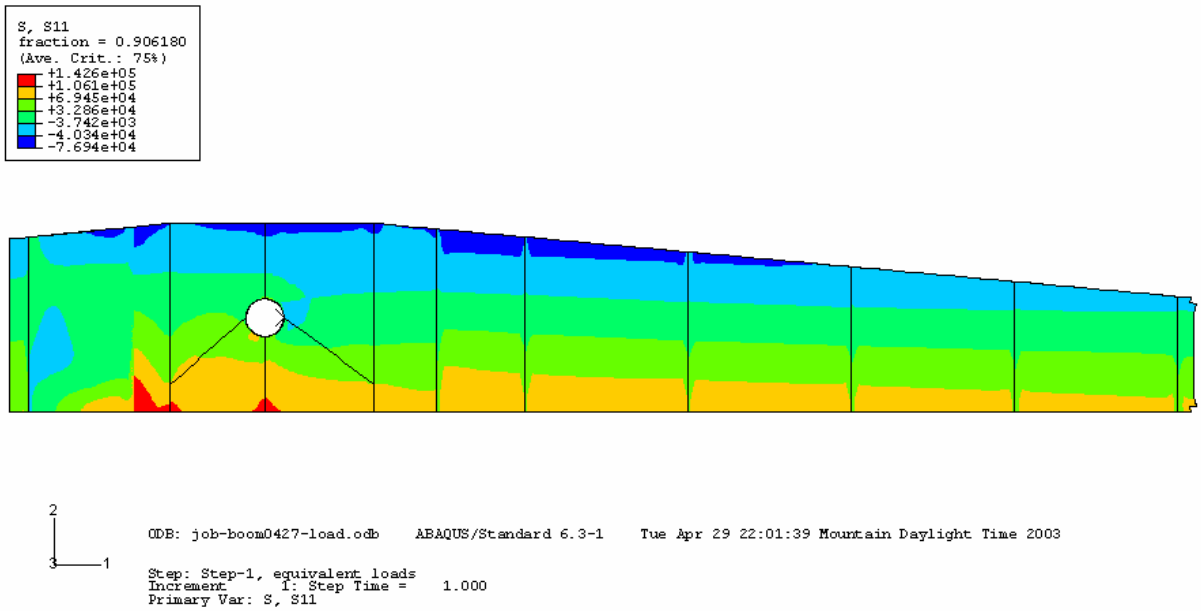

(b) Axial stresses

Figure 28 – Equivalent Stress Ranges in the Interior Web of Shovel Boom

5. Material Testing

The steel used for major repairs of the boom is usually of grade G40.21 350WT. Since toughness is affected by material thickness, it was decided to use a 38 mm steel plate, which represents the upper bound of plate thickness used for repairs of the boom. After two unsuccessful attempts to get the correct grade of steel, a steel plate was finally obtained with the properties that satisfied the requirements for Grade 350WT steel. The grade of steel was confirmed from Charpy V-notch impact tests and tension coupon tests. The average energy absorption from three Charpy specimens was 136 J at –45˚ C, which satisfies the toughness requirement for Grade WT steels. The results of three tension coupon tests are presented in Figure 29. The mean static yield strength was measured at approximately 365 MPa, which satisfies the requirement for grade 350 steel.

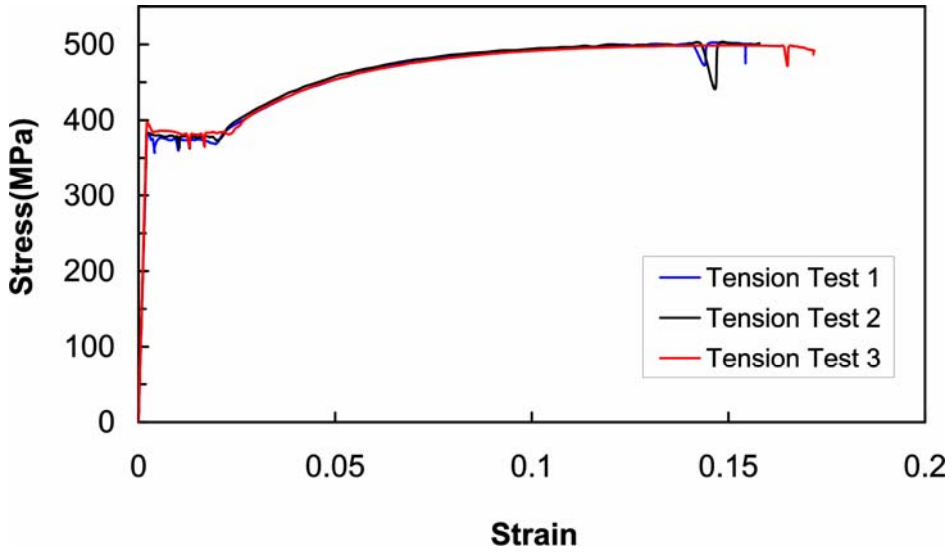

Figure 29 – Tension Coupon Test Results

5.1 Fatigue properties

The fatigue properties required for the fatigue life prediction of the electric shovel boom are fatigue crack initiation behaviour, crack growth rate characteristics, and fracture toughness (at room temperature and –50˚ C).

The crack growth rate tests were conducted using a single edge crack specimen as shown in Figure 30. A total of 12 specimens, shown in Figure 31, were machined from the G40.21 350WT steel plate obtained for this investigation. The testing procedure consists of cyclically loading the test specimen in a tension testing machine until a fatigue crack initiates from the machined notch. Once a fatigue crack has initiated the crack growth rate test is started. The tests were conducted at pre-determined stress ranges and mean stresses. The crack length and number of cycles applied from the beginning of the test were measured at regular intervals. The crack length was measured using a high magnification digital

camera purchased by Syncrude Research for this project. The testing protocol and control software used to conduct these tests were developed using dummy specimens. The crack growth rate test fixture and a typical test specimen are shown in Figure 32 and Figure 33.

The results of crack growth rate tests conducted at two different stress ranges and two different mean stresses are presented in Figure 34. The results are presented in terms of crack growth rate (in m/cycle) versus stress intensity factor range (in $MPa\sqrt{m}$) on logarithmic scales. Since all test results fell within a narrow band it is concluded that the effect of mean stress is negligibly small for the range used in this investigation. It should be noted that the effect of stress range is directly accounted for in the calculation of the stress intensity factor range. As the curves in Figure 33 demonstrate, the stress range is an important factor.

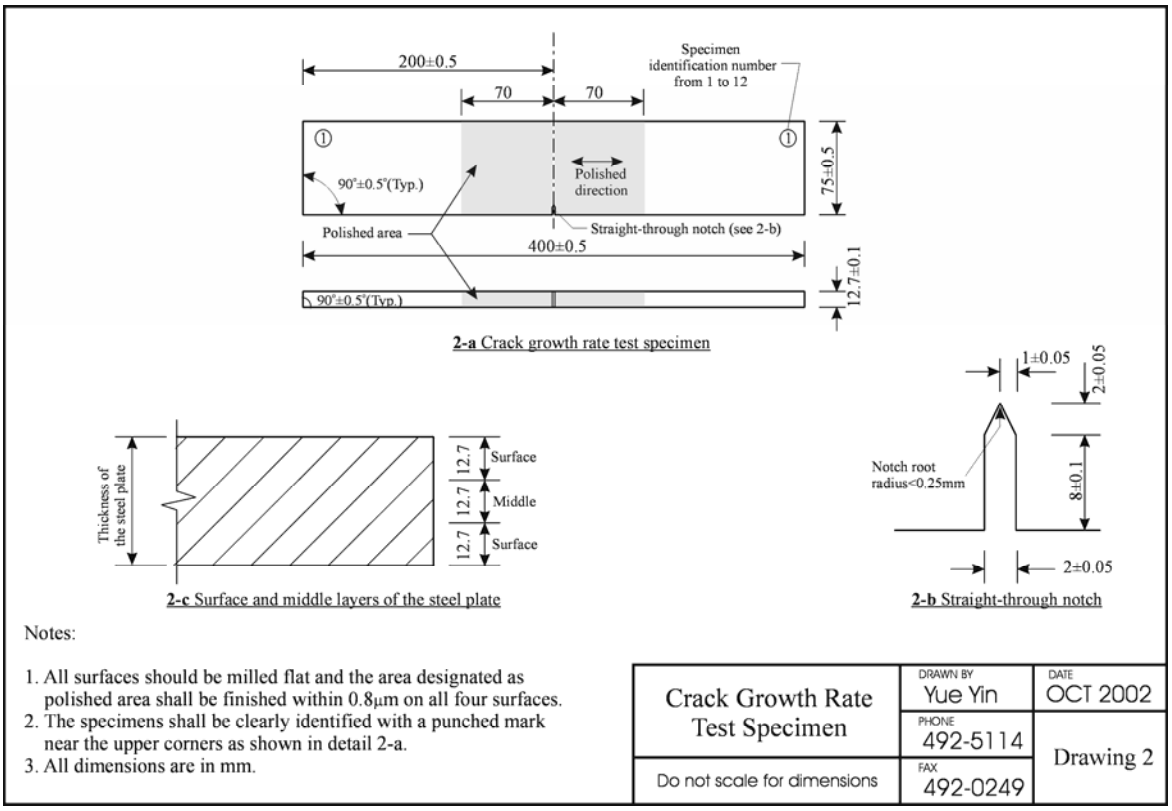

Figure 30 – Fatigue Crack Growth Rate Test Specimen

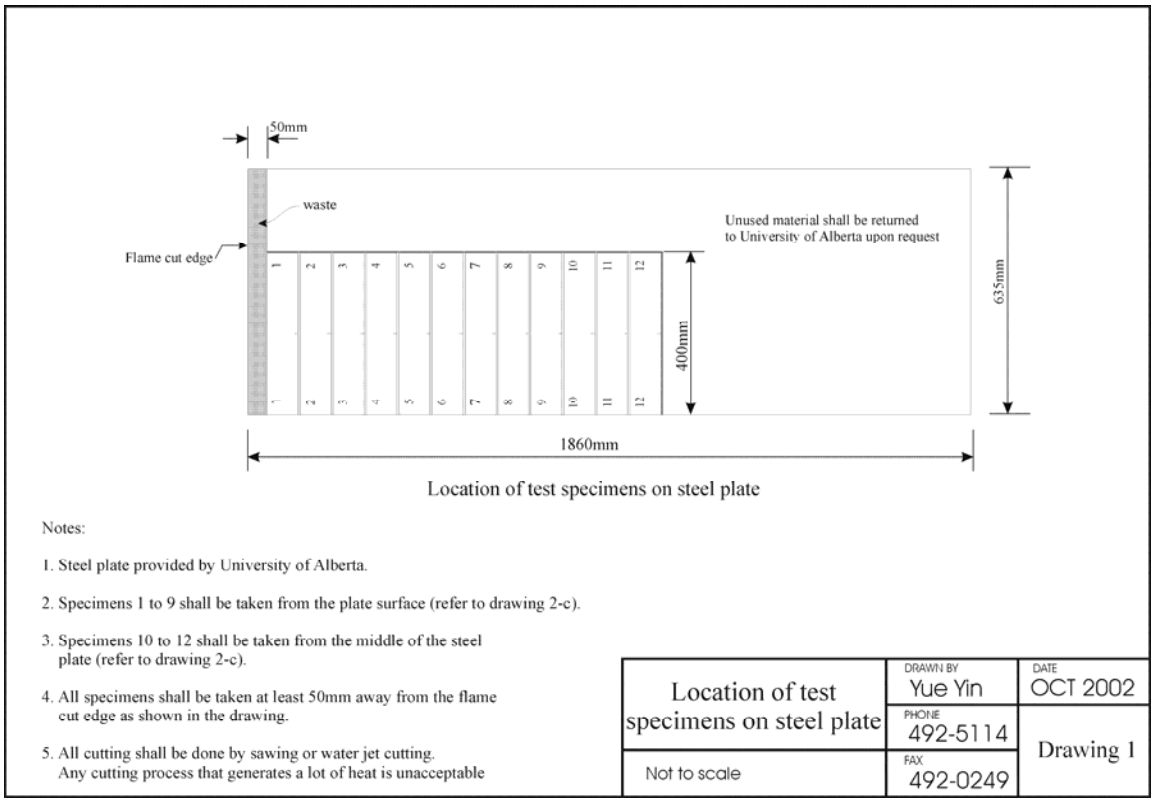

Figure 31 – Location of Crack Growth Rate Test Specimens

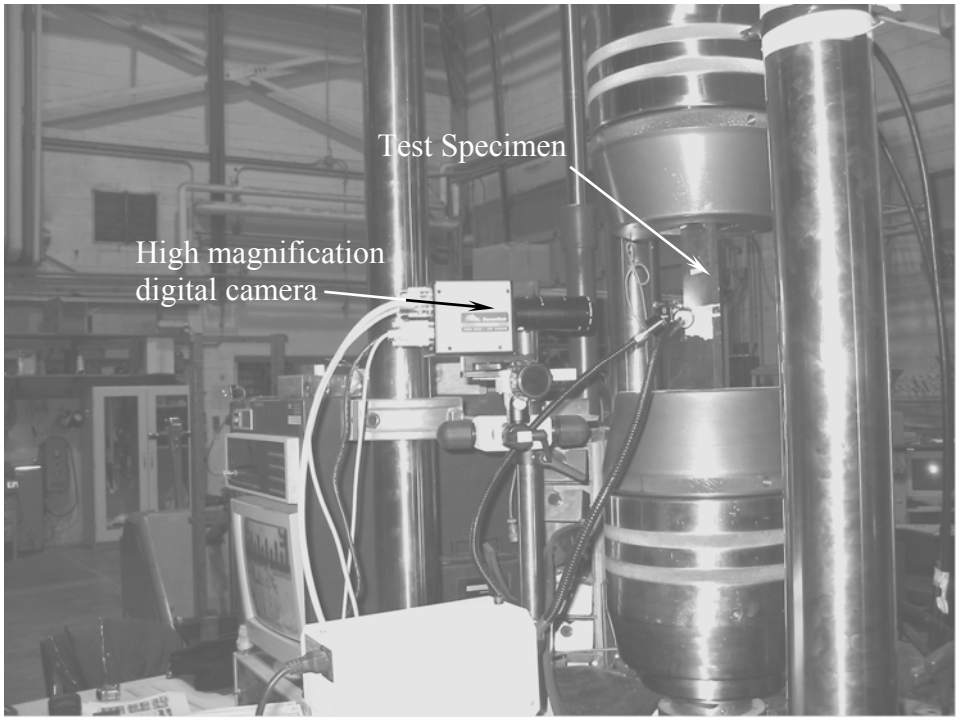

Figure 32 – Test Setup for Crack Growth Rate Measurement

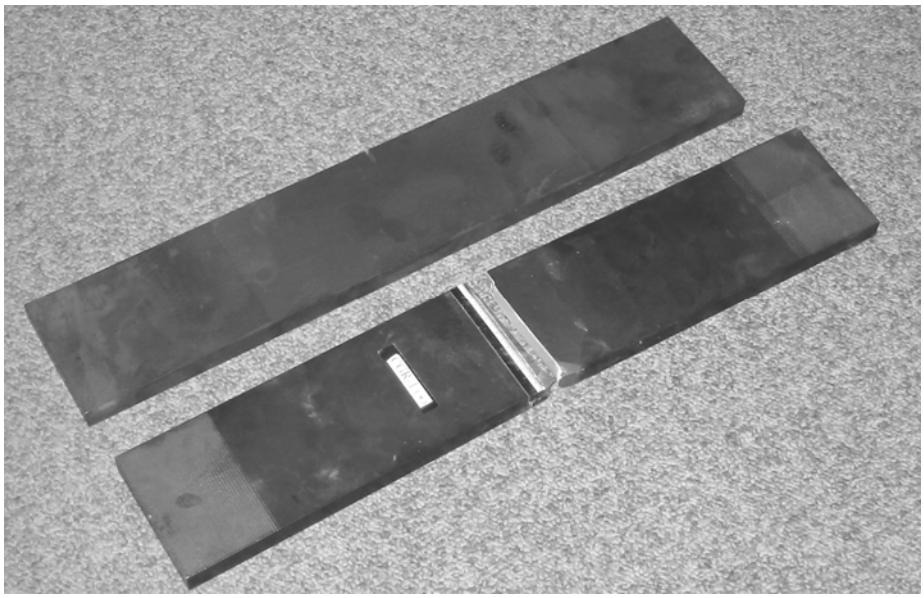

Figure 33 – Crack Growth Rate Test Specimens Before and After Fracture

The crack growth rate test results are presented in Figure as the log of crack growth rate versus the log of the stress intensity factor range. As expected, the plotted data indicate that the relationship between log crack growth rate and log stress intensity factor range is almost linear. A linear regression analysis was therefore conducted on the test data to obtain the crack growth rate equation required to assess the rate of crack propagation in the shovel boom. From a linear regression analysis, the crack growth rate equation obtained from the test specimens tested at a load ratio of 0.1 was:

$$\frac{da}{dN} = 8.88 \times 10^{-12} \left(\Delta K\right)^{3.03} \qquad [46]$$

For a load ratio of 0.5, the crack growth rate equation is as follows:

$$\frac{da}{dN} = 2.89 \times 10^{-12} \left(\Delta K\right)^{3.59} \qquad [47]$$

The average of all the crack growth rate tests is:

$$\frac{da}{dN} = 5.89 \times 10^{-12} \left(\Delta K\right)^{3.27} \qquad [48]$$

where, da/dN is the crack growth rate expressed in m/cycle and ΔK is the stress intensity factor range expressed in $\mathrm{MPa}\sqrt{\mathrm{m}}$.

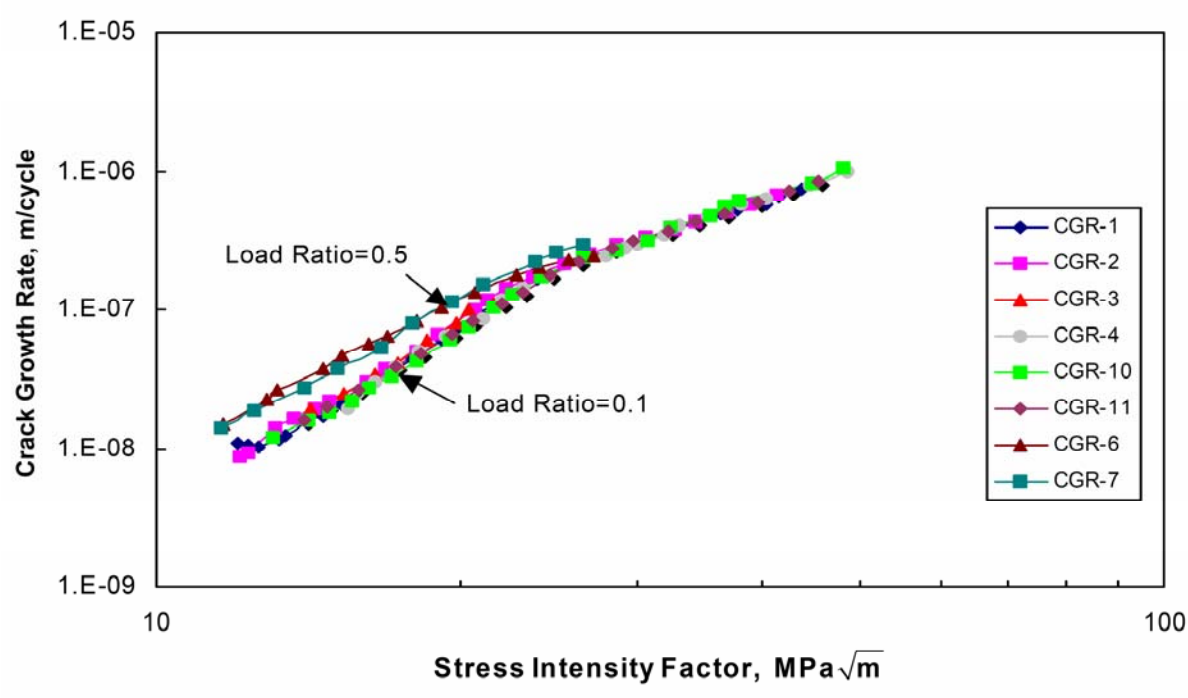

Figure 34 – Crack Growth Rate Test Results

5.2 Fracture toughness tests

To predict the remaining fatigue life of a cracked structure, the toughness of the material is also needed to decide when the crack will cause fracture. Since toughness is affected by material thickness, a 38 mm steel plate, which represents the maximum plate thickness used in the shovel boom, of grade CSA-G40.21-350WT, was used for the fracture toughness tests. This grade of steel is the grade usually specified for boom repair material.

Fracture toughness tests were conducted in accordance with ASTM Standard E1820. Three-point bend specimens of 304×76×38 mm were machined with a 35mm long notch at mid-span and perpendicular to the rolling direction. The geometry of the notch was in accordance with the governing ASTM standard. Four tests were carried out, namely, one at room temperature and three at -50°C. The test procedure consists of pre-cracking the test specimen in a three-point bending setup under cyclic loading until a fatigue crack initiates from the machined notch. Once a fatigue crack reaches the desired length set by the standard, the fracture toughness test was started. In order to obtain the J-based resistance curve from a single specimen, unload-reload sequences are applied to the specimen to produce crack extension measurements. The pre-cracking procedure was monitored with a high magnification digital camera. A clip gage and a LVDT were used to measure the crack mouth opening displacement and load line displacement, respectively. The fracture toughness test fixture is shown in Figure 35.

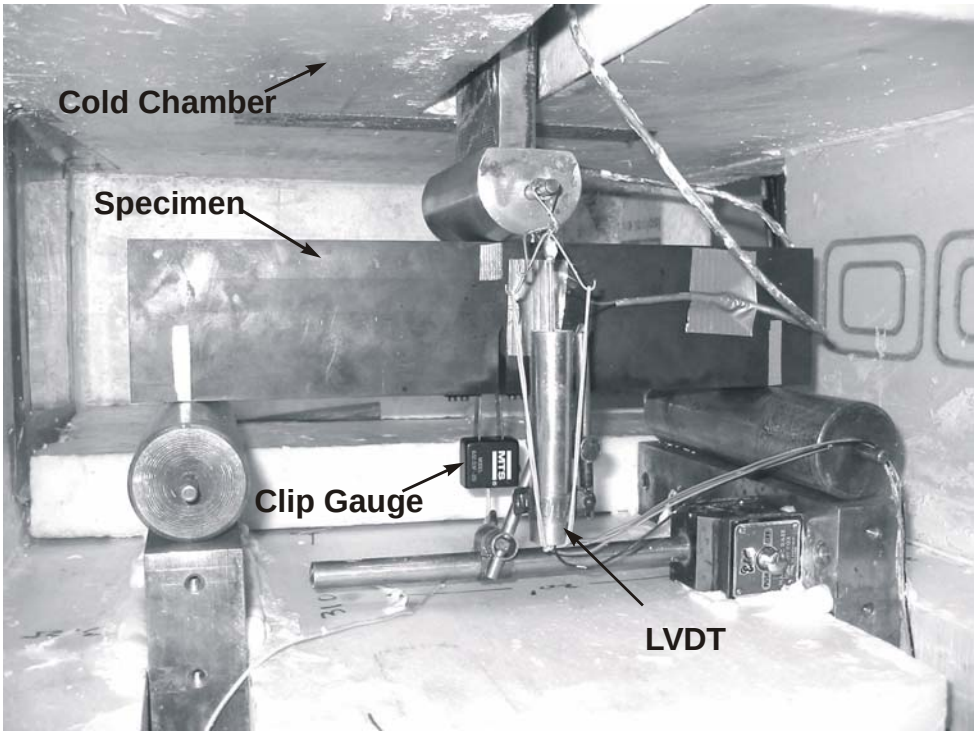

Figure 35 – Fracture Toughness Test Fixture

The first test was performed at room temperature and, as expected, the material displayed very high ductility. No crack extension or fracture occurred until the full section of the specimen had yielded and the test was terminated because the clip gage ran out of range. The load versus load line displacement curve is shown in Figure 36.

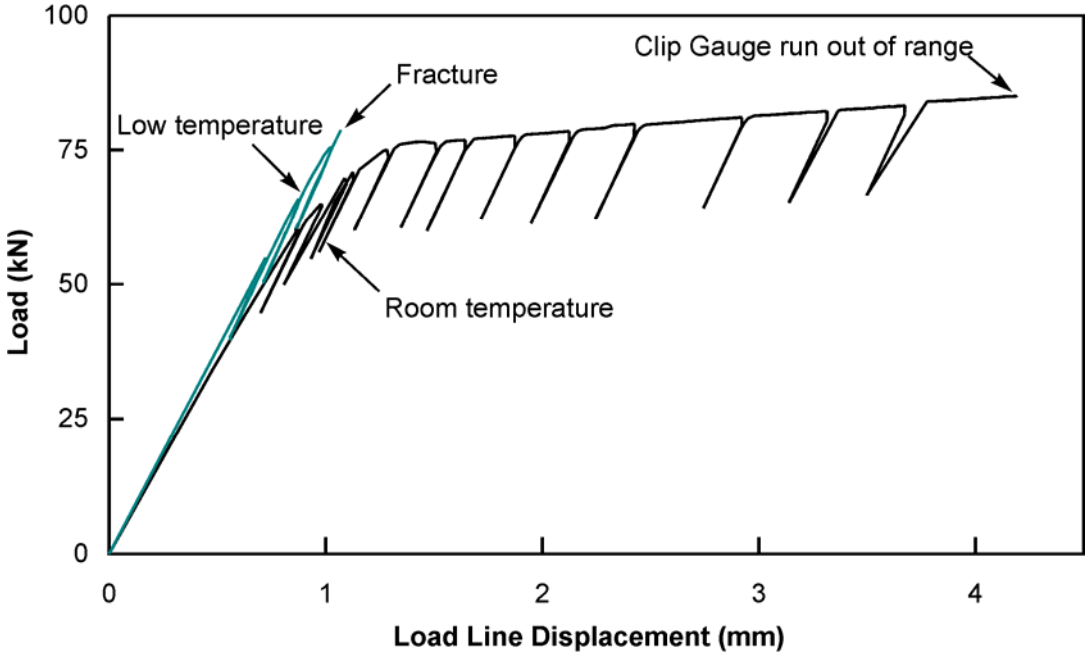

Figure 36 – Load-displacement Curve of Fracture Toughness Test

Since fracture toughness decreases with temperature, the following three fracture toughness tests were performed at -50°C, considered to be close to the lowest temperature under which the shovel would operate. After pre-cracking, the test specimens were placed in an environmental chamber and the temperature was lowered to -50°C with dry ice. Two thermistors were mounted on the specimen close to the crack tip to measure the temperature of the specimens; one on the front surface and the other on the back surface. The temperature was controlled by adjusting the speed of three fans in the cold chamber. An overall view of a test specimen in the environmental chamber is shown in Figure 37.

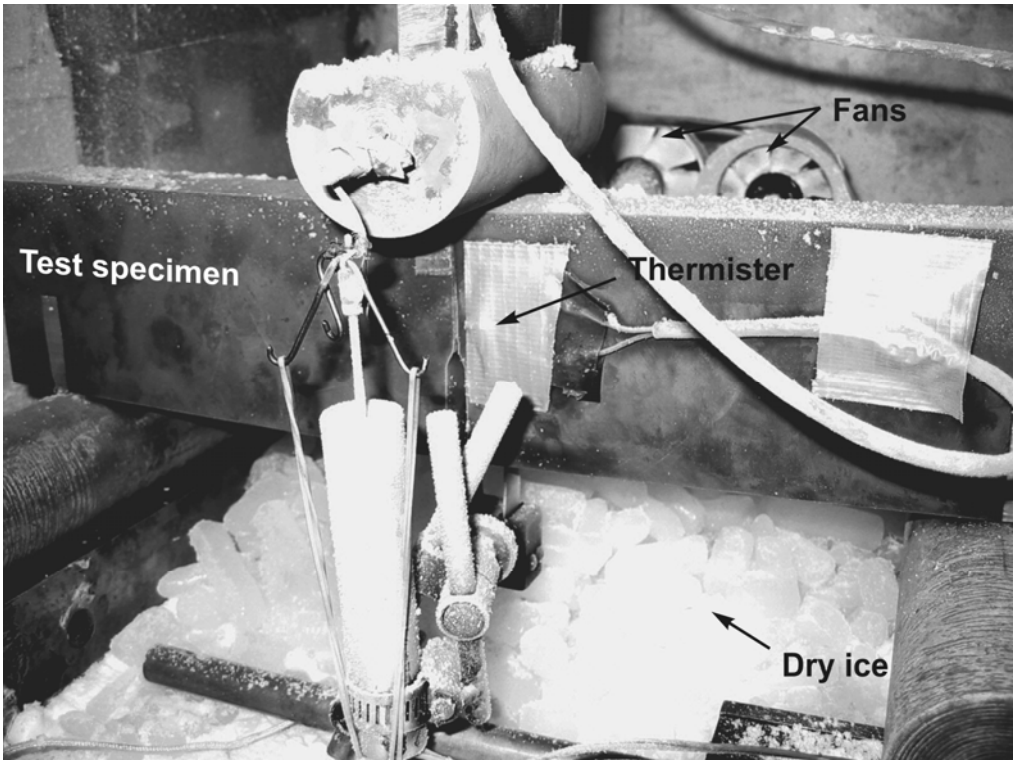

Figure 37 – Fracture Toughness Test Under Low Temperature

Brittle fracture occurred at small load line displacement as shown in Figure 38. The load versus crack mouth opening displacement curves of the three low temperature tests agree very well as shown in Figure 38. The constant gradient of the unload line shows that no crack extension occurred before fracture of the specimens. The specimens fractured under normal temperature and low temperature are compared in Figure 39: plastic tearing occurred at room temperature whereas unstable fracture occurred at low temperature (-50°C).

Because no crack extension was observed before specimen fracture, according to ASTM Standard E1820, the fracture toughness of the material can be calculated for 3-point bending specimens as follows:

$$K = \frac{P_Q S}{(B\,B_N)^{1/2} W^{3/2}}\, f(a/W) \qquad [49]$$

where,

S is the span length of the test specimen,

a is the initial crack length,

B, B_N and *W* are the thickness, net thickness and width of the specimen

P_Q is a load value determined from the load versus crack mouth opening curve, which equal to the maximum load for the above three tests.

and,

$$f(a/W) = \frac{3\sqrt{a/W}\left[1.99 - (a/W)(1-a/W)\left(2.15 - 3.93(a/W) + 2.7(a/W)^2\right)\right]}{2(1+2a/W)(1-a/W)^{3/2}} \qquad [50]$$

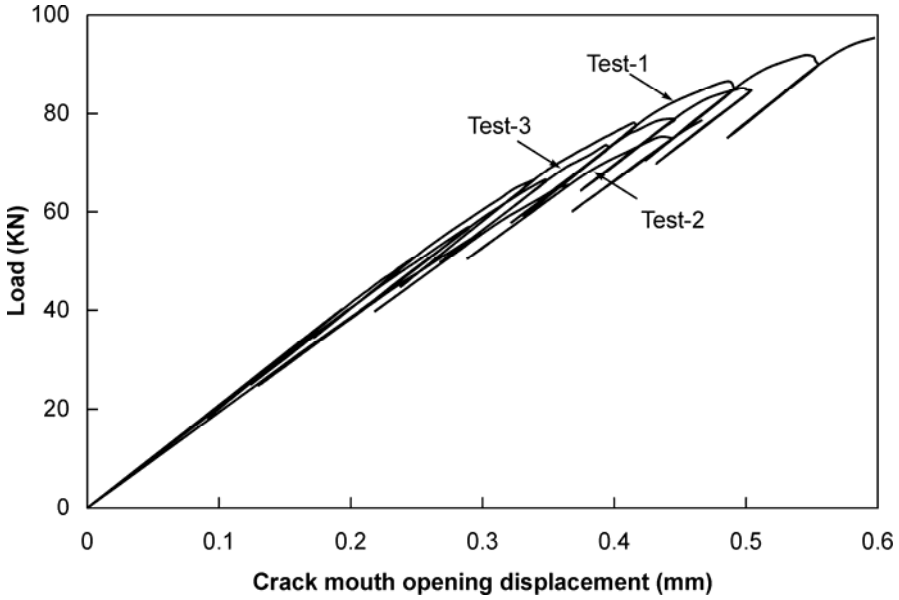

Figure 38 – Low temperature fracture toughness test results

The fracture toughness calculated for the three low temperature tests are $98.9\,\text{MPa}\sqrt{\text{m}}$, $87.3\,\text{MPa}\sqrt{\text{m}}$ and $92.1\,\text{MPa}\sqrt{\text{m}}$ respectively and the average value of fracture toughness at low temperature is $92.8\,\text{MPa}\sqrt{\text{m}}$. This toughness value does not meet the requirements to be plane-strain fracture toughness, but can be safely used with steel plates thinner than 38 mm.

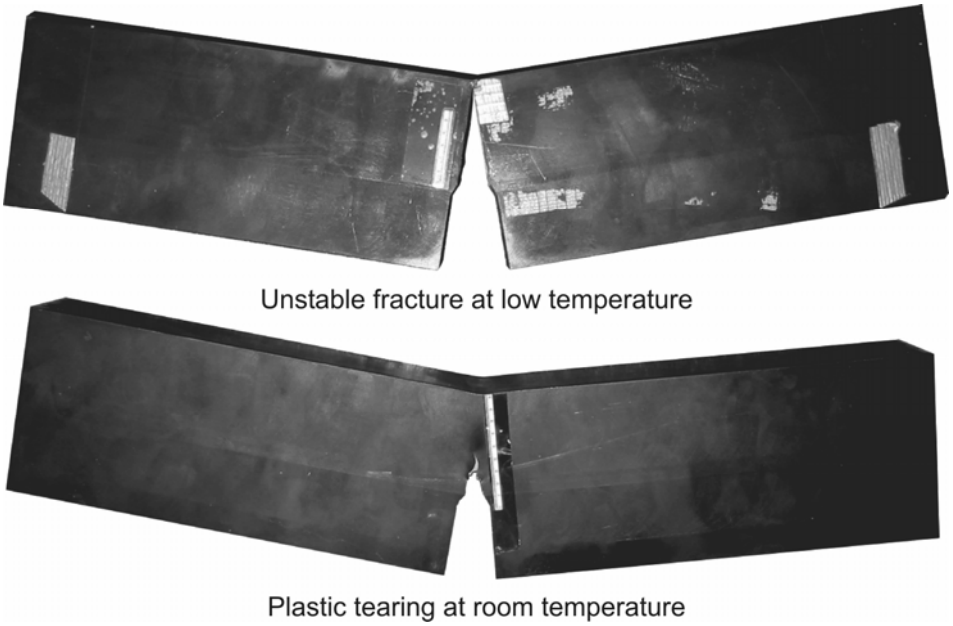

Figure 39 – Fractured specimens

6. Fracture Mechanics Analysis of the Boom

6.1 Introduction

Section 3.3 presented a simplified model of the boom structure with three applied loads and reaction forces at the base and at the tip of the boom as shown in Figure 40. The equivalent load ranges were calculated as $P_{1E} = 3525$ kN, $P_{2E} = 1299$ kN and $P_{3E} = 904$ kN, and the corresponding number of cycles is 2880 cycles per day.

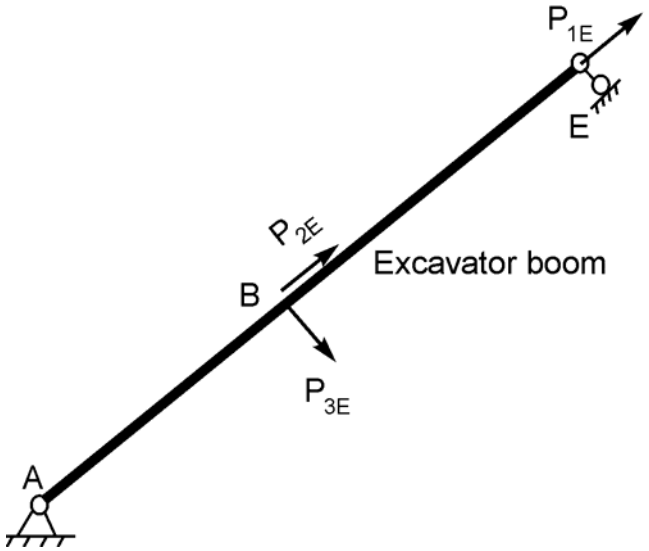

Figure 40 – Equivalent loads on the boom

According to field inspection reports, fatigue cracking of the shovel boom has been a common occurrence during the entire life of the shovel. The inspection reports indicate that most cracks initiate at the toe of the diaphragm-to-flange weld and extend into the web plate, forming a through-thickness corner crack with a crack tip in the web and a crack tip in the flange of the boom (see Figure 41). All the cracks reported in the inspection reports have been reported in the *crack region* identified in Figure 42. This observation is consistent with the results of the finite element analysis presented in section 4.1. The following work will therefore concentrate on cracks in this part of the boom only.

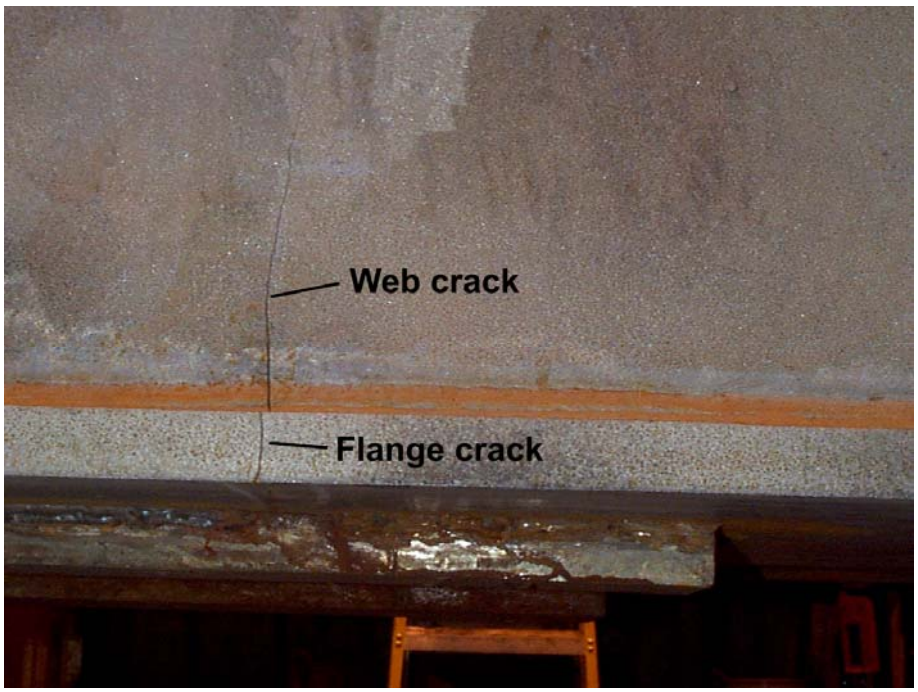

Figure 41 – Through-thickness corner crack in the boom

A fracture mechanics approach is used to determine the growth rate of fatigue cracks in the boom. The fracture mechanics approach is based on the observation that the logarithm of the crack growth rate, da/dN, is directly proportional to the logarithm of the stress intensity factor range, ΔK, in the stable crack propagation range. The crack growth rate equation, known as the Paris model, takes the following form:

$$\frac{da}{dN} = a(\Delta K)^m \qquad [51]$$

where a and m are material constants presented in section 5.1.

In order to make use of equation [51] we must evaluate the stress intensity factor range, ΔK, which is a function of several factors such as, geometry of the object in which the crack is located, the stress magnitude and distribution, and geometry of the crack. The stress intensity factor range can be calculated using the following equation:

$$\Delta K = \beta_E \beta_S \beta_W \beta_G \Delta\sigma \sqrt{\pi a} \qquad [52]$$

where $\Delta\sigma$ is the far field stress range, β_E is correction factor for crack shape, β_S is a surface correction factor for edge or surface cracks, β_W is a finite width (or thickness) correction factor, β_G is a stress gradient correction factor, and a is the crack size. All the parameters β equal to 1.0 for a through thickness crack in an infinitely wide plate subjected to a uniform far field stress. The β values correct for other conditions (crack shape, crack location, finite size of plate and stress distribution). Values of β have been published for several conditions and can be found in various sources. However, in order to use the values of β available in the literature for the boom project, a number of assumptions would have to be made. For this reason, another approach is required to determine the stress intensity factor range for cracks in the shovel boom.

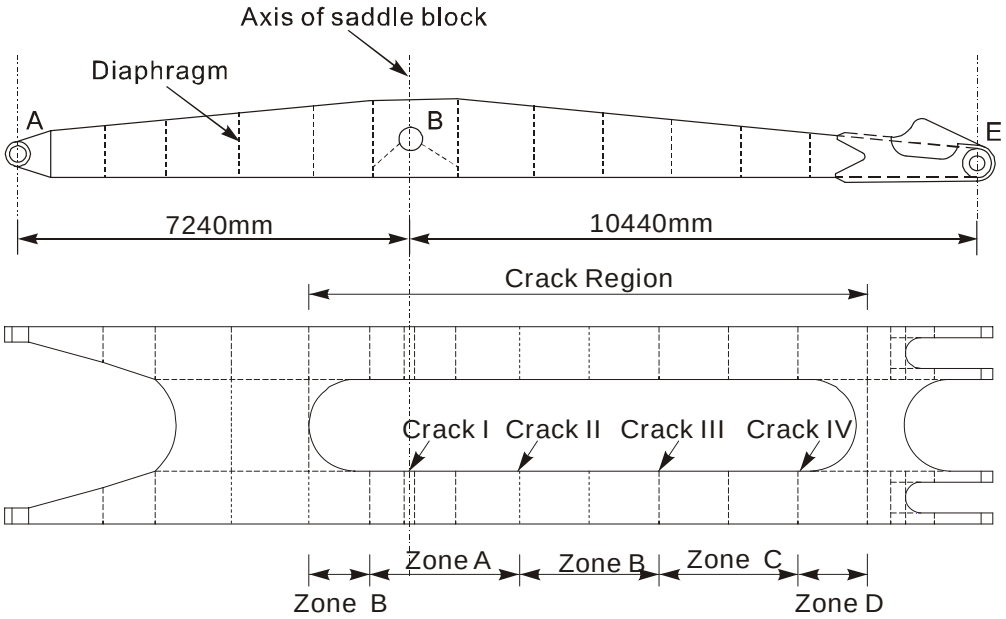

Figure 42 – Various Cracking Zones in the Boom

A finite element approach was used to calculate the stress intensity factor range for cracks in the shovel boom. Detailed finite element models with a corner crack of various lengths were developed to determine the stress and strain conditions at the tip of corner cracks. The stress intensity factor range was calculated from the finite element analysis results using displacement, stress, and energy methods. All methods yielded similar results. For any given crack length, the crack growth rate was then predicted based on the calculated stress intensity factor and equation [51].

After the growth behaviour of the corner cracks with unequal lengths in the web and flange elements was understood, a simplified crack growth prediction method based on the assumption of cracks with equal length in the web and flange was proposed.

The fatigue prone region of the boom was divided into four zones, Zones A, B, C and D as shown in Figure 42, based on the magnitude of the equivalent stress range. In order to characterize each zone. a crack was located in the worst location within the zone in question. Therefore, cracks I, II, III, and IV were used to characterize zones A, B, C and D, respectively.

6.2 Use of Finite Element Method to Determine the Stress Intensity Factor

The use of equation [51] to establish the crack growth rate of fatigue cracks requires the knowledge of the stress intensity factor range, ΔK, which is a function of many factors, the main one being the geometry of the detail in which the crack is located and the loading applied on that detail. For the shovel boom, the fatigue detail consists of a weld between a diaphragm and the flange and web plates of a box girder. The stress intensity factor for a crack in that detail will have to account for the effect of stress concentration from the diaphragm and the fillet weld as well as the stress gradient in the web and possibly in the flange. Such a complex detail requires the use of a finite element procedure to determine accurately the magnitude of the stress intensity factor.

The most commonly used finite element procedures for the determination of the stress intensity factor involve modelling of the particular detail under investigation with a crack incorporated into the model. Once the numerical solution has been obtained for the finite element representation, crack tip intensity factor can be estimated by the use of established crack tip relations. Three possible methods can be used: displacement method, stress method, and energy method.

The displacement method is based on the relationship between the finite element nodal displacements the well-established crack tip displacement equations. For a plane stress condition, the displacement equation for mode I crack (crack opening mode), based on the displacement on the crack surface (for $\theta = \pi$ in Figure 43), is given as:

$$K_I = \frac{\sqrt{2\pi}E}{4}\frac{v_c}{\sqrt{r}} \qquad [53]$$

where K_I is the stress intensity factor estimated from the opening displacement v_c of a node close enough to the crack tip, r is the distance from the node to the crack tip. From a plot of K_I as a function of r, an estimate of K at the crack tip can be made by extrapolating the plot to $r = 0$.

The stress method is similar to the displacement method. The finite element nodal stresses are correlated to the crack tip stress solutions. If the stress perpendicular to the crack plane, σ_{yy}, on the $\theta = 0$ plane is used to calculate the stress intensity factor, the following well-known relationship is used:

$$K_I = \sigma_{yy}\sqrt{2\pi r} \qquad [54]$$

Once again, from a plot of K_I as a function of r, the stress intensity factor at the crack tip (r = 0) can be obtained by extrapolation.

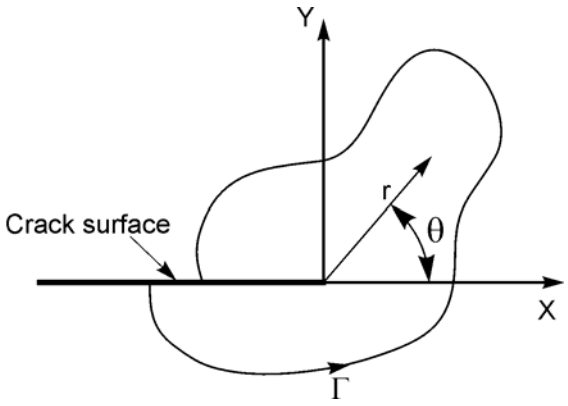

Figure 43 – Crack Tip Coordinates and Typical Contour Γ

The energy method makes use of the J-integral, which is a contour integral defined as:

$$J = \int_{\Gamma} (Wdy - T \cdot \frac{\delta u}{\delta x} ds) \qquad [55]$$

where Γ is an arbitrary contour surrounding the crack tip, as shown in Figure 43. The J-integral is proportional to the square of the crack tip stress intensity factor and for plane stress conditions the stress intensity factor can be calculated by

$$K_I = \sqrt{JE} \qquad [56]$$

6.3 Stress Intensity Factor Calculation for a Corner Crack in a Shovel Boom

The finite element mesh shown in Figure 19 was modified to incorporate a through-thickness corner crack at the location indicated as Crack I in Figure 42. The crack, located at the position indicated in Figure 44, was first incorporated in a relatively coarse mesh. In order to refine the mesh around the crack tip while keep the size of the model manageable, a sub-model, which includes a small portion of the flange, web, diaphragm and the corner crack, was meshed as shown in Figure 45. The sub-model technique implemented in the commercial software ABAQUS (HKS, 2003) was used to ensure that the boundary conditions imposed in the coarse mesh and loading effects were also presenting the sub-model. All steel plates of the boom were discretized using four-node shell elements, SR4, in the global model and eight-node shell elements, SR8, in the sub-model.

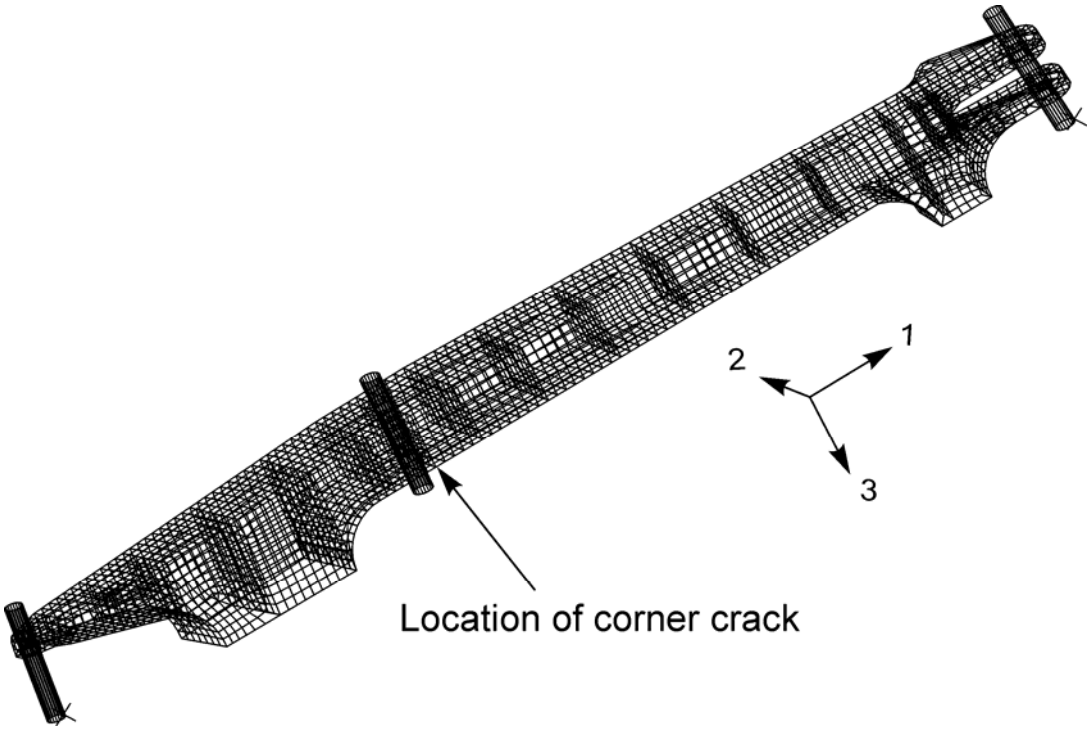

Figure 44 – Global finite element model of the boom

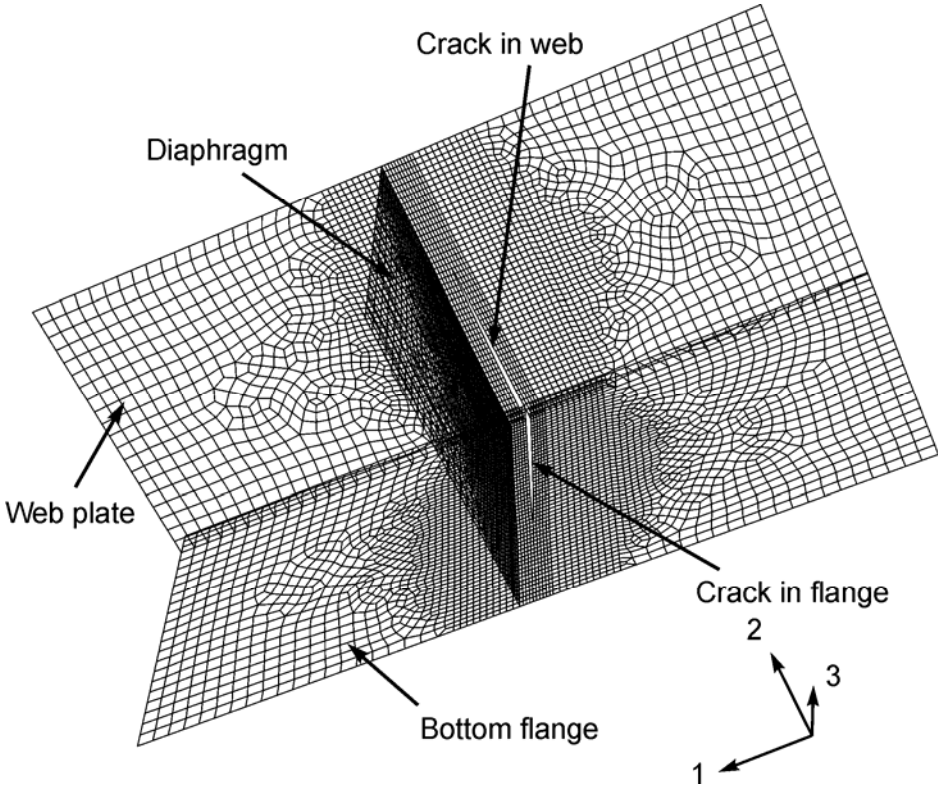

Figure 45 – Sub-model of the boom around a diaphragm

The finite element analysis results a crack extending 148.5 mm both into the web and into the flange are shown in Figure 46. The stress distribution from the global model and coarse mesh is shown in Figure 46(b) whereas the refined mesh sub-model is shown in figure Figure 46(a). The stress distribution and crack opening displacement obtained from the sub-model and global model are in good agreement, indicating that the correct loading and boundary conditions are pass on from the coarse to the fine mesh model.

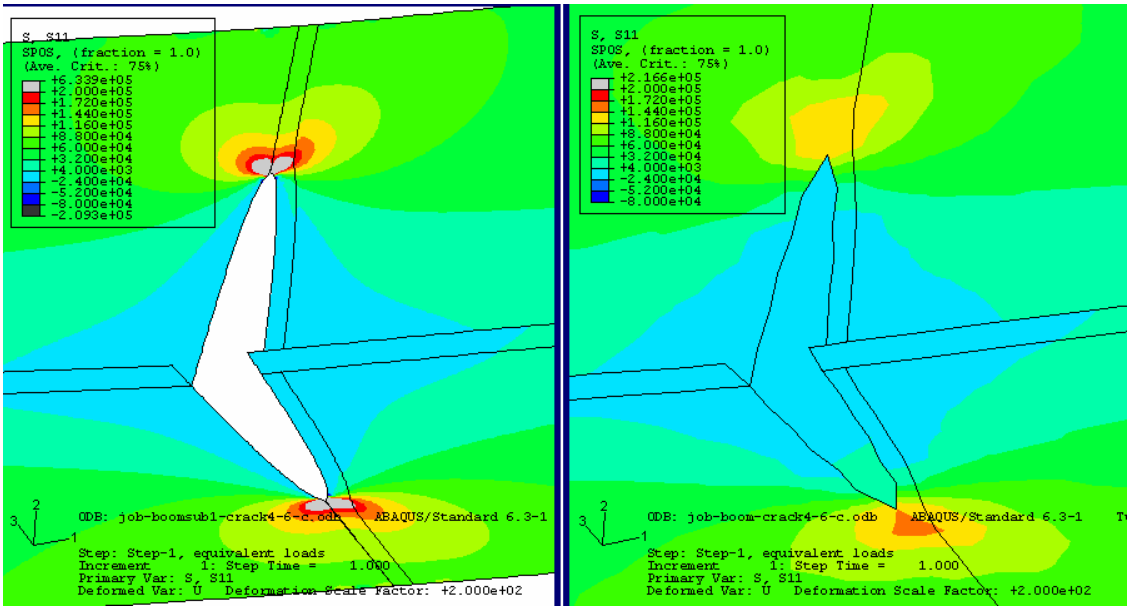

(a) Sub-model (b) Global model

Figure 46 – Longitudinal stress distribution for crack I (see Figure 42) (a=148.5mm)

The stress intensity factor for each crack tip was obtained using the three methods outlined above, namely, the displacement, the stress, and the J-integral methods. Node set 1, shown in Figure 47, consists of 10 nodes taken along the crack surface. The extrapolated crack tip opening displacement from these 10 nodes displacement was used with the displacement method to calculate the stress intensity factor. Node set 2 shown in Figure 47 also consists of 10 nodes and are located at the front of the crack. The stress intensity factor was calculated from the stresses at these 10 nodes. A regression line was then traced through the 10 points and extrapolated to the crack tip to obtain the stress intensity factor at the crack tip. The J-integral was calculated along three contours, namely, Γ_1, Γ_2 and Γ_3, shown in Figure 47. The average J-integral value from these three paths was used to determine the stress intensity factor from equation [56]. The results of the three methods agree well as shown in Figure 48 and Figure 49. For the following calculations, only the J-integral method was used since ABAQUS provides readily the value of the J-integral.

For the crack size illustrated in Figure 46, the stress intensity factors for the crack tip located in the flange is 42.9 MPa$\sqrt{m}$ and 40.9 MPa$\sqrt{m}$ for the crack tip located in the web. The stress intensity factor for the web crack tip is than that for the flange crack tip of same length because of the stress gradient present in the web.

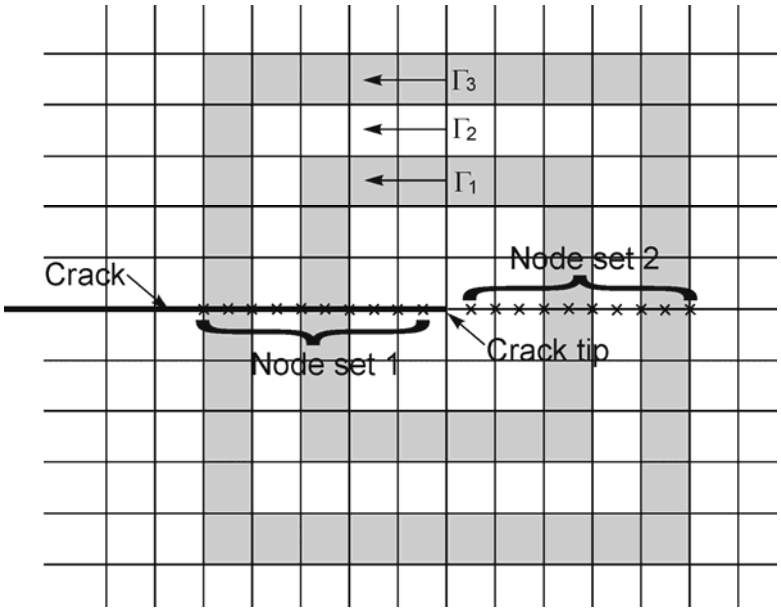

Figure 47 – Node sets and integral contours in sub-model

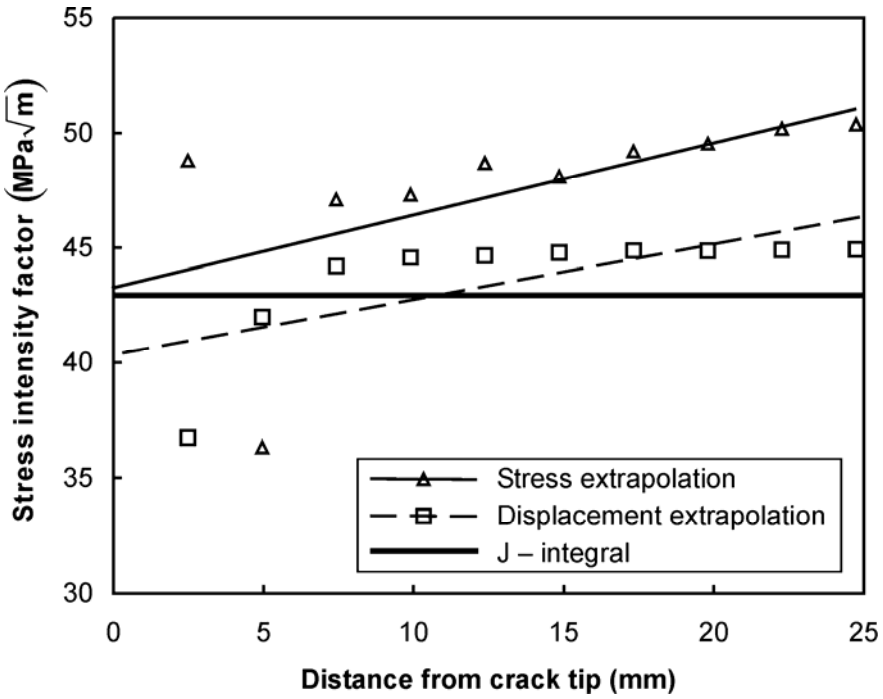

Figure 48 – Stress intensity factor estimation for crack tip in flange

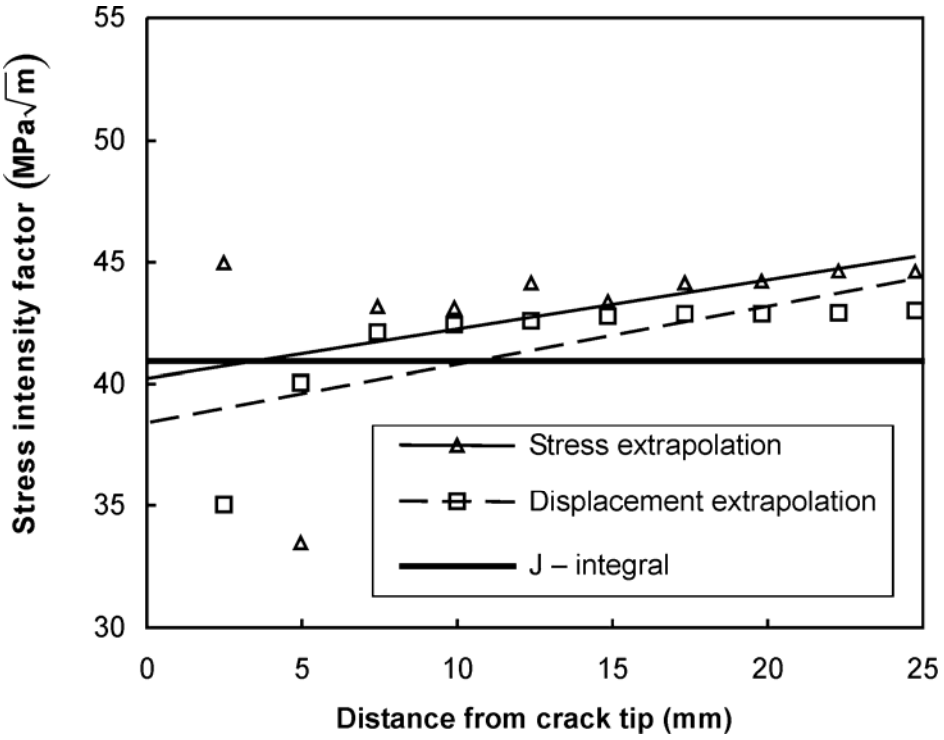

Figure 49 – Stress intensity factor estimation for crack tip in web

The stress intensity factor generally increases as the crack length increases, resulting in an increase in crack growth rate. It is therefore necessary to determine the relationship between the stress intensity factor and crack length in order to determine the remaining fatigue life. Corner cracks have two moving crack tips and the stress intensity factor for each crack tip is affected by the crack growth rate at the individual crack tips. Although there exist an infinite number of different flange and web crack length combinations, the finite element analysis was conducted for a limited number of cases covering a wide range of crack combinations. Five sets of flange crack length, a_f, to web crack length, a_w, ratios were investigated, namely, $a_f / a_w = 0$, 0.5, 1.0, 2.0, and ∞ for a corner crack at Crack I location shown in Figure 42. The stress intensity factor was obtained for crack lengths varying from 25 mm to 450 mm for each crack length ratio. The stress intensity factors for the flange crack tip and the web crack tip are shown in Figure 50 and Figure 51, respectively, and are summarized in Tables 3 to 7.

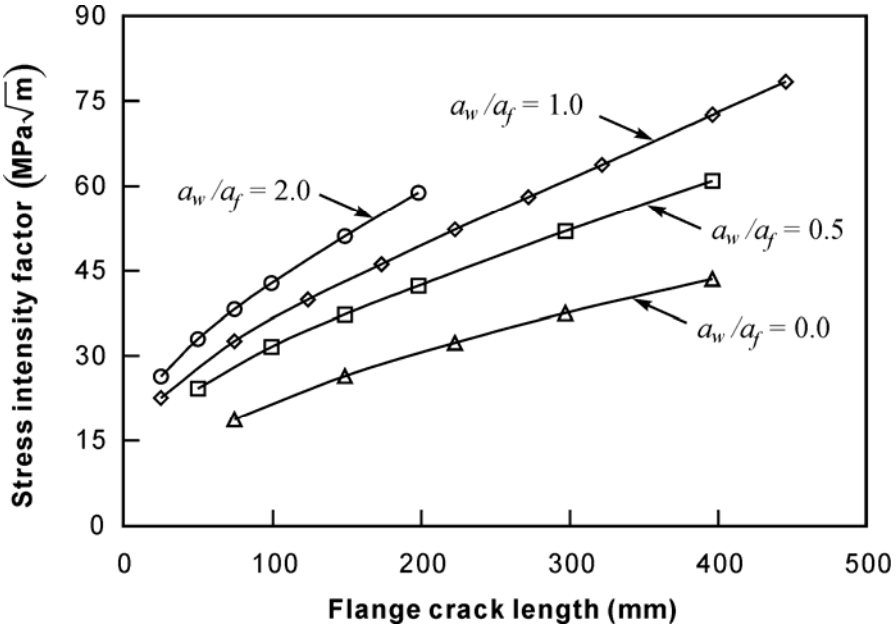

Figure 50 – Stress intensity factor variation for flange crack tip

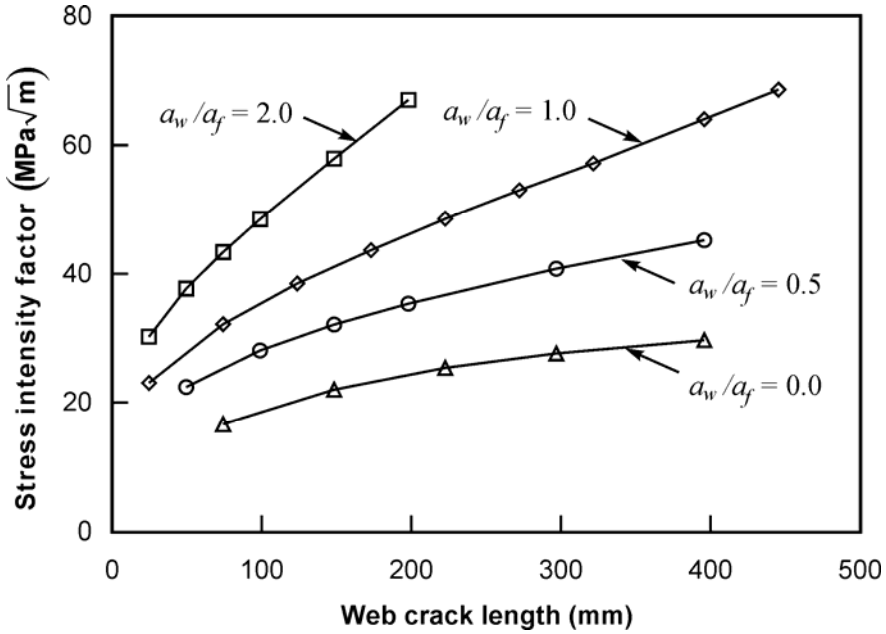

Figure 51 – Stress intensity factor variation for web crack tip

A least square regression analysis was used to fit curves through the data presented in Figure 50 and Figure 51. The resulting regression equations are as follows:

Stress intensity factor for the crack tip in the flange:

For $a_w/a_f = 0.0$

$$K_f = 2\times10^{-7} a_f{}^3 - 0.0002\, a_f{}^2 + 0.148\, a_f + 8.977 \quad [57]$$

For $a_w/a_f = 0.5$

$$K_f = 3\times10^{-7}\, a_f{}^3 - 0.0003\, a_f{}^2 + 0.1775\, a_f + 16.252 \quad [58]$$

For $a_w/a_f = 1.0$

$$K_f = 4\times10^{-7}\, a_f{}^3 - 0.0003\, a_f{}^2 + 0.2078\, a_f + 18.312 \quad [59]$$

For $a_w/a_f = 2.0$

$$K_f = 3\times10^{-6}\, a_f{}^3 - 0.0012\, a_f{}^2 + 0.3348\, a_f + 18.825 \quad [60]$$

Stress intensity factor for the crack tip in the web:

For $a_f/a_w = 0.0$

$$K_w = 3\times10^{-7}\, a_w{}^3 - 0.0003\, a_w{}^2 + 0.1263\, a_w + 8.7279 \quad [61]$$

For $a_f/a_w = 0.5$

$$K_w = 3\times10^{-7}\, a_w{}^3 - 0.0003\, a_w{}^2 + 0.1516\, a_w + 15.76 \quad [62]$$

For $a_f/a_w = 1.0$

$$K_w = 4\times10^{-7}\, a_w{}^3 - 0.0004\, a_w{}^2 + 0.1989\, a_w + 18.998 \quad [63]$$

For $a_f/a_w = 2.0$

$$K_w = 3\times10^{-6}\, a_w{}^3 - 0.0013\, a_w{}^2 + 0.3741\, a_w + 21.823 \quad [64]$$

where K_f and K_w are expressed in $\text{MPa}\sqrt{\text{m}}$ and a_f and a_w are expressed in mm.

Stress intensity factors for crack length ratios other than the ones presented above can be calculated either by interpolation or extrapolation. For example, the stress intensity factor for the crack tip in the flange with a_f = 100 mm and a_w = 80 mm can be determined by interpolating between a_f = 100 mm and a_w = 100 mm ($a_f/a_w = 1.0$) and crack with

a_f = 100 mm and a_w = 50 mm ($a_w/a_f = 0.5$), which can be obtained from Figure 50 and Equations [59] and [60] as follows :

For corner crack with $a_f = a_w$ =100 mm ($a_f/a_w = 1.0$), equation [59] gives

$$K_f = 36.5 \text{ MPa}\sqrt{\text{m}}$$

For corner crack with a_f = 100 mm and a_w = 50 mm ($a_w/a_f = 0.5$), equation [58] gives

$$K_f = 31.302 \text{ MPa}\sqrt{\text{m}}$$

It follows that, for a corner crack with a_f = 100 mm and a_w = 80 mm,

$$K_f = 31.302 + \frac{36.492 - 31.302}{100 - 50}(80 - 50) = 34.416 \text{ MPa}\sqrt{\text{m}}$$

Table 3 – Stress Intensity Factor for Crack I with $a_f/a_w = 0.0$

Crack I	a_f (mm)	a_w(mm)	K_f (MPa$\sqrt{\text{m}}$)	K_w(MPa$\sqrt{\text{m}}$)
I-3-web	0	74.25	N/A	16.6
I-6-web	0	148.5	N/A	22.0
I-9-web	0	222.75	N/A	25.4
I-12-web	0	297.0	N/A	27.6
I-16-web	0	396.0	N/A	29.7

Table 4 – Stress Intensity Factor for Crack I with $a_f/a_w = 0.5$

Crack I	a_f (mm)	a_w(mm)	K_f (MPa$\sqrt{\text{m}}$)	K_w(MPa$\sqrt{\text{m}}$)
I-2-ne2	24.75	49.5	26.3	22.4
I-4-ne2	49.5	99.0	33.0	28.1
I-6-ne2	74.25	148.5	38.2	32.1
I-8-ne2	99.0	198.0	42.8	35.3
I-12-ne2	148.5	297.0	51.1	40.8
I-16-ne2	198.0	396.0	58.9	45.2

Table 5 – Stress Intensity Factor for Crack I with $a_f / a_w = 1.0$

Crack I	a_f (mm)	a_w(mm)	K_f (MPa$\sqrt{m}$)	K_w(MPa$\sqrt{m}$)
I-2	49.5	49.5	28.2	28.2
I-3	74.25	74.25	32.6	32.2
I-4	99.0	99.0	36.4	35.5
I-5	123.75	123.75	39.9	38.5
I-6	148.5	148.5	43.1	41.2
I-7	173.25	173.25	46.2	43.7
I-8	198.0	198.0	49.0	45.9
I-9	222.75	222.75	52.3	48.5
I-10	247.5	247.5	55.2	50.8
I-11	272.25	272.25	58.1	53.0
I-12	297.0	297.0	61.0	55.1
I-13	321.75	321.75	63.8	57.2
I-16	396.0	396.0	72.6	64.0
I-18	445.5	445.5	78.4	68.6

Table 6 – Stress Intensity Factor for Crack I with $a_f / a_w = 2.0$

Crack I	a_f (mm)	a_w(mm)	K_f (MPa$\sqrt{m}$)	K_w(MPa$\sqrt{m}$)
I-2-ne1	49.5	24.75	24.3	30.2
I-4-ne1	99.0	49.5	31.6	37.7
I-6-ne1	148.5	74.25	37.3	43.3
I-8-ne1	198.0	99.0	42.3	48.5
I-12-ne1	197.0	148.5	52.0	57.9
I-16-ne1	396.0	198.0	61.0	67.0

Table 7 – Stress Intensity Factor for Crack I with $a_f / a_w = \infty$

Crack I	a_f (mm)	a_w(mm)	K_f (MPa$\sqrt{m}$)	K_w(MPa$\sqrt{m}$)
I-3-flange	74.25	0	18.7	N/A
I-6-flange	248.5	0	26.4	N/A
I-9-flange	222.75	0	32.3	N/A
I-12-flange	297.0	0	37.5	N/A
I-16-flange	396.0	0	43.5	N/A

6.4 Crack Growth Prediction For Corner Cracks at Crack I Position

Having defined the relationship between the stress intensity factor and crack length, the crack growth process of corner cracks can be predicted by integration of equation [48]. Because the stress intensity factor is a function of the web and the flange crack length, the integration process required to following the growth of a corner crack is complex. It is therefore preferable to simplify the procedure by making some simplifying assumptions in order to predict the crack growth process. One of the main assumptions is that, within a short integration increment, the stress intensity factor at each crack tip remains constant within the crack length increment. The general procedure adopted in this work to predict a corner fatigue crack behaviour is as follows:

For initial crack length a_f in the flange and a_w in the web,

Obtain the stress intensity factors K_f and K_w for the flange and the web crack tips based on a_f and a_w using Figure 50 and Figure 51 or equations [57] to [64].

Calculate crack growth rates for both flange and web crack tips, v_f and v_w using Paris Equation shown in Equation [48].

Let the faster crack tip, generally the flange tip located in the flange, grow by a small increment δ_o. The crack increment should be small enough to assure the precision of the integration procedure, which was set to be 0.3 mm. Update the crack lengths and the number of load cycles as follows:

$$a_f = a_f + \delta_o, \qquad a_w = a_w + \frac{v_w}{v_f}\delta_o \qquad [65]$$

$$N = N + \frac{\delta_0}{v_f} \qquad [66]$$

It should be noted that equations [65] and [66] are used when the crack tip in the flange of the box is the critical crack tip, i.e., the one with the maximum crack growth rate.

Repeat steps (1) to (3) until the increment of number of cycles δ_o / v_f is small for an increment of crack length, or until the stress intensity factor at one of the two crack tips reaches the fracture toughness of the material.

The crack growth curves generated using the procedure outlined above for a corner crack at the Crack I location shown in Figure 42 are presented in Figure 52. The figure presents flange and web crack growth curves for three different initial crack conditions as follows:

(a) a_f = 50 mm and a_w = 50 mm;

(b) a_f = 0 and a_w = 50 mm; and

(c) a_f = 50 mm and a_w = 0.

It should be noted that for the cracks a_f = 0 and a_w = 0 for conditions (b) and (c) although the crack has not propagated in the flange or web, it is assumed that the crack front is oriented perpendicular to the plate surface, i.e. the crack front is orientated so that the crack front does not change orientation. In a real situation, one of the crack tips from a crack that has formed in the flange would have to change orientation before propagating into the web. This re-orientation of the crack tip is neglected in the calculations presented in Figure 52. It is noted that the cracks grow slowly at the initial stage, but grows faster as the crack length and the stress intensity factor increase.

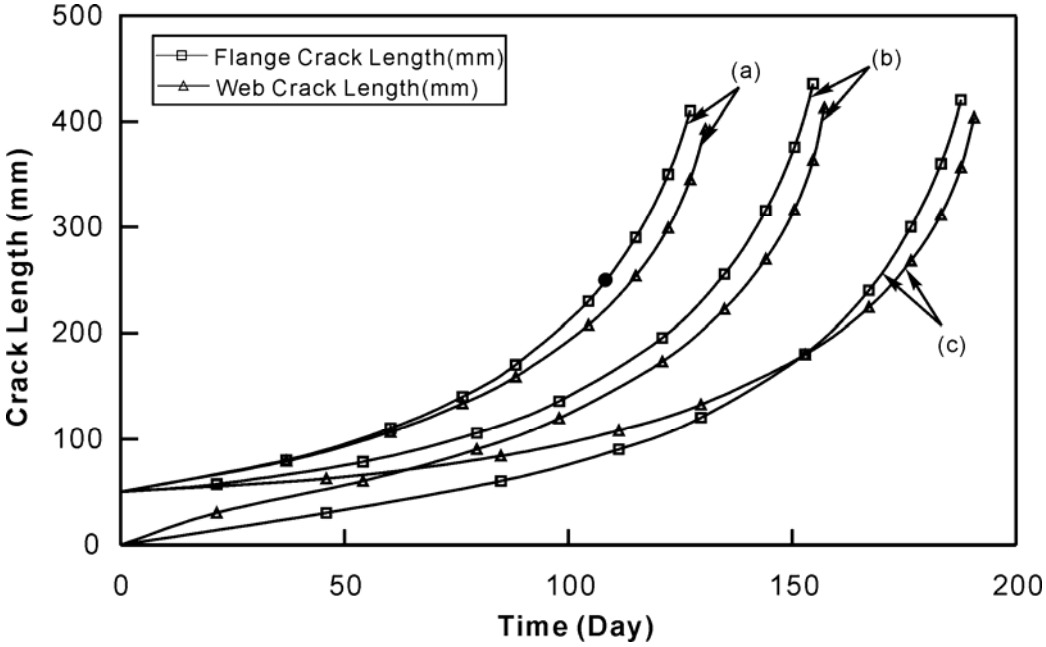

Figure 52 – Crack growth curves for corner crack at Crack-I position

6.5 Growth Behaviour of Corner Crack in Box Girder

The crack growth curves illustrated in Figure 52 show that no matter what the initial crack lengths are, the length difference between the flange crack and the web crack reaches some stable values. The shorter crack has the tendency to grow faster and catch up with the longer one after a period of time. The two lengths of the corner crack tend to balance at some stable compositions eventually.

Since the crack growth rates are governed by the stress intensity factors, this tendency of crack equalization can be explained by the way stress intensity factors vary while only one tip of a corner crack varies as the crack propagates. If the crack length in the web is set to 110mm, the stress intensity factor for both crack tips increases as the flange crack length increases as shown in Figure 53. When the flange crack length is shorter than 129 mm, the stress intensity factor of the flange crack tip is larger than that of the web crack tip, which results in a faster growth rate of the flange crack, allowing the flange crack to catch up with the web crack. On the other hand, when the flange crack length exceeds 129 mm the stress intensity factor of the flange crack tip is smaller than that of the web crack tip. The web crack will therefore grow faster to catch up with the flange crack. This behaviour is also observed if the flange crack length is set to, say 100 mm, in which case the balance value for the web crack length is 89 mm, as shown in Figure 54. It can therefore be concluded that for through-thickness corner cracks in a rectangular box girder, the shorter crack has the tendency to grow faster allowing to catch up with the longer crack and the crack lengths tend to reach a point where both crack tips move at the same rate.

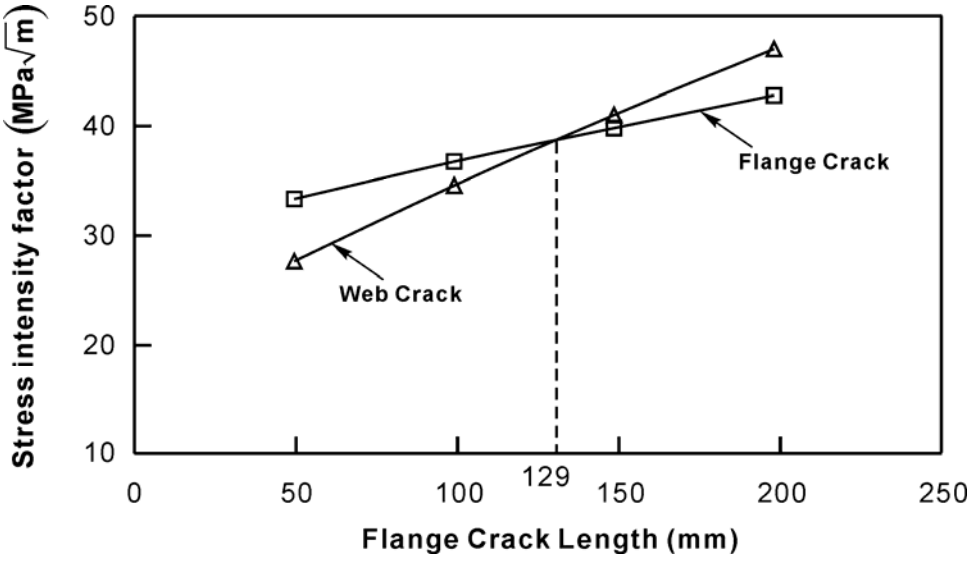

Figure 53 – Stress intensity factor variation with flange crack length (Web crack length=110mm)

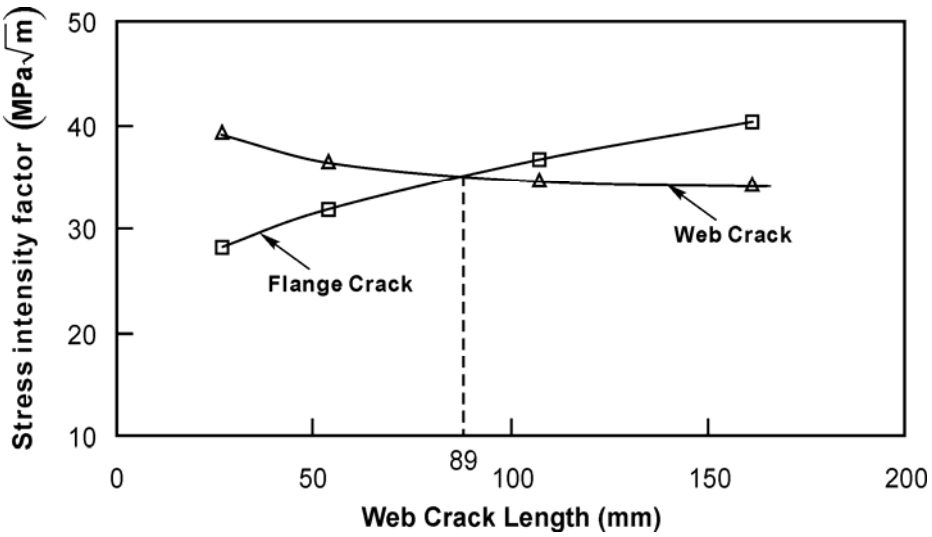

Figure 54 – Stress intensity factor variation with web crack length
(Flange crack length=100mm)

It is noted that, at the point where the stress intensity factor is the same for the web and flange crack tips, the portion of the crack in the web is a shorter than the portion of the crack in the flange. The difference is caused by the different stress distribution in the flange and the web plate. For equal crack length in the web an in the flange, the stress gradient in the web makes the stress intensity factor smaller for the crack embedded in the web than for the crack embedded in the flange. This length difference between the web and flange cracks is governed by the stress gradient and will increase with increasing crack length.

6.6 Simplified Method For Crack Growth Prediction

The above observations indicated that the crack front in the web and in the flange of a box section will tend to move at similar rates. When the corner crack is still relatively short (relative to the size of the boom cross-section), the stress gradient in the web is sufficiently small the stress intensity factor for the crack in the web is similar to the one for the crack in the flange. Consequently, the crack growth rate for both crack tips will be similar and the length of the crack extending in the web will be similar to that of the crack extending in the flange. For this reason, and also because of the complexity of dealing with unequal crack lengths in the flange and the web, a simplified approach was adopted whereby the crack length in the web was assumed to be always the same as the crack length in the flange. For corner cracks extending a different amount in the web and in the flange, the crack length for the corner crack was taken as the larger of the two crack extensions. This assumption always leads to conservative fatigue life predictions because the stress intensity factor for the longer crack will is always smaller for unequal cracks than for equal crack lengths. As illustrated in Figure 50 and in Figure 51, for equal crack lengths ($a_f/a_w = 1$), the stress intensity factor for the crack tip located in the flange is always greater than the stress intensity factor for the

crack tip located in the web. The stress intensity factor for the crack tip in the flange will therefore be used for fatigue crack growth predictions for a corner crack at the Crack I location in the boom (see Figure 42).

The crack growth is predicted by integrating the Paris equation, expressed by Equation [51]. Making the substitution for the constants *a* and *m*, the Paris equation can be re-written as:

$$dN = \frac{da}{2.89\times10^{-12}\left(\Delta K\right)^{3.59}} \qquad [67]$$

The number of load cycles, N_o, required to extend a fatigue crack from a_o to a_1 is obtained by integrating Equation [68]. This is expressed as:

$$N_0 = \int_{a_0}^{a_1} \frac{da}{2.89\times10^{-12}\left(\Delta K\right)^{3.59}} \qquad [68]$$

where ΔK is a function of the crack length *a*, obtained from Equation [59] where K_f is replaced by ΔK. A 7-point Gauss numerical integration procedure was used to obtain crack growth curves for a corner crack at the Crack I location with initial nominal crack length a_o = 50 mm. The crack growth curves for values of $\left(a_f - a_w\right)$ varying from –50 mm to 50 mm are presented in Figure 55. The crack length plotted on the vertical axis is the longer of the two crack segments, i.e. the flange crack for positive values of $\left(a_f - a_w\right)$ and the web crack for negative values. A comparison between crack growth curves for a positive and a negative value of $\left(a_f - a_w\right)$ indicates that cracks propagate more rapidly when the crack in the flange is longer than the crack in the web (i.e. positive values of $\left(a_f - a_w\right)$). For example, if we consider the time required to propagate a crack to 200 mm for a condition where $\left(a_f - a_w\right)$ is 30 mm, the crack size a_f would be 200 mm and a_w would be 170 mm. The time required to propagate the flange crack from 50 mm to 200 mm is expected to be 116 days of operation. During this same time the web crack would have propagated from 20 mm to 170 mm Now, if we consider the time required to propagate a crack to 200 mm for a condition where $\left(a_f - a_w\right)$ is -30 mm, the crack size a_f would be 170 mm and a_w would be 200 mm. The time required to propagate the crack in the web from an initial size of 50 mm to 200 mm is predicted to be 135 days. During this time the flange crack would have propagated from 20 mm to 170 mm.

Figure 55 also shows that the most conservative condition is obtained when the flange crack has the same length as web crack, i.e. $\left(a_f - a_w\right) = 0$. Figure 55 indicates that, for this corner crack configuration, the crack would take 98 days to propagate from 50 mm to 200 mm, representing a 15% shorter life than the corner crack configuration with $\left(a_f - a_w\right) = 30$ mm.

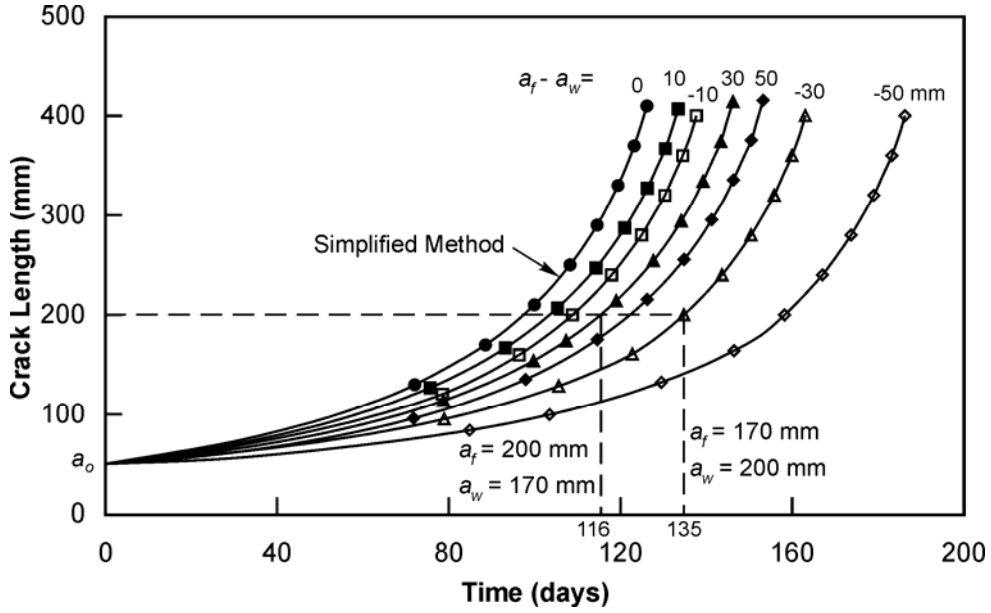

Figure 55 – Crack growth curves for Crack I with different crack length differences

Assuming equal length flange and web cracks, the stress intensity factor variation with the nominal crack length for Crack II, Crack III and Crack IV were determined with the method described above. The results are summarized in Table 8 and illustrated in Figure 56. The relationships between stress intensity factors and crack length, a, were obtained by a least square regression analysis for Crack II, Crack III and Crack IV as follows:

$$K_{fII} = 3\times10^{-7}\,a^3 - 0.0002\,a^2 + 0.1848\,a + 17.893 \quad [69]$$

$$K_{fIII} = 2\times10^{-7}\,a^3 - 0.0002\,a^2 + 0.169\,a + 16.642 \quad [70]$$

$$K_{fIV} = 2\times10^{-7}\,a^3 - 0.0002\,a^2 + 0.1458\,a + 14.077 \quad [71]$$

Table 8 – Stress Intensity Factor for Different Crack Locations and Crack Lenghs

Crack length, a (mm)	K_f (MPa$\sqrt{\text{m}}$)		
	Crack II	Crack III	Crack IV
49.5	26.5	24.5	20.8
99.0	34.5	32.1	27.3
198.0	47.4	44.5	37.6
197.0	59.7	56.7	47.6
396.0	71.5	68.9	57.5
445.5	78.0	75.4	62.9

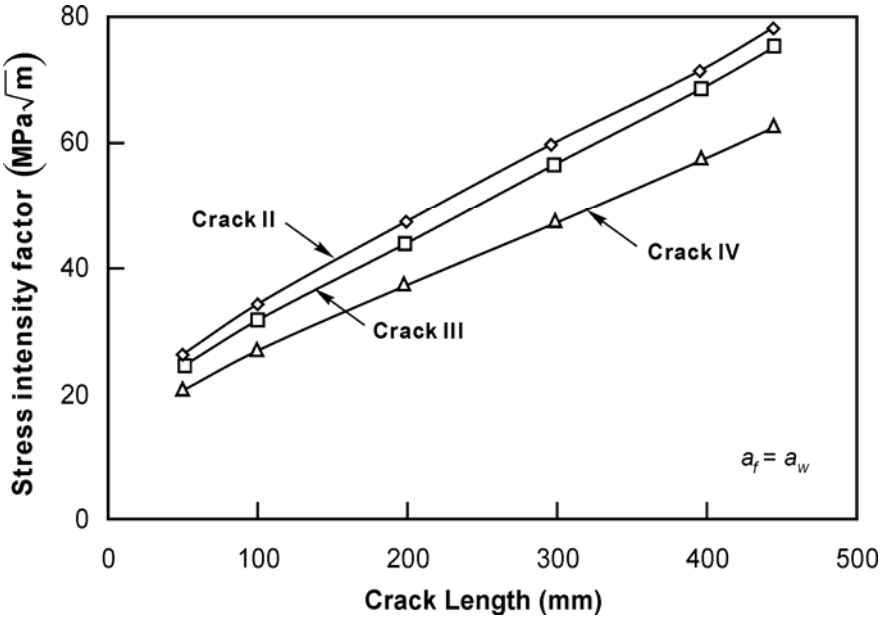

Figure 56 – Stress intensity factor variation for Crack II, Crack III and Crack IV

The crack growth curves for corner cracks at locations I, II, III, and IV identified in Figure 42 the Crack I, II, II and IV with initial crack length $a_0 = 0$ were obtained using Equation [68] and are compared in Figure 57. As expected, the cracks located in the regions of the boom exhibiting high equivalent stress ranges grow faster than the cracks located in zone of low equivalent stress range.

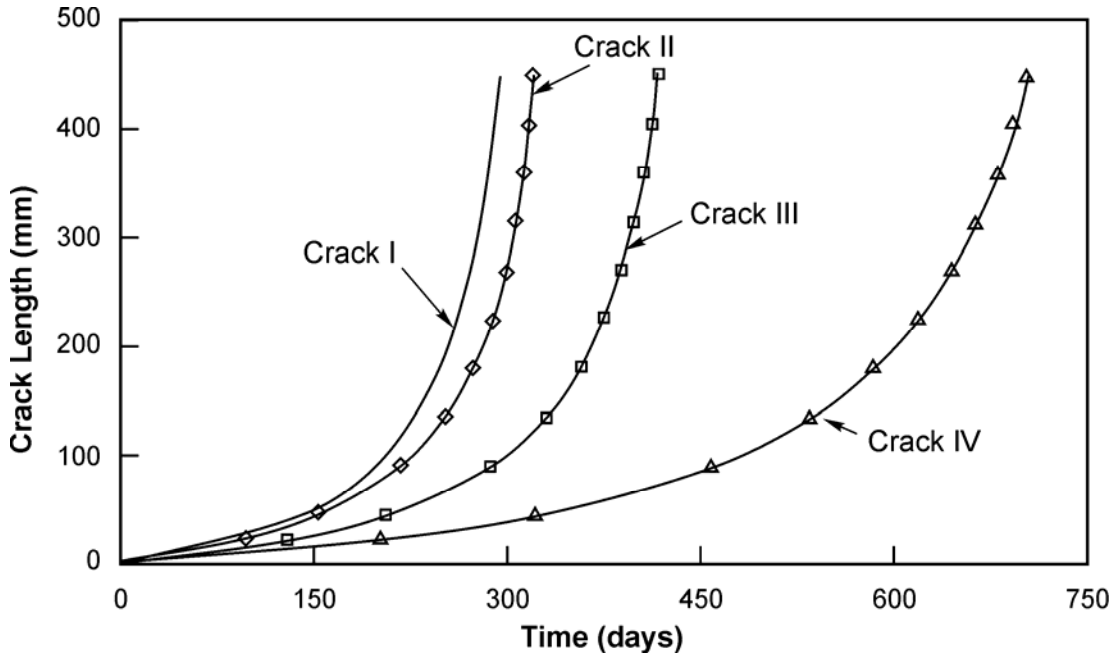

Figure 57 – Crack Growth Curves for Crack I, II, III and IV

7. Remaining Safe Operating Life Prediction of the Shovel Boom

In order to predict the remaining safe operating life of a shovel boom with a corner crack of known size, the critical crack length must be determined based on three limit states. The first limit states consists of the plastic collapse of the remaining ligament, i.e. yielding of the cracked section of the boom. As the stresses on the cracked section grow with crack size, the stress intensity factor at the crack tips increases. Brittle fracture occurs when the stress intensity factor reaches a critical value; the fracture toughness. The fracture toughness properties of CSA-G40.21-350WT steel was determined from a 38 mm plate. The measured fracture toughness was reported in section 5.2. The third limit state consists of rapid crack growth. A limiting crack growth rate of 4.0 mm/day was selected for the following work.

The critical length for corner cracks at Crack I location (see Figure 42) was calculated to be a_c = 204 mm based on the crack growth rate limit of 4.0 mm/day. The maximum value of the nominal stress and corresponding stress intensity factor, σ_{max} and K_{max}, were calculated for a_c = 204 mm under the self weight of the boom and its accessories (σ_o and K_o) and the maximum boom force measured during the 48 hours of monitored field operation (σ_1 and K_1). Cracked finite element models as shown in Figure 44 and Figure 45 and the technique outlined in section 6 were used for the analysis. The results are summarized in Table 9. The maximum stress in the boom, calculated from the applied axial force and bending moment on the net area of the cracked section, was found to be 171 MPa. This is much lower than the minimum specified yield strength of 350 MPa for this grade of steel. Yielding of the net section is therefore not expected to be a governing factor. Table 9 also shows that the maximum stress intensity factor ($81.7\ \text{MPa}\sqrt{\text{m}}$) is lower than the low temperature fracture toughness value of the material ($92.8\ \text{MPa}\sqrt{\text{m}}$), indicating that the crack growth is stable and the boom will not fail by brittle fracture. It is recalled that the fracture toughness was determined at –50 °C, which represents winter temperature condition. It is therefore concluded that the critical crack size is not controlled by brittle fracture either under summer operating conditions or winter operating conditions. It should be noted, however, that this conclusion is based on the field data collected for two days during August 2002. It is possible that the maximum stress in the boom would be higher under winter operating conditions. If this is the case, brittle fracture could still be a governing limit state under winter operating conditions. This issue can only be resolved with more field data to assess operating conditions during winter.

For a critical crack size of 204 mm and the crack growth curve presented in the previous section for a corner crack in the Crack I zone shown in Figure 42, the remaining fatigue life for different starting crack sizes can be predicted. Figure 58 presents the crack growth curve and the remaining fatigue life curve for a crack size varying from zero to 204 mm. The remaining life for this range of crack size ranges from about 250 days to no significant remaining life when the initial crack size becomes equal to the critical value. For example,

the remaining fatigue life of a boom with a corner crack within the Crack I zone of size a_o = 70 mm is expected to be about 72 days as shown in the figure.

Table 9 – Nominal and maximum stress intensity factors for Crack I with critical length

Nominal stress	σ_0 (MPa)	σ_1 (MPa)	σ_{max} (MPa)	F_y (MPa)
Crack I (a = 204 mm)	12	159	171	350
Stress intensity factor	K_0 ($MPa\sqrt{m}$)	K_1 ($MPa\sqrt{m}$)	K_{max} ($MPa\sqrt{m}$)	K_c ($MPa\sqrt{m}$)
Crack I (a = 204 mm)	7.8	73.9	81.7	92.8

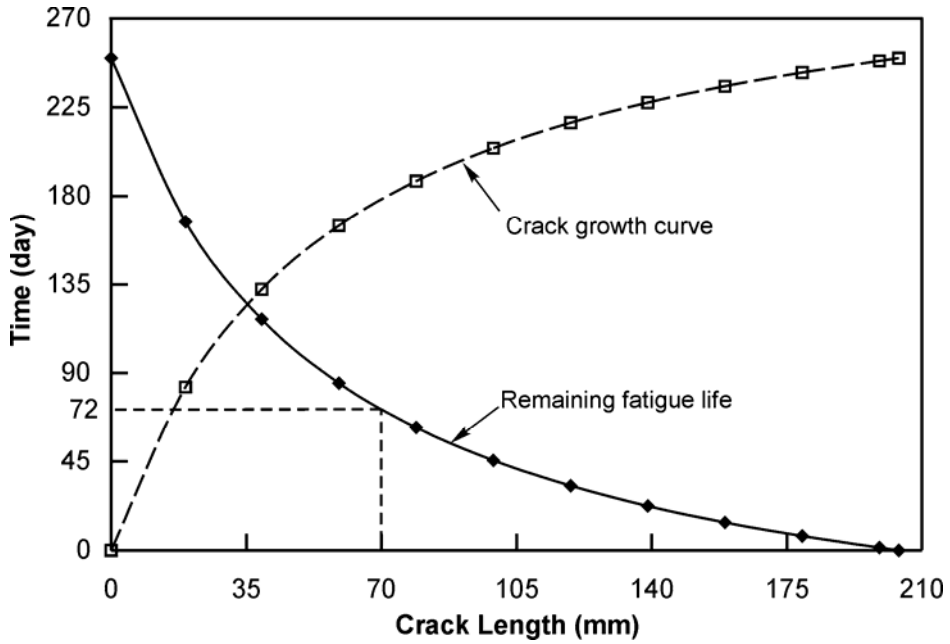

Figure 58 – Remaining fatigue life prediction for Crack I

The above presentation of remaining life for Crack I location was based on a limiting crack growth rate of 4 mm/day, which was arbitrarily chosen. If this limit is removed, one can calculate the remaining life based either on crack fracture, yielding of remaining ligament as failure criteria. Using these limitations rather than the 4 mm/day criterion used above, the remaining life for cracks of lengths varying from 50 mm to 450 mm can be obtained directly from Figure 57 for all four zones of the boom identified in Figure 42. The tabulated values of remaining life are presented in Table 10.

Table 10 – Remaining Life of BE Shovel Boom (Days)

Crack Length	Crack Location			
(mm)	Crack I	Crack II	Crack III	Crack IV
50	142	157	196	357
75	110	119	149	278
100	89	92	115	220
125	73	74	92	179
150	61	59	74	149
175	50	47	61	123
200	40	38	51	103
225	34	31	42	86
250	28	24	34	69
275	23	19	28	57
300	18	15	22	46
325	14	11	16	34
350	11	8	10	25
375	8	5	7	17
400	6	2	4	9
425	3	1	2	4
450	0	0	0	0

In order to reduce the level of conservatism resulting from the relative crack length assumption made earlier, the fatigue life predicted based on this simplifying assumption can be adjusted by comparing the fatigue life of a corner crack with $(a_f - a_w) = 0$ with that of corner cracks with different values of $(a_f - a_w)$. The extended fatigue life resulting from values of $(a_f - a_w)$ from 100 to -100 for a corner crack of initial length a_o = 100 mm was determined as shown in Figure 59 and Figure 60. The crack length a_o is the longer of the flange or web crack The results of the calculations summarized in Figure 59 and Figure 60 were obtained for Crack I location in the BE shovel boom.

The difference between the fatigue life for equal length cracks and unequal length cracks can be obtained directly from Figure 59 and Figure 60. These values, along with values for other initial crack size a_o , are tabulated in Table 11 for different values of crack length differences ($a_f - a_w$). It can be seen that the fatigue life extension is related to both initial crack length and crack length difference of the corner cracks. A larger crack length

difference causes larger fatigue life extension, indicating the conservatism of the equal crack length assumption.

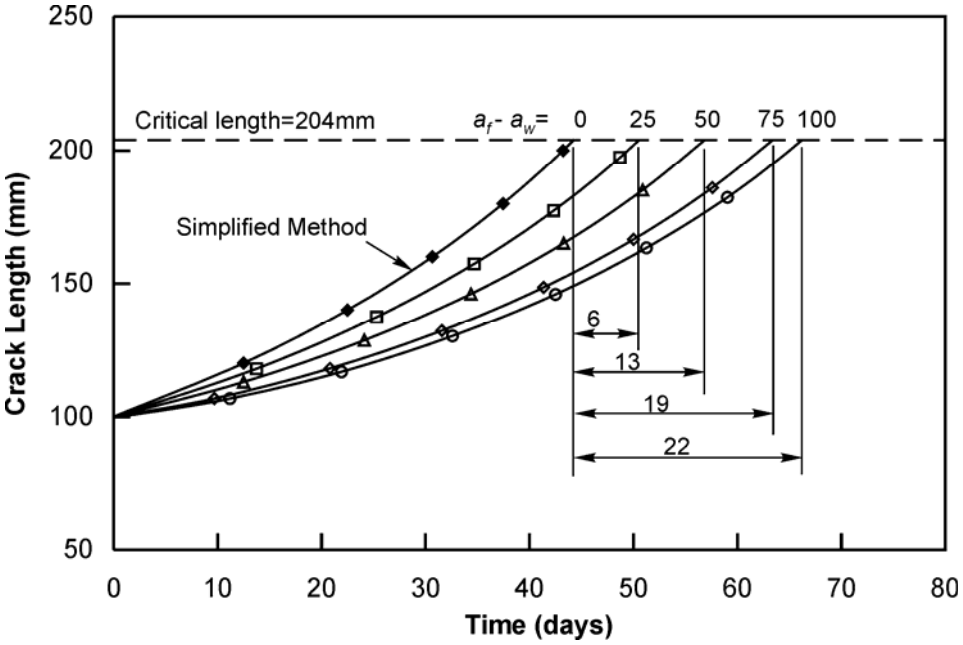

Figure 59 – Fatigue life extension for Crack I (a_o = 100 mm, $a_f - a_w > 0$)

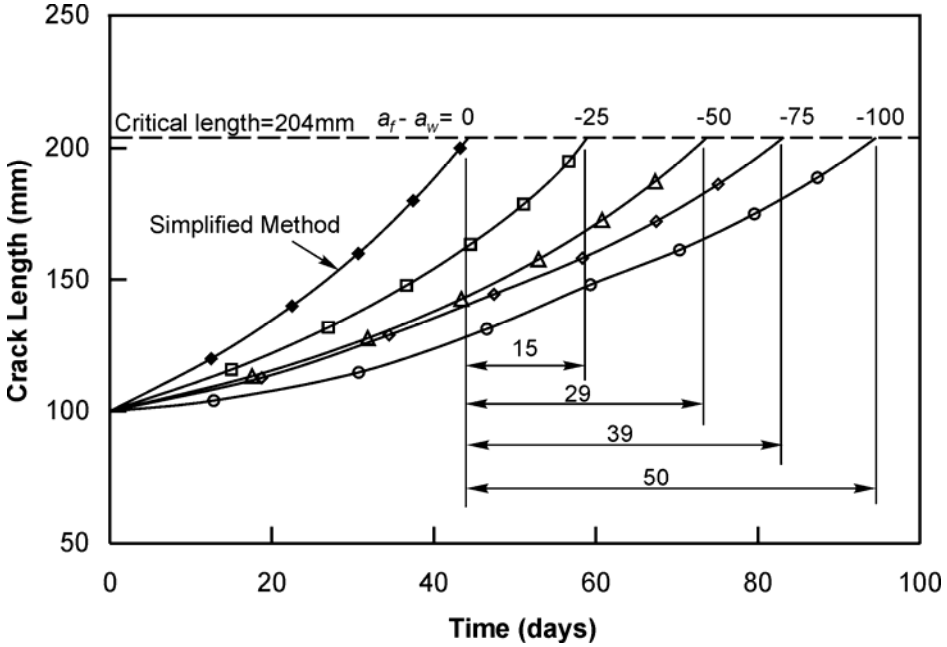

Figure 60 – Fatigue life extension for Crack I (a_o = 100 mm, $a_f - a_w < 0$)

According to Table 11, for the above corner crack with nominal crack length 70mm, if the flange and web crack lengths are a_f = 70 mm and a_w = 10 mm, respectively, the additional fatigue life extension should be 19 days and the total remaining fatigue life is 91 days. If

exchanging the flange and web crack length, the fatigue life extension turns to be 41 days and the total fatigue life 113 days, which is much longer than the former one.

Table 11 – Increase in Fatigue Life for Unequal Length Cracks (days) for Crack I

		$a_f - a_w$ (mm)								
		-125	-100	-75	-50	-25	0	25	50	100
a_o (mm)	50	—	—	—	61	31	0	15	25	—
	75	—	—	59	41	20	0	9	19	—
	100	—	50	39	29	15	0	6	13	22
	125	37	30	25	20	12	0	—	8	17

8. Crack Clock Chart Construction

Table 10 and Table 11 can be used to predict the remaining life of corner cracks in the BE shovel boom. The data in these tables can be further interpolated and extrapolated so that they are set in a useful format for use by field inspectors and engineers. This section explains the procedure adopted to fit a surface to the data presented in Table 10 and Table 11 and construct field charts for crack life predictions.

The data in Table 11 can be added to those in Table 10 to form 40 points of FEA-based life predictions as shown in Table 12. Although Table 11 was derived for Zone I cracks only, it is conservative for Zones II, III and IV. The error associated with this approximation will be considered later on in choosing the factor of safety associated with each zone chart.

For each zone, the 40 data points can be used to fit a surface that describes the remaining life of a corner crack at different lengths of flange and web cracks. TABLE CURVE 3D ® software was used to construct four surfaces to fit the data points presented in Table 12. The four fitted curves as well as their residual plot are shown in Figures 61, 62, 63 and 64 for zones I, II, III and IV, respectively.

The fitted surfaces show that crack life decreases as crack length increases. This reduction is more pronounced for growing flange cracks than for web cracks. The accuracy of these fitted surfaces in predicting the actual remaining life of corner cracks will be discussed later.

The fitted surfaces in Figures 61 to 64 can be utilized to construct an easy-to-use charts which relate predicted remaining life of inspected corner crack to its two lengths; flange crack length and web crack length. These charts are represented in Tables 13, 14, 15 and 16 for corner cracks in zones I, II, III and IV, respectively. For simplicity, Tables 13 to 16 will be referred to as “Crack Clock” charts.

Table 12 – FEA-based Crack life for different corner crack lengths

Crack size (mm)		Remaining Life (days)			
Flange	Web	Zone 1	Zone 2	Zone 3	Zone 4
50	50	142	157	196	357
75	75	110	119	149	278
100	100	89	92	115	220
125	125	73	74	92	179
150	150	61	59	74	149
175	175	50	47	61	123
200	200	40	38	51	103
225	225	34	31	42	86
250	250	28	24	34	69
275	275	23	19	28	57
300	300	18	15	22	46
325	325	14	11	16	34
350	350	11	8	10	25
375	375	8	5	7	17
400	400	6	2	4	9
425	425	3	1	2	4
450	450	0	0	0	0
0	50	203	218	257	418
0	75	169	178	208	337
0	100	139	142	165	270
0	125	110	111	129	216
25	50	173	188	227	388
25	75	151	160	190	319
25	100	128	131	154	259
25	125	103	104	122	209
50	0	167	182	221	382
50	25	157	172	211	372
50	75	130	139	169	298
50	100	118	121	144	249
50	125	98	99	117	204
75	25	129	138	168	297
75	50	119	128	158	287
75	100	104	107	130	235
75	125	93	94	112	199
100	0	111	114	137	242
100	50	102	105	128	233
100	75	95	98	121	226
100	125	85	86	104	191
125	25	90	91	109	196
125	75	81	82	100	187

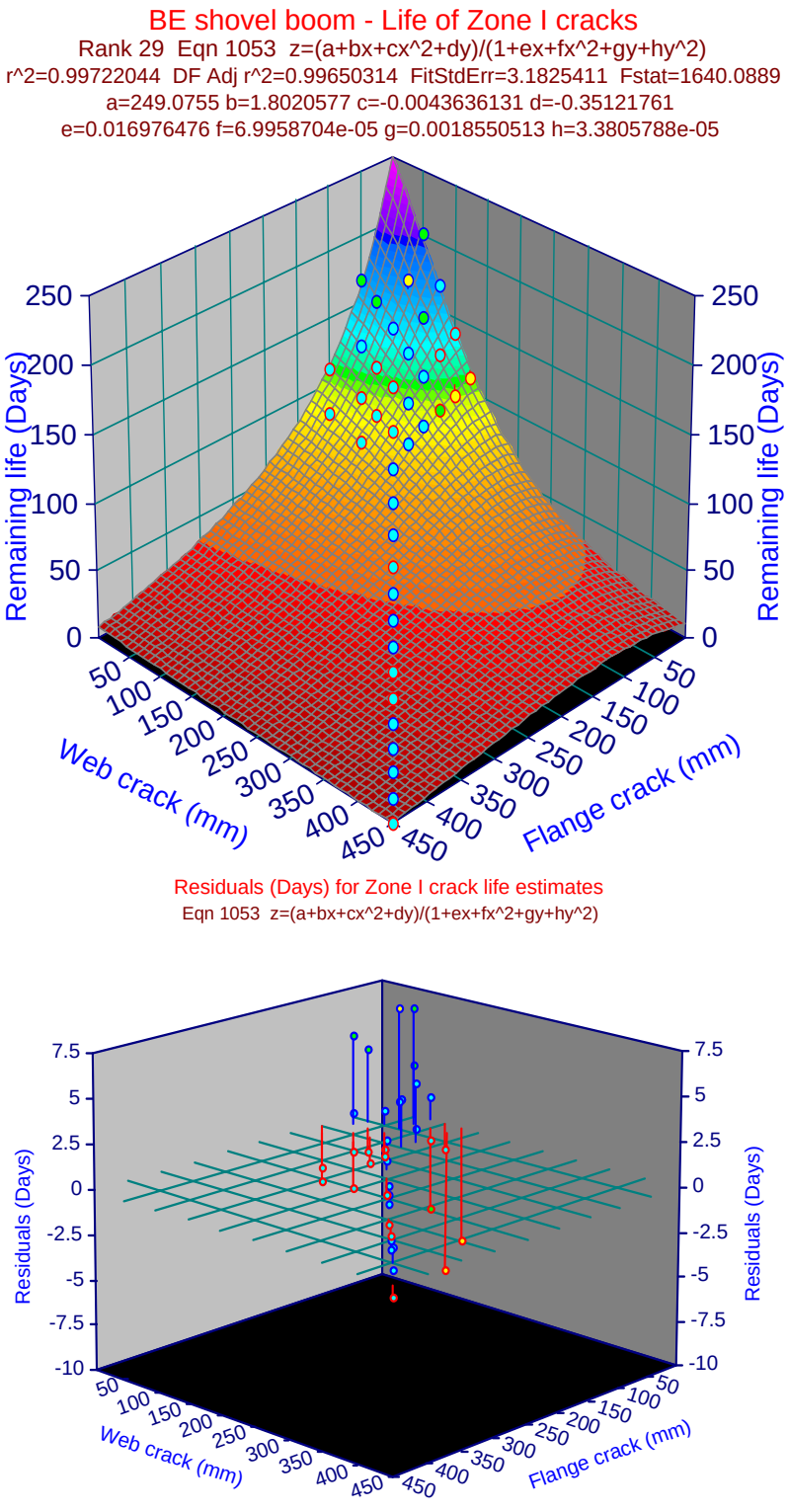

Figure 61 – Zone 1 Crack Life Surface

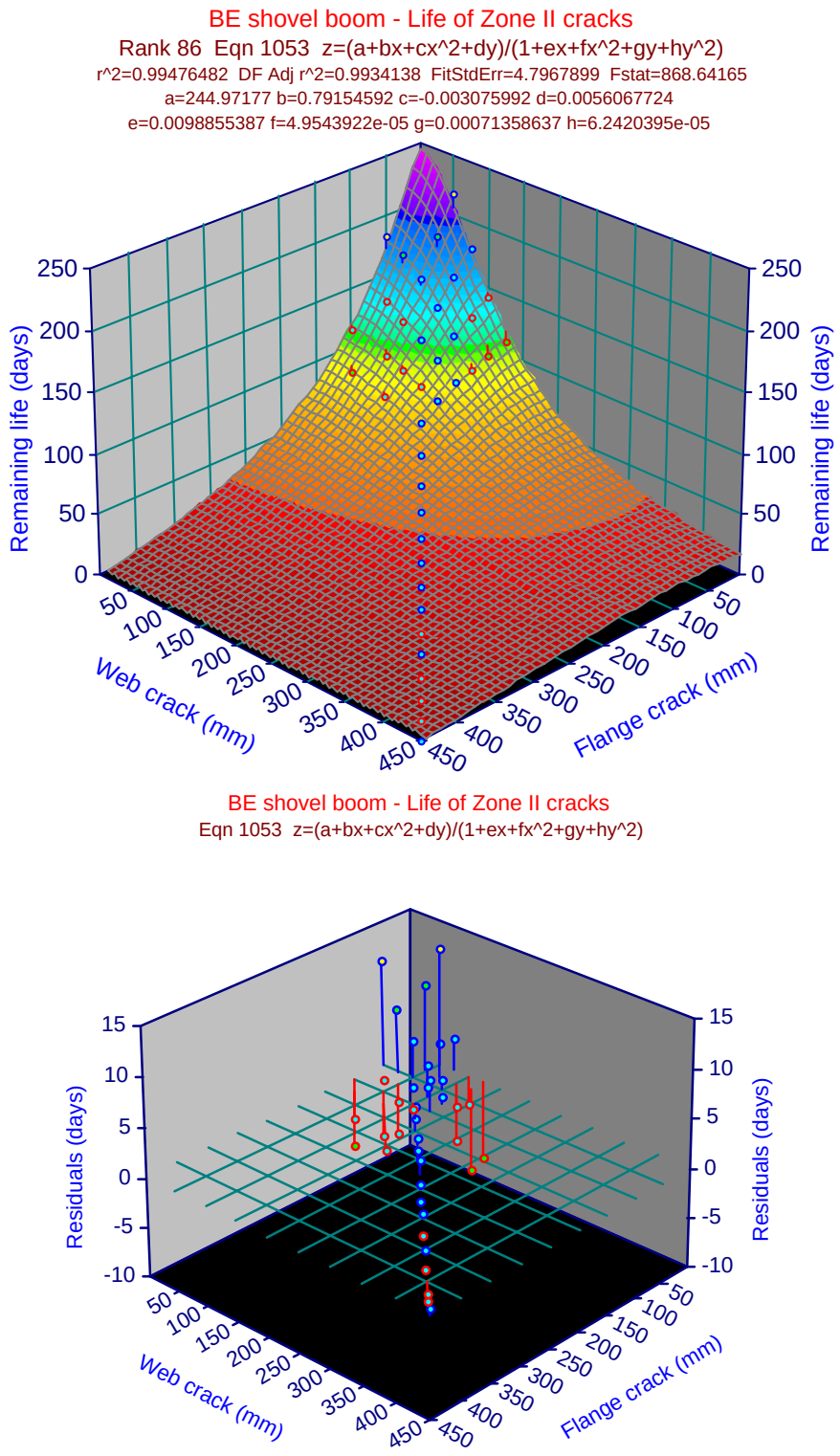

Figure 62 – Zone II crack life surface

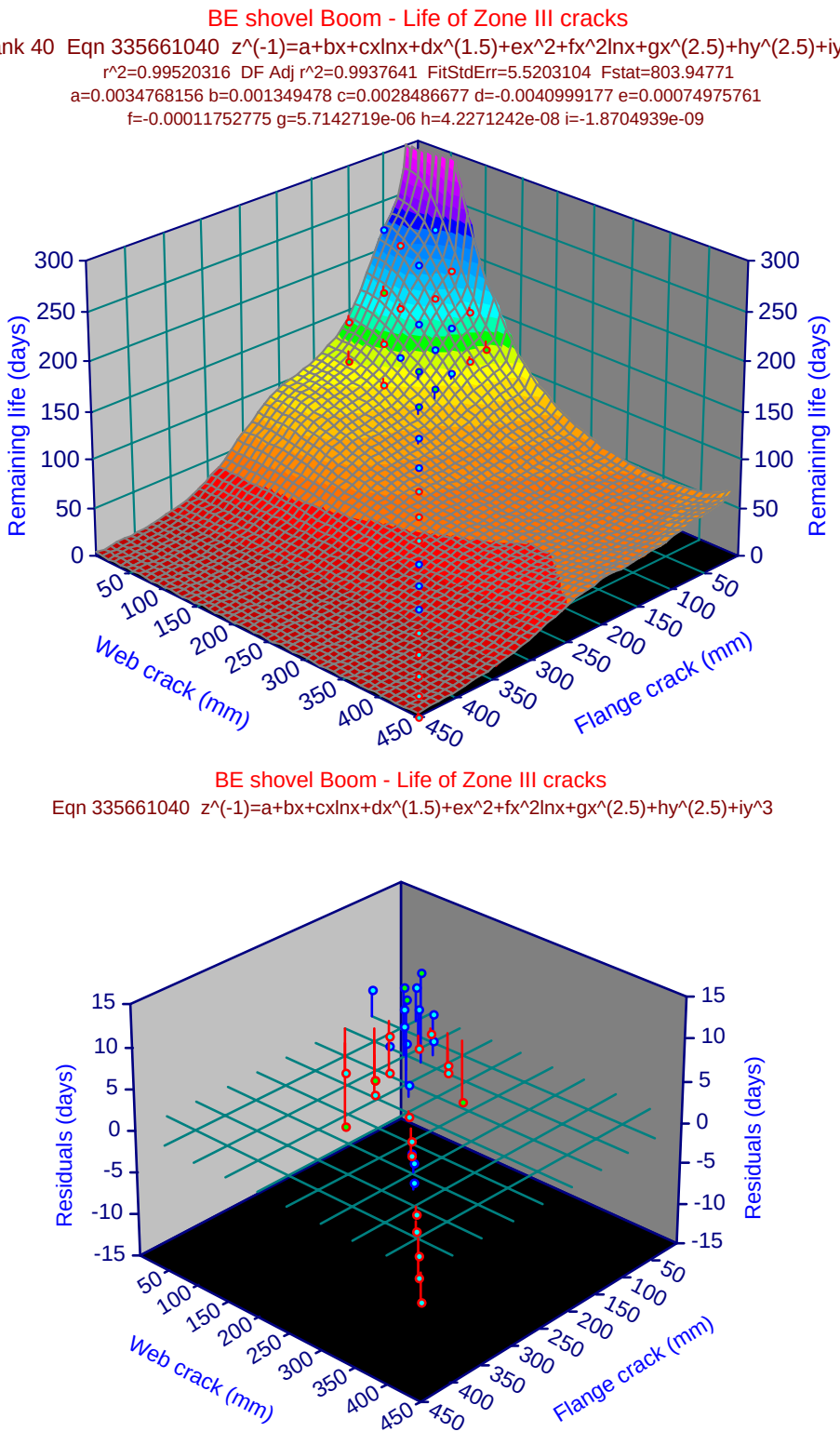

Figure 63 – Zone III crack life surface

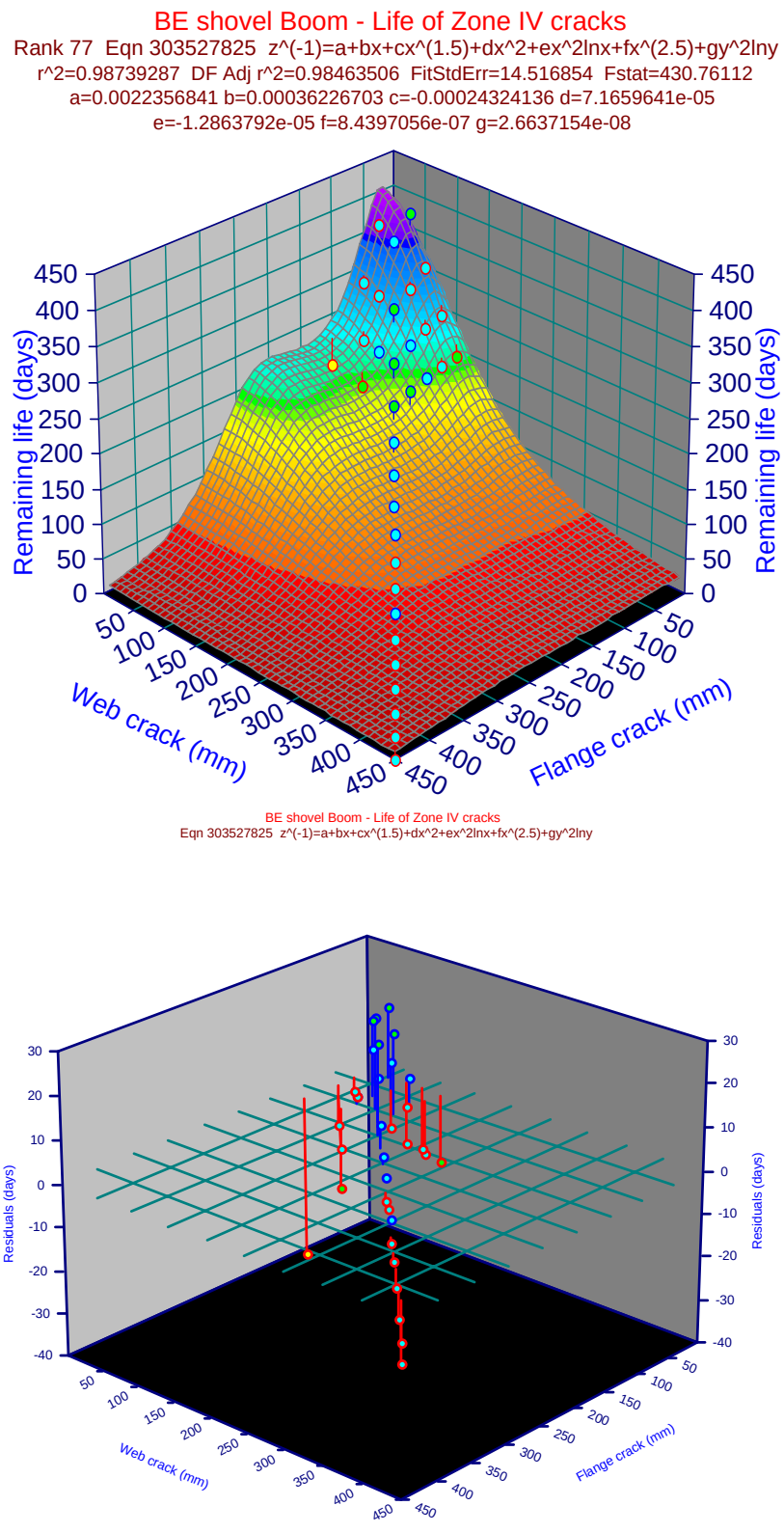

Figure 64 – Zone IV crack life surface

Table 13 – Crack Clock for Zone I

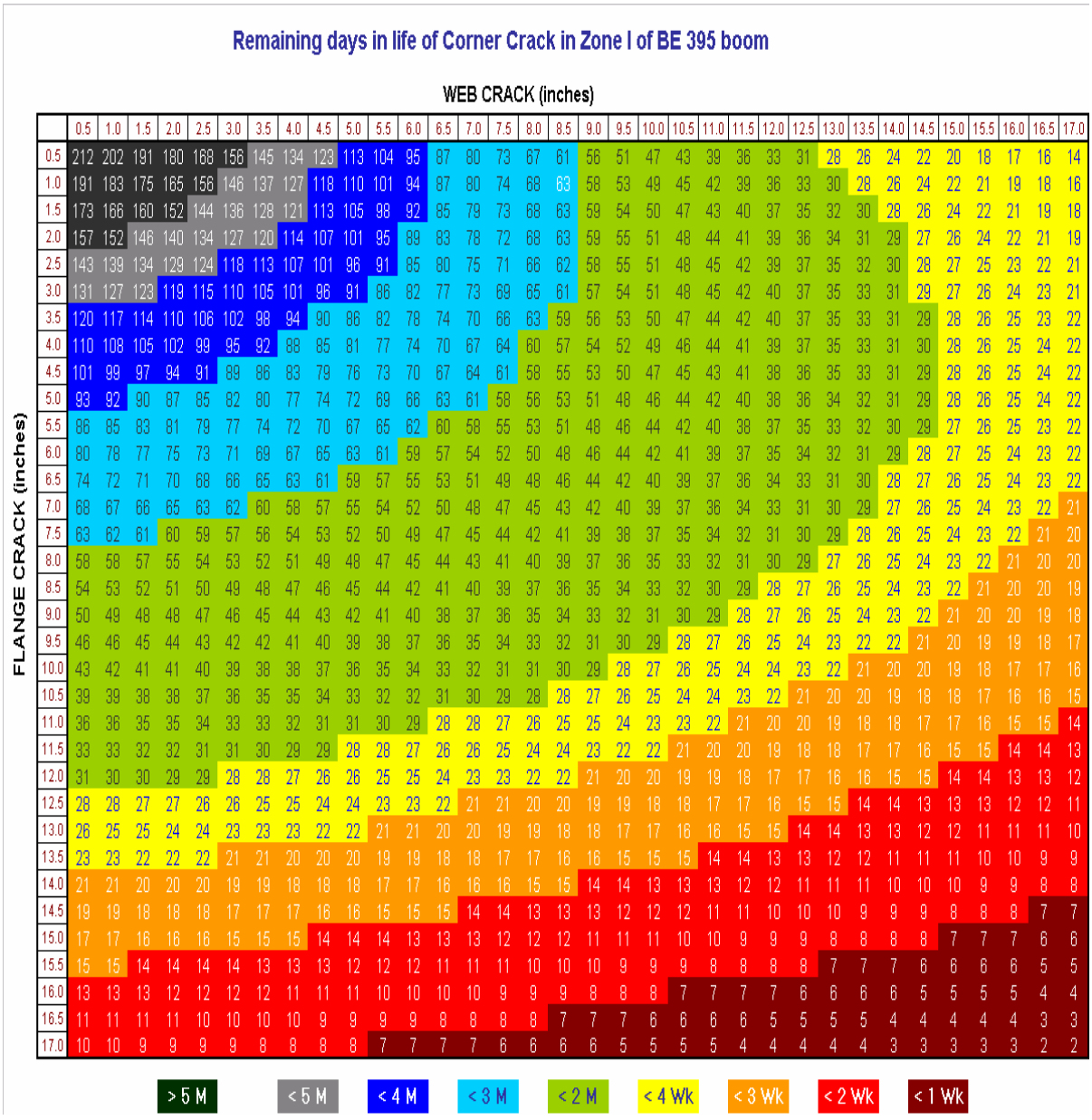

Table 14 – Crack Clock for Zone II

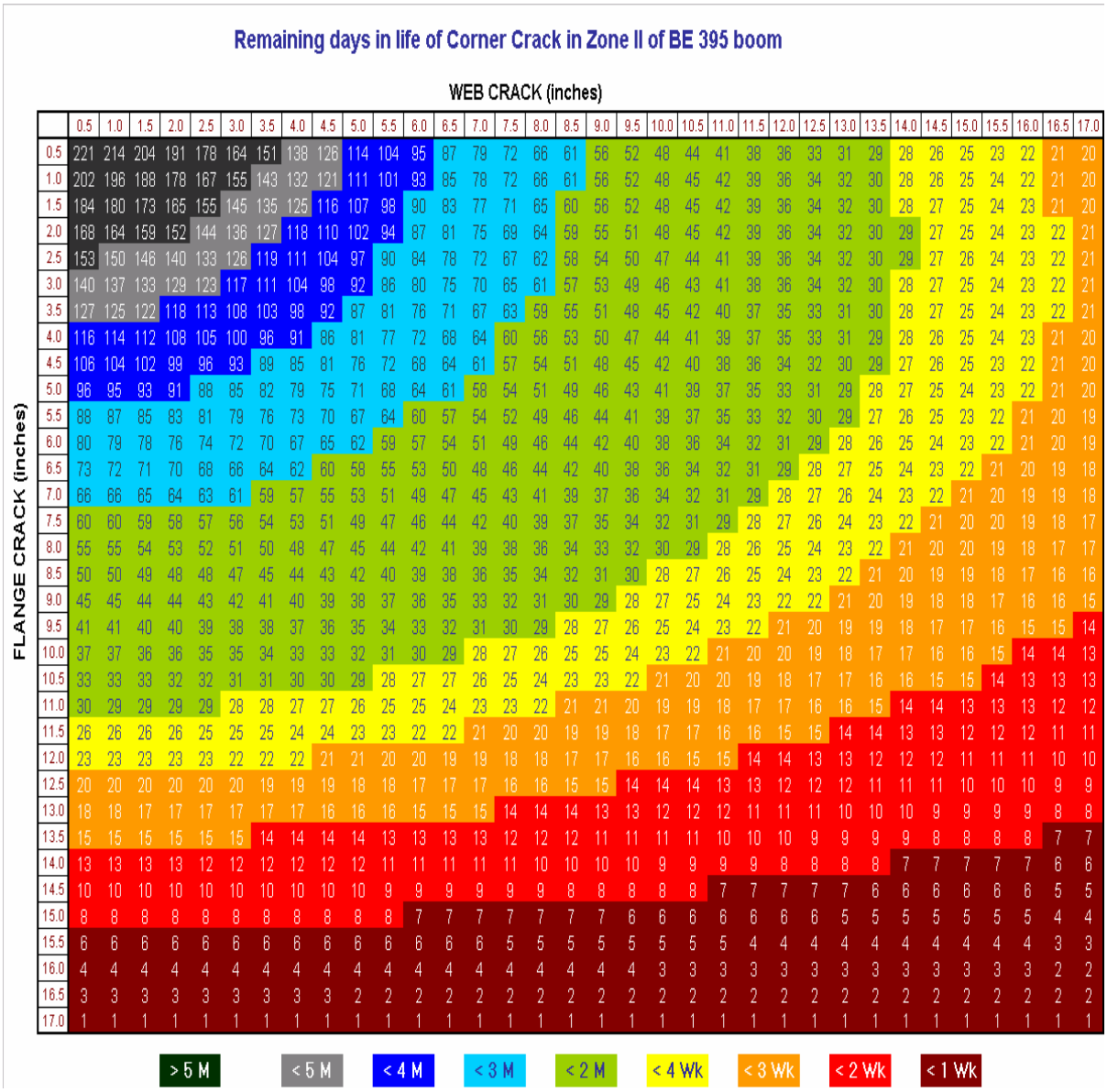

Table 15 – Crack Clock for Zone III

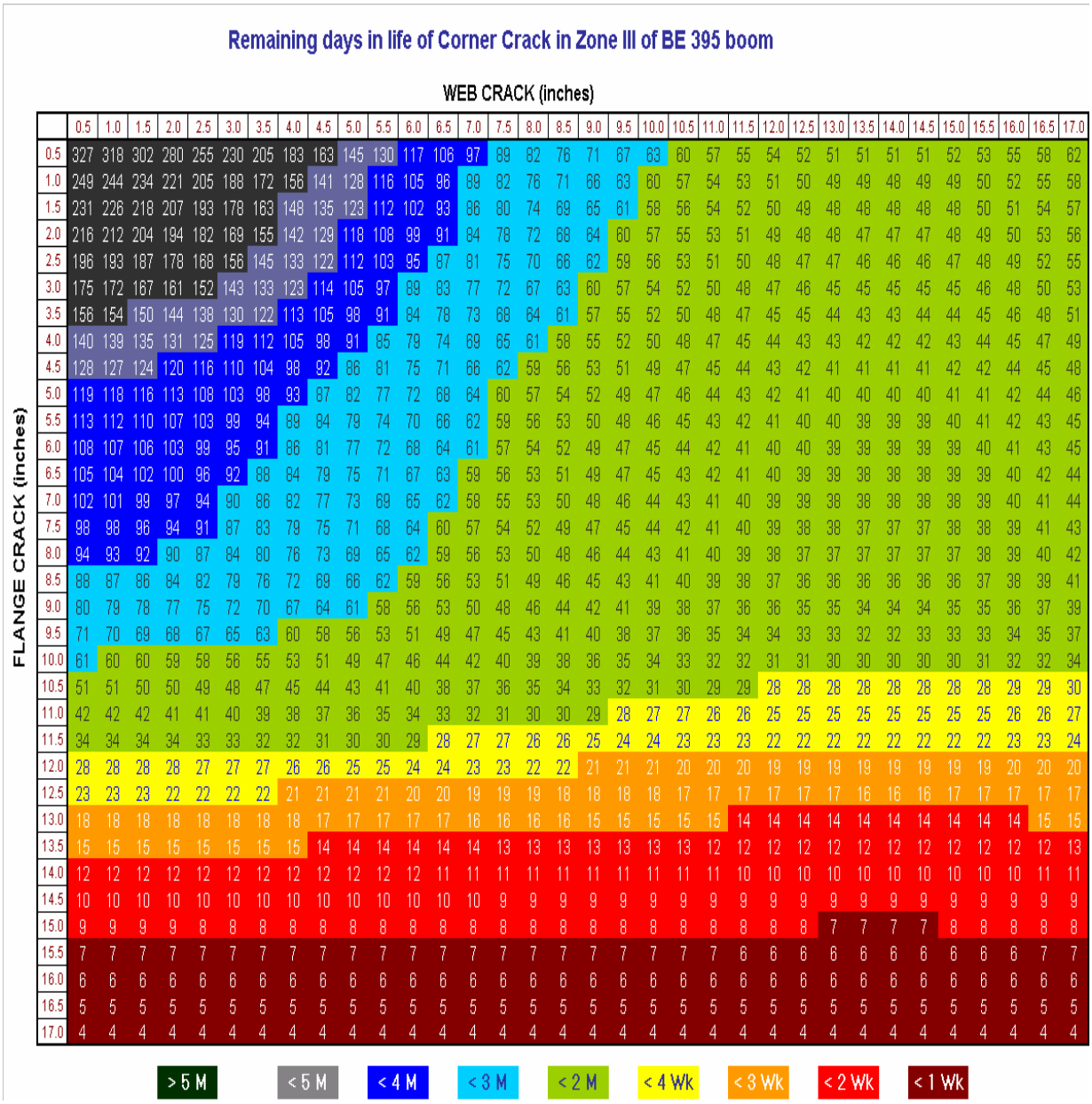

Table 16 – Crack Clock for Zone IV

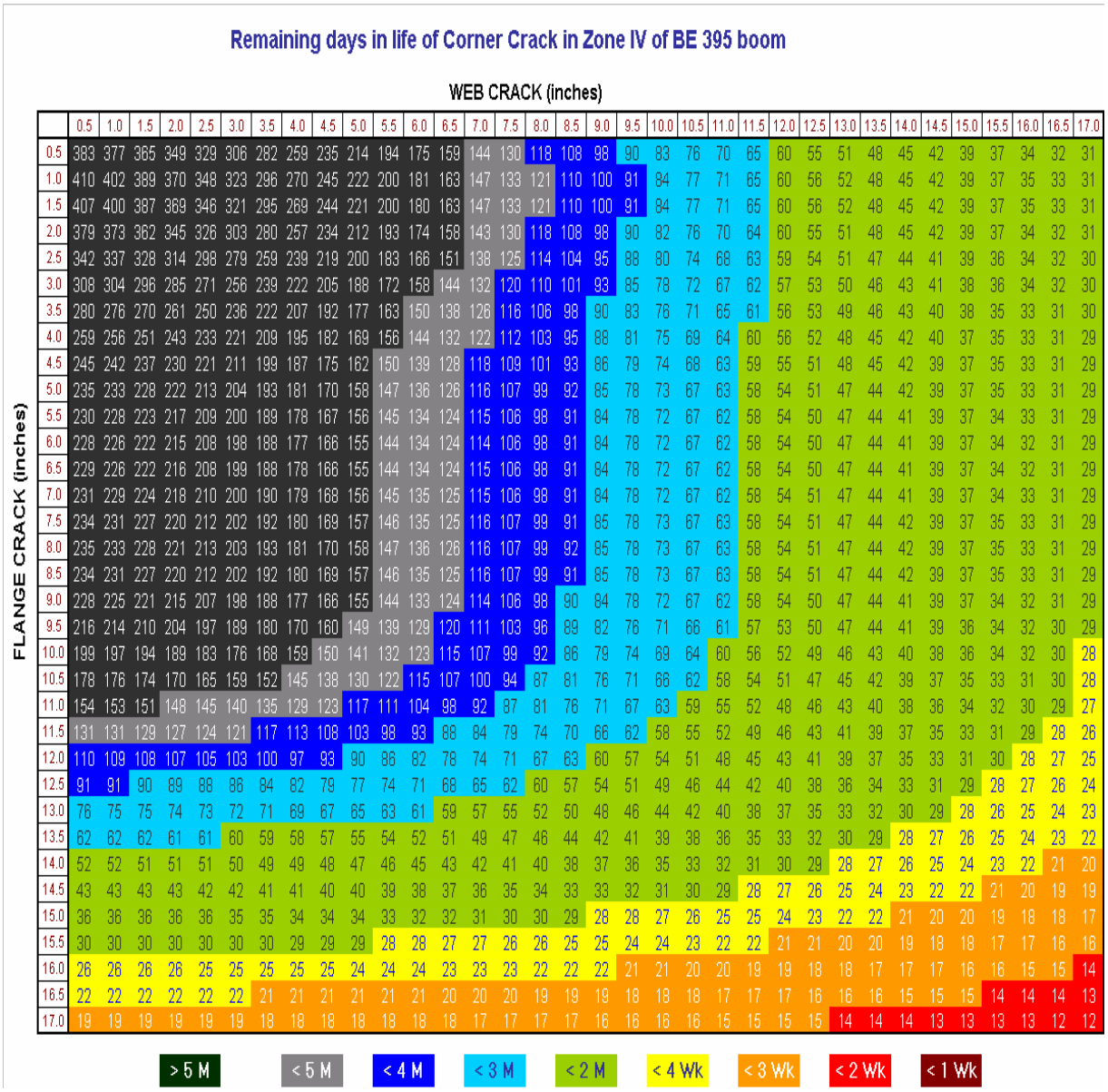

The crack clock charts are undoubtedly quite handy for maintenance planners since it gives them instantaneous prediction of remaining life for inspected cracks. However, the limitations of the charts due to uncertainties and error must be understood. The various sources of error and uncertainties are as follows:

1. **Equivalent applied load** – Data describing the variation of BE shovel loads are based on only two days of field testing in August 2002. Variations due to different ore types, weather conditions and operator practices would affect the measured data and the resulting equivalent load and boom stresses. More field data, obtained at different locations in the mine and different times of the year are required to assess the impact of the

2. **Limited data** – Corner crack of equal leg length is the base of the FEA runs and correction is added to account for unequal lengths in Zone I. This correction is available for crack lengths below 5" only. Although the correction is conservative for lengths below 5", it is used to extrapolate for lengths up to 17", which can introduce an unknown amount of error. It also used without adjustment for Zone II, III and IV, which can be a source of error as well.

3. **Regression analysis** – By definition, there is a difference between a regression curve and sample data. Although the coefficient of determination r^2 for all surfaces in Figures 61 through 65 implies a good fit (0.997, 0.995, 0.995 & 0.987 for Zone I, II, III and IV, respectively), the error in predicting the remaining life can be as high as 40 days as shown in the residual plots of Figures 61 to 65. However, the first chart (Zone I) is much more accurate, and more critical, than the rest and has residual error less than $\pm$10 days. Charts of Zone II and III are also much more accurate and critical than Zone IV chart with residual error less than $\pm$15 days. The residual error in Zone IV chart is between +30 and -40 days. Also, the standard error for the fitted surfaces is 3.2, 4.8, 5.5 & 14.5 for Zone I, II, III and IV, respectively, which implies that the 99.7% confidence level for the predicted life is $\pm$10, $\pm$14, $\pm$17, $\pm$44 for Zone I, II, III and IV, respectively.

4. **Error in crack measurement in the field** – Records of field inspections for the BE shovel boom indicate that there is potentially a significant error in crack length measurement during field inspections. The accuracy of crack measurement using non-destructive methods is dependent on many factors, including the crack size, geometry of the detail where the crack is located, crack location, inspection method, and inspector. No systematic investigation has been undertaken to date in order to quantify the error in field crack length measurements.

For these reasons, the life predictions of the crack clock shown in Tables 13 to 16 should be reduced by some appropriate factor before field implementation. Ideally, a statistical approach should be used to assess the probability of premature failure as a function of the sources of variation and error outlined above. Unfortunately, insufficient data is available to quantify the sources of error. This will be address in the next phase of the project, which will

consider a risk and reliability approach to fatigue crack management. In the absence of the information required for such an approach, one option is to reduce the predicted life for cracks by a constant percentage to account for variation in equivalent load and another factor that varies as crack grows to reflect the higher accuracy in the data range obtained from the finite element analysis. One possible equation for the ratio of predicted life to actual life for crack inf Zone I is the linear surface 1.25 + 0.025 ($a_f + a_w$) where the constant 1.25 reduces crack life by 20% to account for equivalent load variations. The slope (0.025) reduces the life of equal length 5" corner crack by another 20% or 12 days to account for regression error, which is consistent with the maximum residual and the 99.7% confidence level observed in Zone I. Zones II and III have slightly higher regression error and could adopt a factor of safety such as 1.25 + 0.030 ($a_f + a_w$). The slope (0.030) reduces the life of equal length 5" corner crack by 23% or 16 and 19 days for Zones II and III. Zone IV has the worst regression error and could adopt a higher reduction such as 1.25 + 0.040 ($a_f + a_w$). The slope (0.040) reduces the life of equal length 5" corner crack by 29% or 45 days, which is consistent with the maximum residual observed. Suggested values of the factor of safety for different zones and different crack lengths are shown in Table 17.

Table 17 – Factor of safety for factored Crack Clock

	Zone I	Zone II	Zone III	Zone IV
Corner crack length 0.5"(a_f) & 0.5"(a_w)	1.275	1.280	1.280	1.290
Corner crack length 0.5"(a_f) & 5"(a_w)	1.388	1.415	1.415	1.470
Corner crack length 5"(a_f) & 5"(a_w)	1.500	1.550	1.550	1.650
Corner crack length 17"(a_f) & 0.5"(a_w)	1.688	1.775	1.775	1.950
Corner crack length 17"(a_f) & 17"(a_w)	2.100	2.270	2.270	2.610

Using the factors of safety presented in Table 17 on Zone I Crack Clock, we obtained adjusted remaining life predictions as summarized in

Table **18**. The title for

Table **18** indicates that the predicted remaining days of operation for an inspected crack are factored to reflect the uncertainty in the assumptions used in both measurements and calculations of crack life. Similarly, Zones II, III and IV Crack Clock charts can be determined and they are shown in Tables 19, 20 and 21, respectively.

Tables 18 through 21 can be used to predict remaining life for inspected corner cracks in the BE shovel boom and make decisions on when a repair need to be made. They are based on actual measurements of operating load on the boom and actual fatigue properties of material around the crack.

Table 18 – Factored Crack Clock for Zone I

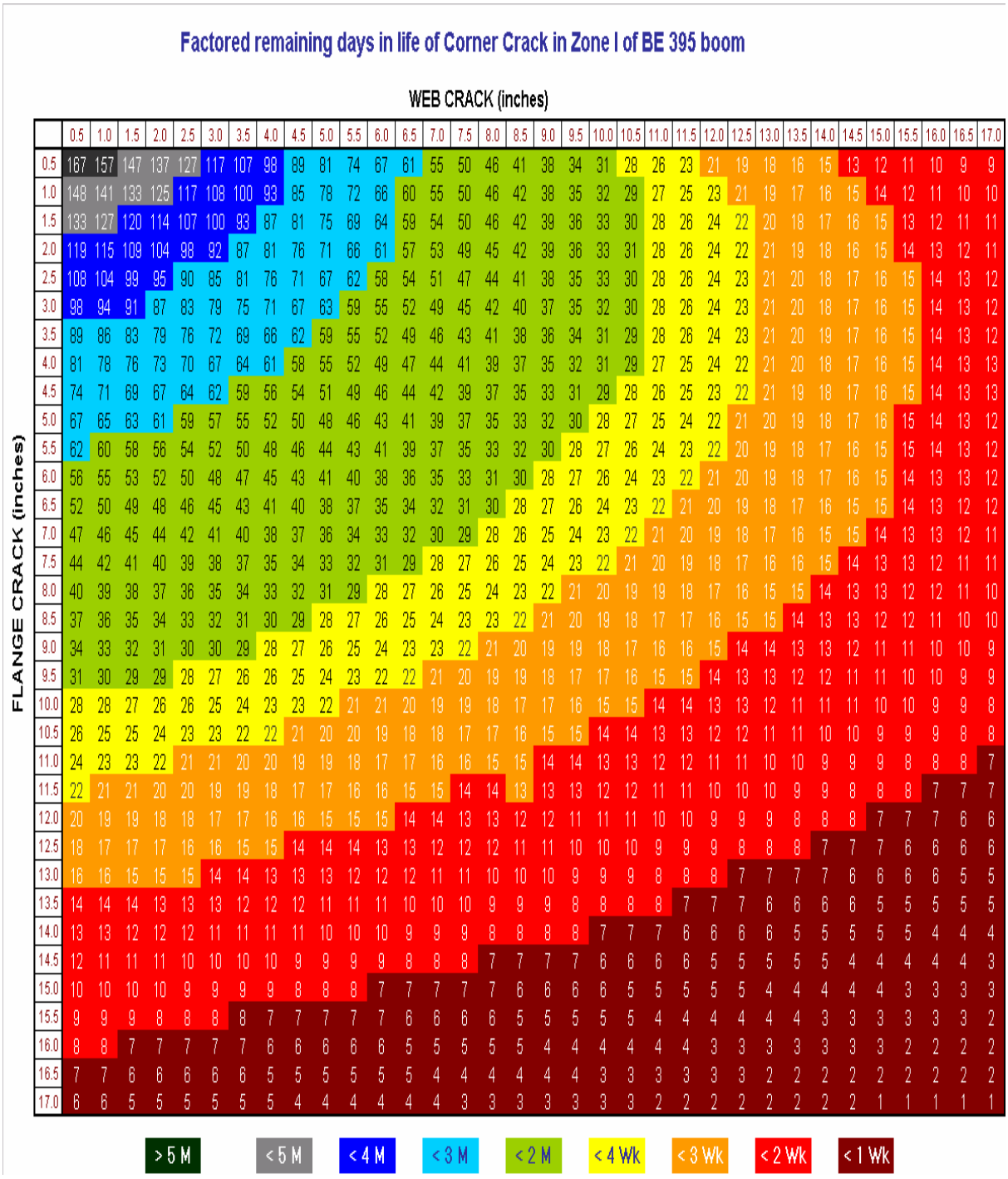

Table 19 – Factored Crack Clock for Zone II

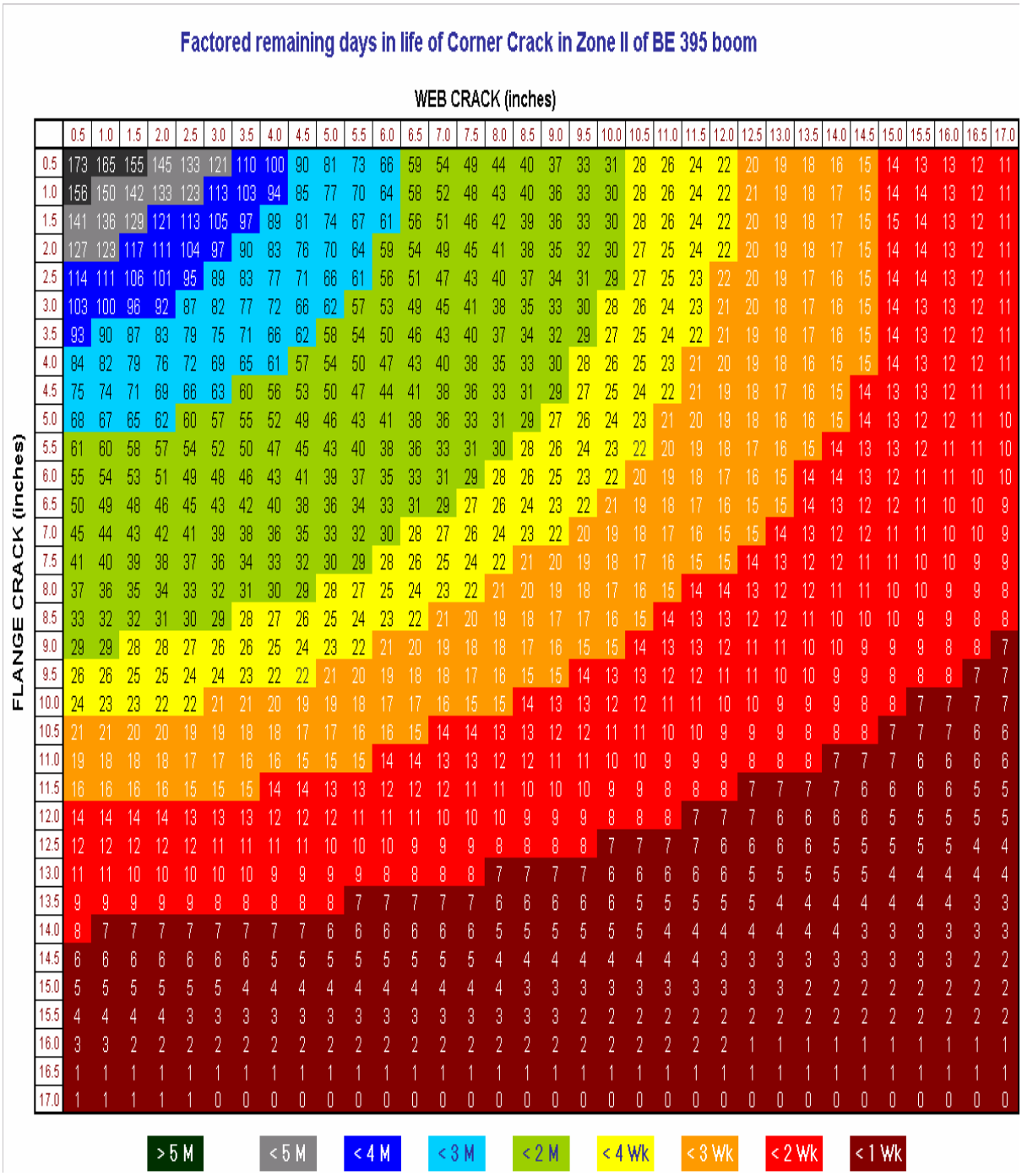

Table 20 – Factored Crack Clock for Zone III

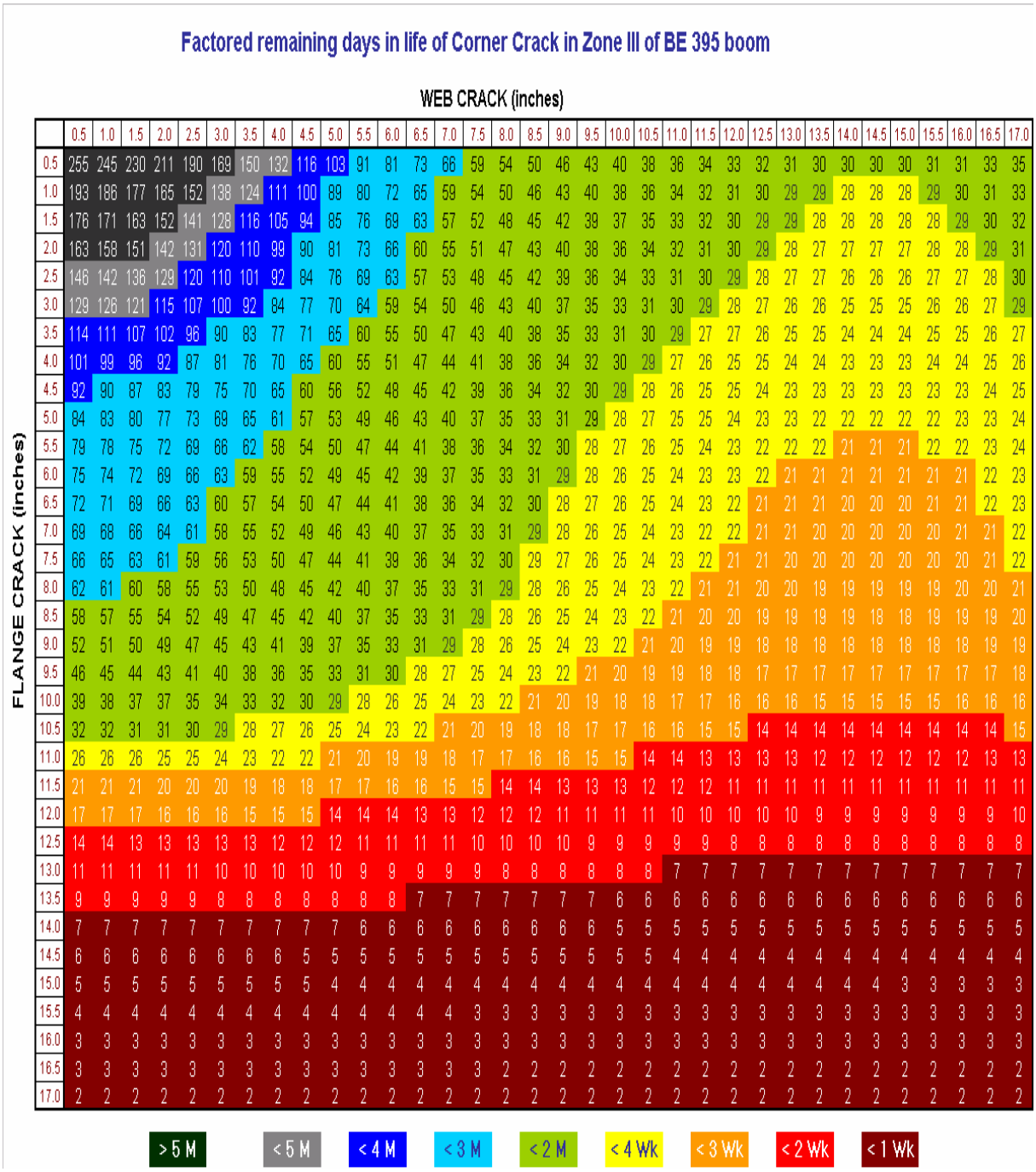

Table 21 – Factored Crack Clock for Zone IV

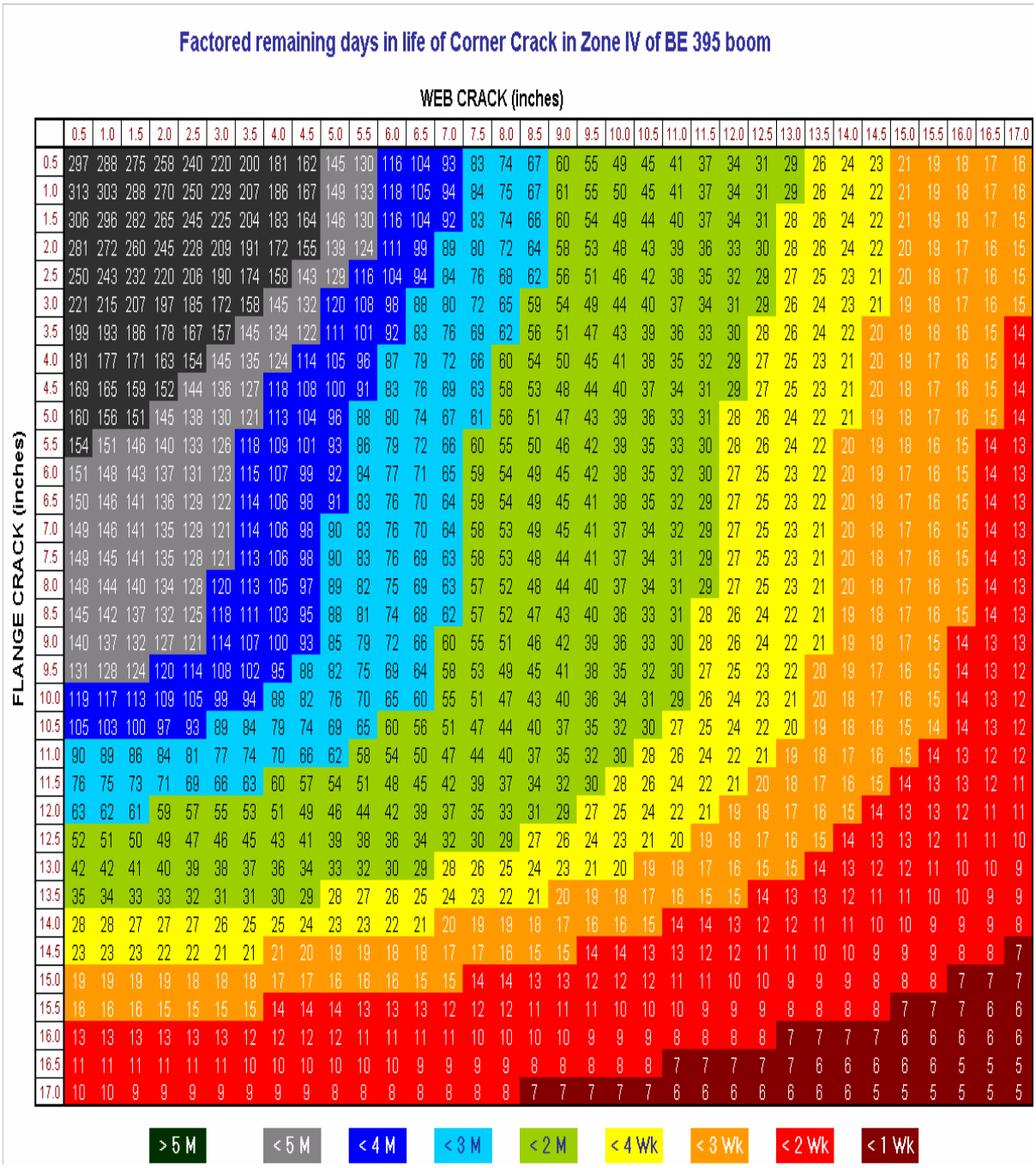

9. Summary and Conclusions

Maintenance cost at Syncrude represents a significant portion of yearly operating budget. Optimizing repair costs and shutdown outages can therefore lead to significant reductions in unit cost. One of the recurring problems with most mining equipment is cracking and this issue is therefore one that needs to be dealt with as part of the maintenance and repair program. This frequent and almost sure occurrence of cracking is largely due to high impact loads, high fatigue cycles, low operating temperature and large component size. To ensure safe and reliable operation, a good portion of the maintenance budget is allocated to monitor and repair cracks. This monitoring and repair strategy is based on vendor specifications and maintenance personnel experience. However, the oil sand environment causes cracks to appear much earlier than for typical mining applications. Also, newer and larger equipment do not necessarily conform to the experience gained from old equipment. These concerns, coupled with fast retirement rate of personnel, present a challenge to Syncrude's efforts in reducing maintenance cost and increasing equipment reliability.

The purpose of this research is to examine the crack management program at Syncrude and to optimize it using state-of-the-art technology. The research is conducted through collaboration with a research team from the Department of Civil & Environmental Engineering from the University of Alberta and is applied to the BE 395B shovel boom as an example but the same technique is applicable to any equipment component subjected to fatigue loading. The main product of this research is a tool that can optimize crack repair and improve equipment reliability.

Optimizing crack management involves four stages of detailed work. The first stage is the load spectrum evaluation, which deals with the assessment of actual cyclic loads acting on the equipment under normal operating conditions. This is achieved through field measurements and structural analysis of boom components. The measurements for the BE 395B shovel boom required strain gauges installed around the cross section of the boom box girder and cable transducers attached to the crowd tip. Boom strains and crowed position data were collected during actual operating conditions and were used with the finite element model to evaluate the frequency and magnitude of stresses acting on the boom. The frequency distributions of longitudinal stress range at different locations are presented in Figures 21, 22 and 24.

The second stage consists of numerical modeling, which involved the development of a refined finite element model of the boom that included through-thickness corner cracks and loaded with the load spectrum determined from the field data. Stresses resulting from variable stress spectrum can be transformed into a single equivalent stress range using Palmgren and Miner linear damage rule. The equivalent stress range distributions in the boom are presented in Figures 26, 27 and 28.

The third stage consists of the material properties characterization. Fatigue tests were performed on coupons made of the same nominal steel grade as the steel grade used in the boom, namely, CSA G40.21 350WT steel. Tension coupon tests and Charpy V-notch impact tests were performed to determine the monotonic material properties and to confirm the grade of steel. Single edge, straight-through notch specimens were subjected to cyclic loading to determine crack growth rate characteristics. The average regression curve of crack growth rate tests is presented in Equation [49]. Three-point bend tests were performed at room temperature and at -50^{o}C to obtain the fracture toughness. The average value of low temperature fracture toughness was found to be $92.8\ \text{MPa}\sqrt{\text{m}}$.

The final stage consists of a fracture mechanics analysis of the boom. By incorporating lab and field data into a finite element model of the boom structure that includes a through-thickness corner crack, stress intensities for different crack lengths were calculated and crack growth curves were obtained as shown in Figure 52. Due to the infinite number of flange and web crack length combinations, a simplified method is presented and used to generate 40 different crack propagation scenarios. Statistical curves are then used to interpolate and extrapolate these crack life predictions for different areas of the shovel boom as shown in Tables 13 to 16. An appropriate factor of safety is recommended for the remaining life predictions to account for the limited field data, inaccuracy of crack length measurements, and the assumptions made in the fracture mechanics analysis. The resulting tables are referred to as "Crack Clock charts" and they are shown in Tables 18 through 21.

The Crack Clock charts allow maintenance inspectors and planners to make fast and reliable decisions on managing boom cracks. Maintenance outages can be scheduled based on inspection results and remaining life. Repair of several cracked locations can be prioritized based on their relative remaining life. Changing operation demands can be accommodated without risking unscheduled shutdown or catastrophic failures. The Crack Clock chart is, in fact, an optimization tool for shovel maintenance.

References

Fisher, J.W., Kulak, G.L. and Smith, I.F.C. (1998). *A Fatigue Primer for Structural Engineers*, National Steel Bridge Alliance, American Institute of Steel Construction, Chicago, Illinois.

Gurney, T. and S. Maddox (1990). *An Alternative to Miner's Rule for Cumulative Damage Calculations?* in "Remaining Fatigue Life of Steel Structures", IABSE Workshop, Lausanne, 1990, IABSE reports Vol. 59, pp. 189-198.

Stephens, R.I., A. Fatemi, R.R. Stephens and H.O. Fuchs (2001). *Metal Fatigue in Engineering*. Second edition, John Wiley & Sons, New York.